Università degli Studi di Perugia

Facoltà di Scienze
Matematiche Fisiche e Naturali

Corso di dottorato di ricerca in scienza e tecnologia

per la Fisica e la Geologia

XXIX ciclo

PhD thesis:

Search for heavy Majorana neutrinos in Run II and feasibility study of a track-trigger for Phase 2 with the CMS detector at the LHC

Supervisor:
Prof. Livio Fanò

Candidate:
Luisa Alunni Solestizi

Assistant supervisors:
Dr. Orlando Panella
Dr. Francesco Romeo

Academic year 2015-2016

Abstract

This thesis intends to present the salient anspects of the research work carried forward in collaboration with the CMS experiment group, during my PhD.

The LHC accelerator and CMS detector main features are illustrated in the first chapter. The second chapter regards the CMS tracker subdetector status, performances, and future perspectives. The crucial role of the tracker in the HL(High Luminosity)-LHC era, starting from 2020, is here introduced.

Once clarified the technological context and the principles of work of the machines, where the proton collisions take place, and thanks to which the particles can be revealed, a specific data anlysis of the 2015 data collected by CMS will be shown. First, the current state of the searches of new physics, focusing on heavy neutrinos and leptoquarks, is illustrated in chapter 3, where the basis for a new search are provided. An original model is proposed (chapter 4), that leads a new experimental analysis, whose strategy and results are examined in chapter 5.
This is a search for physics beyond the Standard Model (SM) in the final state with two same-flavour leptons (electrons or muons) and two quarks. The analysis is performed using proton-proton collisions at $\sqrt{s} = 13$ TeV, recorded by the CMS experiment, at the CERN LHC. The data correspond to an integrated luminosity of 2.3 fb^{-1}; the results are interpreted in the framework of a recently proposed model, in which a heavy Majorana neutrino stems from a composite scenario.

The CMS collaboration is preparing the field to extend these searches in the future, at higher luminosity conditions. The HL LHC will require a totally different trigger paradigm, with the inclusion of the tracker at Level-1. After introducing the general needs and upgrade plans towards this new phase (chapter 6), a specific track-trigger proposal is formulated, based on the PCA statistical method. The software simulation and the hardware prototype of this innovative system will be discussed in chapter 7.

Contents

List of Figures

List of Tables

Chapter 1

The CMS detector at the LHC

1.1 The Large Hadron Collider

The Large Hadron Collider (LHC) is, currently, the most powerful hadron collider in the world [1]. It is housed in the already existing, 27-km-long, circular tunnel of LEP, in the Geneva region, at an average depth of 100 m underground (Fig.1.1). The machine yields head on collisions of two proton (or heavy ion) beams, circulating in opposite ways and in two distinct pipes, at a design energy per beam of 7 TeV (2.75 TeV for ions) and a design luminosity of $10^{34} cm^{-2} s^{-1}$.

The protons are accelerated by eight superconducting radio-frequency (RF) cavities per beam. This result in a 0.5 GeV/turn energy kick, during the injection phase. The beam trajectory is steered by 1 232 superconducting dipole magnets, each 15-m-long and featuring an 8.3 T field strength. Several thousands, higher order, magnets (quadrupoles, sextupoles, etc) focus the beam. The LHC is the last step of a larger acceleretor complex. Linac 2 takes the protons extracted from a bottle of hydrogen gas, forms the beam, and inject it, at 50 MeV, into the Proton Synchrotron Booster (PSB). The PSB accelerates the protons up to 1.4 GeV. The beam passes to the Proton Synchrotron (PS), and then to the Super Proton Synchrotron (SPS). Here, it reaches 450 GeV of energy, enough to be tranferred into the LHC. At nominal parameters, the LHC proton beams consist of bunches of $O(10^{11})$ protons each, spaced by 25 ns. Their tranverse section, near the collision point, has dimensions of the order of tens of microns.

There are four main experiments, located in underground caverns, in corrispondance of the collision points, along the path of the LHC circumference. The ATLAS

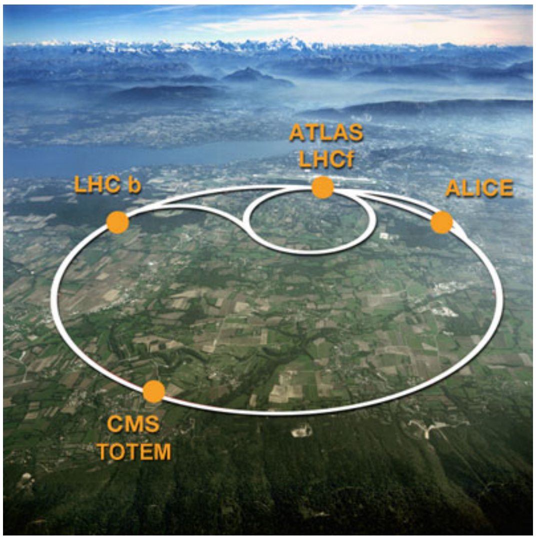

Figure 1.1: The circunference of the Large Hadron Collider. The four orange dots correspond to the four collision points, surrounded by the particle detectors. They are: ATLAS, CMS, ALICE, LHCb, and the smaller TOTEM and LHCf, both using particles thrown forward by collisions.

(A Toroidal LHC ApparatuS) and CMS (Compact Muon Solenoid) detectors, the polar opposite of the circumference, are twin experiments. They were designed to discover the Higgs boson, and to look for signals of new physics beyond the Standard Model (SM), but also to study a wide range of phenomena produced by both ion-ion and proton-proton collisions. The LHCb experiment was designed to carry out precision measurements of the CP-violation and the rare decays of B hadrons in proton-proton collisions. The ALICE (A Large Ion Collider Experiment) detector is used to study the physics of strongly-interacting matter and the quark-gluon plasma, in heavy-ion collisions. Two more, smaller experiments, TOTEM and LHCf, are interested in the study of the very forward particles from proton-proton collisions.

The LHC operation began on the 10th of September 2008, when the first beams circuleted successfully for the first time. After an accident to the dipole circuit, the machine activity had to be suspended until the autumn 2009, when it restarts aiming to reach half the design energy of 3.5 TeV per beam. The first LHC p-p (proton-proton) collision at 7 TeV of energy in the centre of mass happened on the 30th of March 2010. The integrated luminosity collected was 45.0 pb^{-1} in 2010 and 6.1 fb^{-1} in 2011, at 7 TeV collisions; while the luminosity delivered in 2012, at 8 TeV, was of 23.3 fb^{-1}. Then, the LHC entered a 2-year-long technical stop period, LS1 (Long Shutdown 1), in which magnet interconnects have been repaired, in order to collide at design energy and luminosity, in 2015. Last year, the proton beams were back in the accelerator, and the first beam of Run II, at the record energy of 6.5 TeV, was recorded, on the 10th of April 2015. The first collisions at the lower beam energy of 450 GeV followed. Since June 2015, new data at 13 TeV have been recording by the detectors, reaching an integrated luminosity of 4.2 fb^{-1} for that year. After a brief winter shutdown, new data have been collected at the same energy, during 2016. They correspond to an integreted luminosity of fb^{-1}.

1.2 Compact Muon Solenoid

The Compact Muon Solenoid (CMS) is a general purpose detector that operates at the Large Hadron Collider (LHC) at CERN [2]. It is installed, about 100 m underground, close to the French village of Cessy. CMS has a cilindrical and endcap structure, able to hermetically cover all the solid angle around a collision, as the schematic view in Fig.1.2 shows. The detector is 21.6 m long, 14.6 m in diameter, and weighs approximately 14 000 t.

At its centre, there is the silicon tracker, whose granularity reduces from the innermost pixel detector to the more external microstrip detector. These are encompassed by the lead tungstate crystal electromagnetic calorimeter, and the brass and scintillator hadronic calorimeter. A preshower system is located in front of the endcap calorimeter, in order to distinguish pions from prompt photons. A superconducting solenoid, of 12.5 m of length and 6 m of internal radius, surrounds most of the calorimeter volume, and provides a magnetic field strength of 3.8 Tesla. This powerful magnetic field allows to accurately measure charged particle momenta, up to high energies, using the track curvature. The muon system is all outside of the solenoid, and consists of three different kind of gas ionization chambers, for identifying muons, and for determining their momenta and charge. These muon stations are interleaved with iron layers, that behave as return yoke for the magnetic flux.

The purpose of the CMS subdetectors is to measure, with high resolution, the energy, momentum, and position of electrons, muons, photons and hadrons. The neutrinos can be inferred, thanks to the CMS hermeticity, through the transverse energy imbalance of all the reconstructed visible particles in the event.

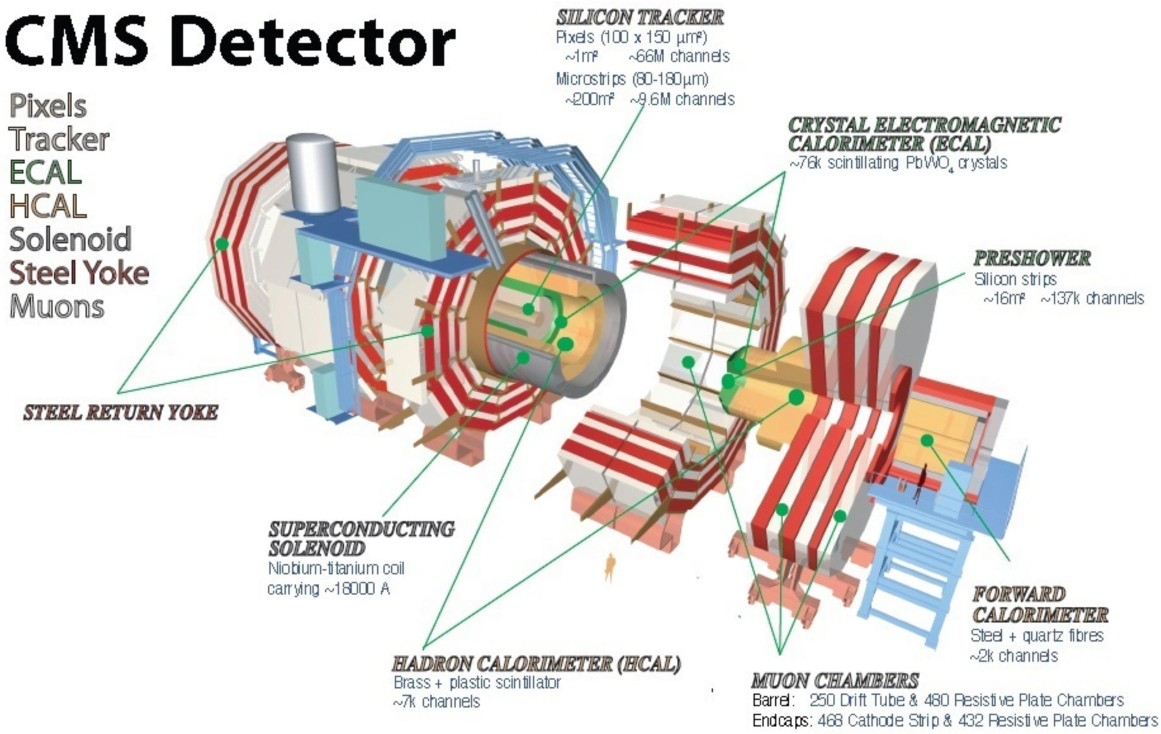

Figure 1.2: Exploded view of the CMS detector.

The coordinate system adopted by CMS has its origin at the nominal collision point, the horizontal x-axis points radially towards the centre of the LHC circumference, the y-axis points vertically upwards, and thus the z-axis points along the beam direction. It is intuitive, for a cilindrical experiment, using cylindrical polar coordinates; the azimuthal angle ϕ is measured from the positive x-axis in the x-y plane, and the polar angle θ is measured from the positive z-axis in the y-z plane. The pseudorapidity $\eta = -ln(tan\frac{\theta}{2})$ is often used, instead of the polar angle. The angular separation of particles in the detector is typically described by the quantity ΔR, defined as $\Delta R = \sqrt{(\Delta\phi)^2 + (\Delta\eta)^2}$. Transverse energy E_T and momentum p_T are defined as the components of energy and momentum in the x-y plane. The imbalance of the detected energy in the transverse plane, associated with undetectable particles, such as neutrinos, is defined as the missing-transverse energy, MET.

Two levels of trigger systems are used to reduce the event rate from 40 MHz to the order of 100 Hz for archival storage.

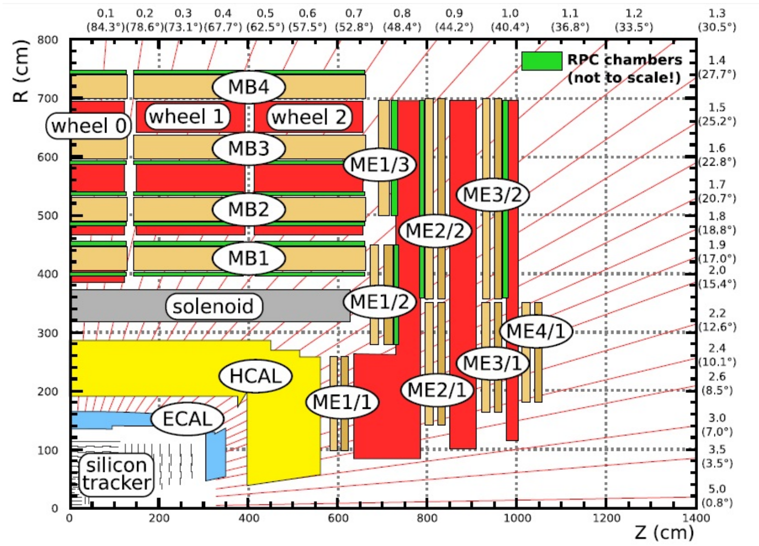

Figure 1.3: View of a CMS quadrant in the R-z plane.

1.3 Tracking system

The tracking system is the part of the detector closest to the beam pipe [3]. It measures the trajectories (tracks) of the charge particles travelling through it, thanks to semiconductor detector elements.

Consisting in a cilinder of both barrel and endcap components, the system has an overall length of 5.8 m and a diameter of 2.5 m, and covers a pseudorapidity range of $|\eta| < 2.5$. The heart of the tracker is the Pixel detector. In the outer tracker, the barrel part consists of the Tracker Inner Barrel (TIB) and the Tracker Outer Barrel (TOB), whereas the endcap disks are made up of the Tracker Inner Disks (TID) and the Tracker End Caps (TEC). One can refer to Fig.1.4, where black lines indicate single detector modules, whilst each blue line represents a stereo module. In these modules, each strip is coupled with another one, that is rotated with regard to the first one, allowing for the measurement of the respective missing third coordinate. The innermost components are built using silicon pixel elements, while all outer components are made up of silicon strip elements. The tracker is equipped with insulation and a cooling system, ensuring a safe operating temperature.

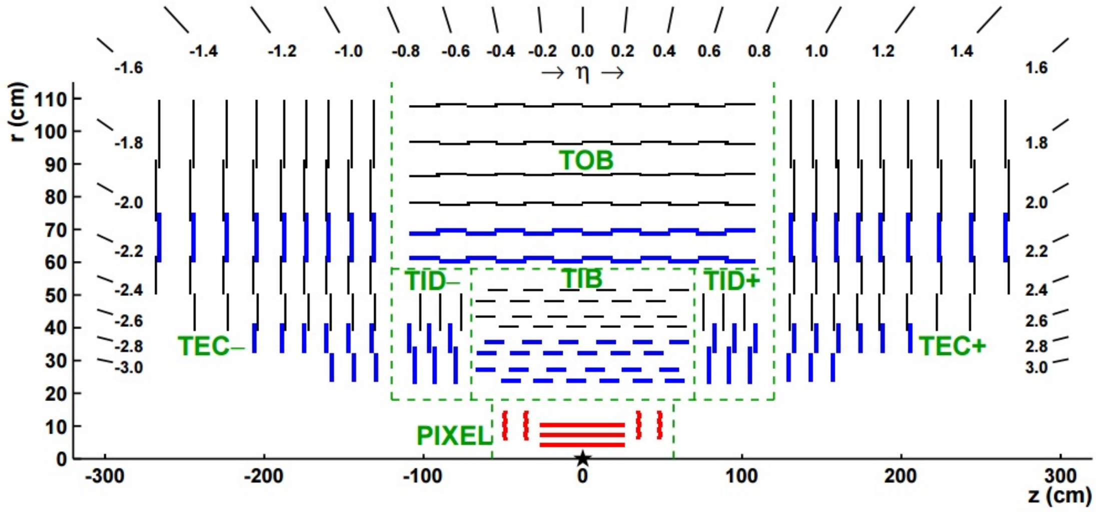

Figure 1.4: The current CMS tracking system.

The tracks of charged particles are curved, due to the magnetic field of 3.8 T, established by the solenoid, and a measurement of their curvature allows to determine both the charge and the momentum of the particles. The momentum resolution in the tracker is better than 3%, in the central part of the detector ($|\eta| < 1.5$), for particles with transverse momentum up to 100 GeV.
The tracker system also provides a robust vertex reconstruction. The spatial resolution of the tracker permits to distinguish between tracks coming from the hard proton-proton interaction and from the pile-up vertices. The transverse impact parameter resolution, for particles with $p_T > 10$ GeV, is better than 35 μm, while the longitudinal impact parameter resolution is better than 75 μm.
Moreover, the tracker performance allows to identify jets containing a bottom quark, using b-tagging algorithms. The identification of b jets is interesting for several studies; top quark decays via the $t \to bW$ process with a branching fraction of almost 100%, many particles predicted by beyond Standard Model (BSM) theories have final states involving bottom quarks.

1.4 Calorimetry system

The main calorimetry sistem [4] is included inside the solenoid, and consists of two subdetectors, both of which enclose the tracking system. The inner subdetector is the Electromagnetic Calorimeter (ECAL), designed to detect electromagnetically interacting particles, like photons and electrons. On the outer side is the Hadron Calorimeter (HCAL) that focuses on hadrons, which interact with the detector via the strong force, and usually are not stopped by the ECAL.

The calorimetry system is important, not only for the direct measurement of the energy of the detectable particles, but also for the determination of the overall balance of the transverse energy in a collision event. This variable gives information on those particles that cannot be detected, like neutrinos or the various weak interacting hypothesised particles, in theories beyond the Standard Model.

A statistical description of the energy deposit of electrically charged particles traversing the detector material is given by:

$$E(x) = E_0 e^{-\frac{x}{X_0}}. \tag{1.1}$$

E(x) is the energy of the particle, after travelling a distance x in the material, E_0 is the initial energy, and X_0 is the radiation length. This is defined as the distance after which the particle energy has been reduced to E_0/e. In the case of hadrons, the same formula can be used, but the hadron interaction length λ_I takes the place of the radiation length. Because of their direct relation to the physical absorption processes, these two lengths X_0 and λ_I are employed as units for the specification of the amounts of absorbing material in specific parts of the detector.

1.4.1 The ECAL

The ECAL is made up of lead tungstate ($PbWO_4$) crystals, that work both as absorbers and as scintillators. Having a single active material allows for a better energy resolution, than that achieved by adding passive-material layers. The interaction of an electron or photon, with the scintillating material, results in particle electromagnetic showers. They consist of electrons, positrons and photons, emitted via pair production and bremsstrahlung. Precise photo-detectors have the aim to convert the produced photons in an electrical signal, that is roughly proportional to the energy of the original particle. The lead tungstate has a density of 8.28 g/cm^3, a radiation length of $X_0 = 0.89$ cm, and is transparent to visible light. It gives an high speed of response; about 80% of the light of a given excitation is emitted within 25 ns, which corresponds to the design bunch-crossing time.
The ECAL is divided in the Electromagnetic Barrel (EB), consisting of 61 200 lead

tungstate crystals, and in two Electromagnetic Endcaps (EE), located at $|z| = 314$ cm, consisting of 10 764 crystals each. The crystals have lengths of 230 mm and 220 mm, in the barrel and endcap regions, respectively, comparable to 25 radiation lengths. In the EB, the detection of photons is performed by silicon avalanche photodiodes. In the EE, these are replaced by vacuum phototriodes, in order to avoid too high leakage currents, due to the higher radiation doses in the endcap region.
The endcaps are fitted with preshower detectors, consisting of lead absorbers and silicon detector layers, which provide a better angular resolution than the lead tungstate crystals. This allows to improve the discrimination capability between single photons and neutral pions, that decay into two photons with small angular separation.

1.4.2 The HCAL

The HCAL is a sample calorimeter, this means that it alternates layers of absorber and scintillating material. Brass is used as the main absorber material because is non magnetic, has an high density of $\rho = 8.53\ g/cm^3$ and a short interaction length of $\lambda_I = 16.42\ cm$. Plastic materials have been chosen as scintillators.
The HCAL consists in the Hadron Barrel (HB), Hadron Outer (HO), Hadron Endcap (HE) and Hadron Forward (HF). The HB and HO cover until $|\eta| < 1.3$, the endcaps extend from $|\eta| = 1.3$ to $|\eta| = 3.0$, and the HF has a range of $3.0 < |\eta| < 5.3$. In terms of radiation lenght, it means 5.82 λ_I for the HB and 10 λ_I for both HE and HF.
The HO is located outside the magnetic coil, for catching the tails of the more energetic showers not contained in the HB, it exploits the addictional absorber represented by the solenoid.
In the HF a different detection method is used; it employs copper as absorber material, and relies on quartz fiber calorimetry. The mechanism of interaction here is the Cerenkov effect; photons are emitted by particles traversing the quarz fibers faster then light in the means. Dedicated photomultipliers convert photons in elecrtical signals. The advantages of this technique are: higher speed of response, which lies on a scale much smaller than the design bunch crossing time of 25 ns, and the insensitivity to neutrons' fluxe, very large in the HF.

1.5 Muon system

The muon chambers [5] are the outermost subdetector of CMS, and alternate to the magnetic return yokes, thus, they are immersed in a magnetic field of 2 T. The vast majority of particles able to survive, after passing through all other detector layers, are the muons, which, due to their high mass, have comparatively small energy losses via bremsstrahlung in the calorimetry systems. Muons occur in many of the most interesting processes of the Standard Model and of new physics. Their importance is reflected even in the name that was chosen for CMS as a whole.

The muonic system is divided three components, see Fig.1.5:

- The Drift Tubes (DT); this system covers $|\eta| < 1.2$, and consists in cell of 21 mm of lenght, filled with a a gas mixture of 85% Ar and 15% CO_2, in which the drift time are of the order of 380 ns.

- The Resistive Plate Chambers (RPC); they cover $|\eta| < 1.6$, and consist in gas chambers, enclosed between pairs of paralel plate of phenolic resin. They provide high performances in timing, enabling to compensate the slow detection process in the other muon subsystems, and to trigger the events at online level.

- The Cathode Strip Chambers (CSC); only in the endcap, extend closer to the beam pipe than the other two subsystems, featuring $0.9 < |\eta| < 2.4$. Consist of multiwire proportional chambers, covering roughly 5 000 m^2, and using about 2.5 million wires.

The individual stations of both the CSC and RPC systems are separated by the iron disks of the flux return yoke.

1.6 Trigger

The high bunch-crossing rate of up to 40 MHz at the LHC, joined to the amount of subdetector readout channels, and to the fact that there are several simultaneous collitions per crossing, makes impossible to store this amount of data in its entirety. The purpose of the trigger system [6] is precisely to reduce, in a reasonable time, the data to a more manageable subset, while discarding as little useful information as possible.

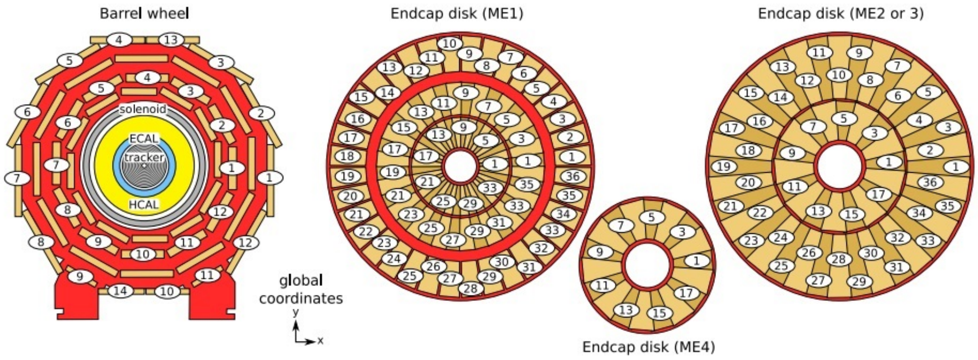

Figure 1.5: Transverse slices of CMS; the central barrel wheel and representative endcap disks, indicating the numbering of the DT azimuthal sectors in the barrel and the CSC chambers numbers in the endcaps.

The first step of the trigger system is the Level-1 (L1) Trigger, which is performed on custom-designed and programmable electronics and reduces the data rate to about 0.1 MHz. It operates on special primitive trigger objects, provided by the calorimetry and muons systems. A full readout of the detector data can be delayed, until after this trigger has made its decision on the retention of an event. The readout systems are activated only for those events passing this first step.

In a second step, the High Level Trigger (HLT) further reduces the rate to under 400 Hz. It is implemented in software, using a custom version of the CMS analysis software reconstruction algorithms, and runs on a dedicated computing cluster.
The combination of the electronic devices and computing cluster resources, used for the trigger system, is referred to as the Data Acquisition (DAQ) system.

Chapter 2

Tracker operation

The scientific programme of the CMS experiment at the LHC covers a very wide spectrum of physics at the TeV scale. The trajectories of charged particles, called tracks, are among the most fundamental objects in the reconstruction of proton-proton (p-p) collisions. Tracks of electrons, muons, taus, and hadrons have to be reconstructed.

The task of the CMS tracker [3] is to measure the tracks up to high momentum, with high resolution, high reconstruction efficiency, and low fake rate. In addition, tracks may be used to identify b jets, through the displacement of their secondary vertex, compared to the primary vertex. The tracker has to face a high-density tracks scenario, including superimposed p-p collisions in the same event (pile-up), and a high frequency rate.

The achievement of these goals requires a proper modelling of the tracker design, and excellent tracking performances, which depend also on the calibration and the alignment of the tracking devices.

In the next-two sections, the commissioning issues and the performances of the tracker are going to be illustrated.

2.1 Commissioning

Before starting the LHC p-p collisions, the CMS experiment was commissioned, using events containing cosmic muons, collected during the Cosmic Run At Four Tesla (CRAFT). The detector and the magnetic field conditions during CRAFT were quite similar to the conditions during p-p collisions. Thus, the results obtained from CRAFT provided good initial operating points for the pixel detector, the strip detector, the tracker alignment, and the magnetic field. We focus here on the tracker commissioning [15].

2.1.1 Calibration and timing

In order to apply the bias potential to each of the sensors, calibration procedures were used to determine the ADC gains and pedestals for all the channels.

The tracker readout system uses the 40 MHz LHC clock as input. The signals from the CMS trigger system must arrive at the proper time, within the 25 ns clock cycle, to associate the correct bunch crossing with any signal above the readout threshold. An optimally phased clock signal will maximize the number of pixels observed in clusters. Thus, the overall trigger timing was adjusted by varying the clock phase, until the average barrel and endcap cluster sizes, as measured in minimum bias triggers, were maximized.

2.1.2 Lorentz-drift correction

The drift direction of the charge carriers is affected by the Lorentz force, due to the high magnetic field, in which the tracker is immersed. The Lorentz angle θ_L, by which charge carriers are deflected in a magnetic field perpendicular to the electric field, is defined by

$$\theta_L = \frac{\Delta x}{d} = \mu_H B = r_H \mu B, \tag{2.1}$$

where d corresponds to the drift distance along the electric field, and Δx to the shift of the signal position. The drift mobility in a magnetic field, called the Hall mobility, is denoted by μ_H, the drift mobility without magnetic field by μ. They are related by the Hall scattering factor $r_H = \mu_H/\mu$. This factor describes the mean free time between carrier collisions, which depends on the carrier energy.
Another important question is the dependence of the Lorentz shift on the irradiation dose. Radiation damage can change the drift properties, which will change the Lorentz shift. Such a shift appears as a misalignment of the detector as function of radiation dose, which itself is a function of the distance from the interaction point.

The Lorentz-drift effects are encoded in the cluster shapes, and the PIXELAV simulation is used to compute them. The actual Lorentz calibration procedure is to tune the detailed simulation to agree with data.

The 2008 cosmic ray data were calibrated by measuring the cluster x-sizes as functions of $cot(\alpha)$, where α is the angle between the x axis and the track projection on the local x-z plane, see Fig.2.1. In the pixel barrel, -$cot(\alpha_{min})$ is equal to $tan(\theta_L)$.

The barrel calibration was repeated with collision data in December 2009 using a new technique. This makes use of the two-dimensional pixel segmentation to measure the average transverse displacement of the charge carriers, as a function of the distance along clusters, produced by highly inclined tracks. Since longitudinal position in the cluster is completely correlated with depth in the junction, this technique determines the average transverse carrier displacement as a function of depth.

The two techniques are affected by different systematic effects. A variation of the fitting procedures suggests that the total systematic uncertainty on the Lorentz angle calibration is less than 2%. A consistency better than 1% has been observed between the real and simulated measurements.

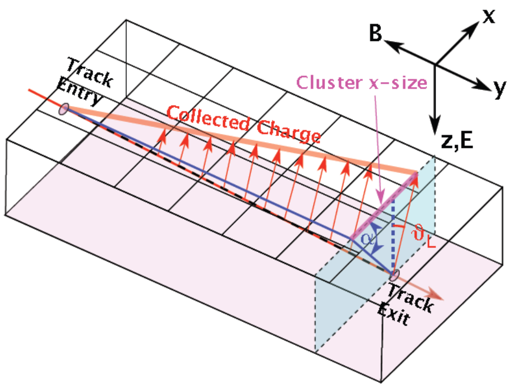

Figure 2.1: A track in the pixel local coordinate system. The local z axis coincides with the sensor electric field $\vec{E}$. The local x axis is chosen to be parallel to $\vec{E} \times \vec{B}$, where $\vec{B}$ is the axial magnetic field. The local y axis is defined to make a right-handed coordinate system. The angle α is the angle between the x axis and the track projection on the local x-z plane.

2.1.3 Alignment

One of the most important inputs for reconstructing the tracks is the tracker geometry; the set of parameters describing the geometrical properties of all the mod-

ules composing the tracker. This has to be determined after an accurate alignment procedure [17]; any misalignment of the tracker geometry is a potentially limiting factor for its performance.
The statistical accurancy of the alignment should stay below the intrinsic silicon hit resolution of 10 μm in the pixel detector. The other important aspect is the efficient control of the systematic biases; inaccurate treatment of material effects, imprecise estimation of the magnetic field, and a lack of sensitivity of the alignment procedure itself to such degrees of freedom can be source of such systematic distortions.

The magnetic field of the CMS solenoid is to good approximation parallel to the z-axis. The orientation of the tracker respect with the magnetic field is of special importance, since the correct parameterisation of the trajectory in the track reconstruction depends on it. This global orientation is determined by the angles θ_x and θ_y, the rotations of the whole tracker around the x-axis and the y-axis, respectively. These tilt angles are essential to be determined prior to the internal alignment correction, because the latter might be affected by a wrong assumption on the magnetic field orientation. It is expected that the tilt angles will not change significantly with time, hence one measurement should be sufficient for many years of operation. The tilt angles have been determined with the 2010 CMS data, and they have been used as the input for the internal alignment.

The CMS silicon tracking subdetector consists of 1 440 silicon pixel and 15 148 silicon strip detector modules. To first approximation, the CMS silicon modules are flat planes and their degrees of freedom are three shifts (u, v, w) and three rotations (α, β, γ). Sensor curvatures can be expected, for instance because of the tensions after mounting; to take into account such deviations, the vector of alignment parameters is extended to up to nine degrees of freedom.

Track-hit residual distributions are generally broadened if one assumes that the positions of the silicon modules used in the track reconstruction differ from the true positions. Thus the standard alignment algorithms follow the least squares approach and minimise the sum of squares of normalised residuals from many tracks

$$\chi^2(\vec{p},\vec{q}) = \sum_j^{tracks} \sum_i^{hits} \left(\frac{m_{ij} - f_{ij}(\vec{p},\vec{q})}{\sigma_{ij}} \right)^2$$

where m_{ij} are the hit positions with the uncertainties σ_{ij}, f_{ij} is the trajectory prediction of the track, depending on the geometry ($\vec{p}$) and track parameters ($\vec{q}$).

Two independent and complementary alignment algorithms have been used by

CMS during Run 2; Millepede-II and HipPy(HIP). Millipede works using a global approach, HIP a local one; the first minimises the χ^2 function, by taking into account track and alignment parameters simultaneously, whilst HIP does not consider the track parameters. Millepede considers the correlations among the modules, that are ignored by HIP. The latter has the advantage to solve a simpler local problem, with O(10^1) parameters for every module, compared to Millepede that has to solve a matrix equation of size n, where n is of the order of 10^6. The HIP's disadvantage is the need for many iterations to perform the alignment, from 10 to 20, depending on; the element we are aligning, the goodness of initial geometry, the available time, and the computing resources.

2.2 Performances

The physics program aimed by CMS sets the minimum level of performance that the tracker has to match [16]. The required efficiency and resolution of the tracking system were evaluated since the early stages of the detector design. The tracker should provide;

- A resolution on the transverse momentum, p_T, of 1.5% (10%) for 100 GeV (1 000 GeV) momentum muons.
- Correct charge assignment for leptons of energy up to 2 TeV.
- Reconstruction efficiency higher than 95% for isolated charged particles of momentum above 1-2 GeV, and efficiency of the order of 90% for particles with the same momentum threshold, but collimated inside jets.
- Measurement of the longitudinal impact parameter with a minimal resolution of 2 mm, to associate particles to the p-p collision vertices they originated from.
- Resolution around 20 μm for the transverse impact parameter and around 100 μm on the longitudinal one, to implement valuable b-tagging.
- Detector occupancy below 1% to facilitate the pattern recognition in the congested environment of LHC collisions. The occupancy is defined as the ratio of the number of detector channels, above the noise level to the total number of channels.

- At least in the barrel region of the Tracker, the amount of material budget should be less than 0.15-0.30 radiation lengths. This requirement is necessary to avoid that the reconstruction of photons and electrons is spoiled, because of conversions and bremsstrahlung radiation. In the same way, an excessive material budget deteriorates the resolution on the trajectory parameters of low energy particles because of multiple scattering.
- At the LHC design luminosity of $L = 10^{34}\ cm^{-2}s^{-1}$, about 1 000 particles, from more than 20 overlapping interactions, are expected to traverse the tracker volume every 25 ns. The tracking system is required to have a sufficiently fast time response in order to associate correctly the detected signals to the corresponding bunch crossings.

In addition to the previous list, it is imperative that the components of the tracking system are sufficiently radiation tolerant to maintain, without major interventions, the design performance for the full extent of the CMS operations at LHC.

2.2.1 Track reconstruction

The track reconstruction algorithms [16] rely on a good estimate of the p-p interaction point, referred to as beamspot.
Starting from the location of the beamspot, an initial round of track and vertex reconstruction is performed using only the pixel hits. The standard track reconstruction is performed by the combinatorial track finder (CTF). Tracks are seeded from either triplets of hits in the tracker or pairs of hits, with an additional constraint from the beamspot or a pixel vertex. This yields an initial estimate of the trajectory, including its uncertainty.
The seed is then propagated outward in a search for compatible hits. As hits are found, they are added to the trajectory and the track parameters and uncertainties are updated. This search continues until either the boundary of the tracker is reached or no more compatible hits can be found.
A second search for hits is performed starting from the outermost hits and propagating inward.
The first two iterations of this procedure use pixel triplets and pixel pairs as seeds to find prompt tracks with $p_T > 0.9\ GeV$. The next iteration uses pixel triplet seeds to reconstruct low-momentum prompt tracks. The following iteration uses combi-

nations of pixel and strip layers as seeds, and is primarily intended to find displaced tracks. The two final iterations use seeds of strip pairs to reconstruct tracks lacking pixel hits.
In the final step, the collection of hits is fitted, to obtain the best estimate of the track parameters.
At the end of each iteration, the reconstructed tracks are filtered to remove tracks that are likely fakes. The filtering uses information on the number of hits, the normalized χ^2 of the track, and the compatibility of the track to be originated from a pixel vertex. This information is used to enstablish the quality level of the tracks. Tracks that pass the tightest selection are labelled "highPurity".

In the context of the reconstruction software of CMS, the five parameters used to describe a track are; d_0, z_0, ϕ, $cot\theta$, and the p_T, defined at the point of closest approach of the track to the assumed beam axis. This point is called the impact point, with global coordinates (x_0, y_0, z_0). Thus, d_0 and z_0 define the coordinates of the impact point in the radial and z directions, being d_0 defined as $d_0 = -y_0 \cdot cos\phi + x_0 \cdot sin\phi$. The azimuthal and polar angles of the momentum vector of the track are denoted by ϕ and θ, respectively.
The resolution in the parameters is studied using simulated events, and estimated from track residuals, which are defined as the differences between the reconstructed track parameters and the corresponding parameters of the generated particles. For each of the five track parameters, the resolution is plotted as a function of the η or p_T of the simulated charged particle. In every bin of η or p_T, the distribution in track residuals defines the resolution.

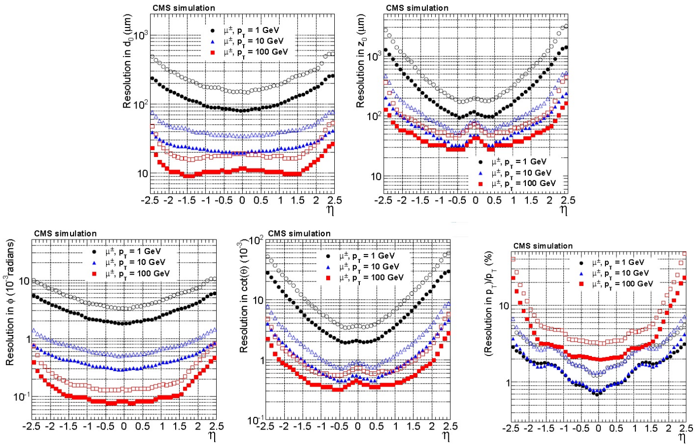

Figure 2.2: Resolution for each track parameter (d_0, z_0, ϕ, cotθ, p_T) as a function of η and for different p_T ranges, [16].

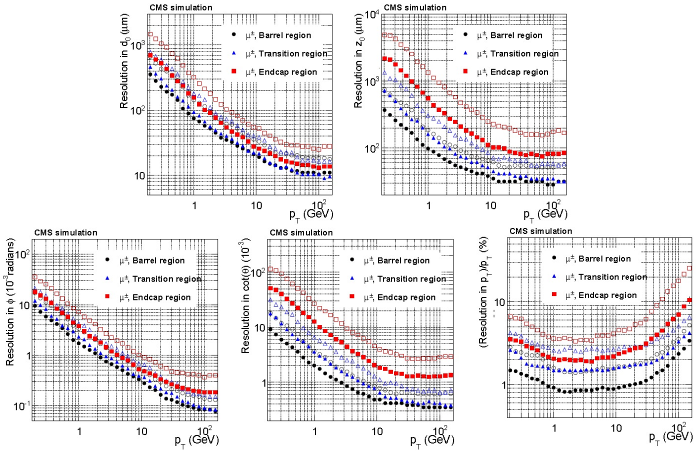

Figure 2.3: Resolution for each track parameter (d_0, z_0, ϕ, cotθ, p_T) as a function of p_T and for different η regions, [16].

2.2.2 Primary vertex

The goal of primary-vertex reconstruction [16] is to measure the location and the associated uncertainty of all proton-proton interaction vertices in each event, including the ”signal” vertex and any vertices from pileup collisions, using the available reconstructed tracks. It consists of three steps; (i) selection of the tracks, (ii) clustering of the tracks that appear to originate from the same interaction vertex, and (iii) fitting for the position of each vertex using its associated tracks.

The track selection involves choosing tracks consistent with being produced promptly in the primary interaction region, by imposing requirements on the maximum value of significance of the transverse impact parameter (< 5) relative to the centre of the beam spot, the number of strip and pixel hits associated with a track (> 1 pixel layers, pixel+strip > 4), and the normalized χ^2 from a fit to the trajectory (< 20). To ensure high reconstruction efficiency, even for minimum-bias events, there is no requirement on the p_T of the tracks.

The tracks are clustered according to the z coordinate of the track, at the point of closest approach to the beamline. This clustering allows for the reconstruction of any number of p-p interactions in the same LHC bunch crossing. The clustering algorithm must balance the efficiency for resolving nearby vertices in cases of high pile-up, against the possibility of accidentally splitting a single, genuine interaction vertex, into more than one cluster of tracks.

The clusters of tracks are fitted with an adaptive vertex fit, where tracks in the vertex are assigned a weight between 0 and 1, based on their proximity to the common vertex. The primary vertex resolution strongly depends on the number of tracks used in fitting the vertex and on their p_T. Results from a study of the primary-vertex resolution in x and z as a function of the number of tracks associated to the vertex, using both minimum-bias and jet-enriched data samples, are shown in 2.4. The resolution in y is almost identical to that in x, and is therefore omitted.

2.2.3 Energy loss

Although the primary function of the strip tracker is to provide hit position information for track reconstruction and precise momentum determination, the strip channel output also provides a measure of energy loss, [16]. That is, the charge collected in a hit cluster is directly proportional to the energy lost by a particle,

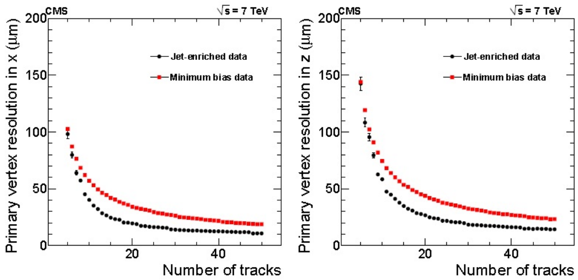

Figure 2.4: Resolution of the primary vertex in x (left) and in z (right), as a function of the number of tracks, using a minimum bias data or jet-enriched data, [16].

largely through ionization, while traversing the silicon.

For reconstructed tracks the angle θ between the track direction and the axis normal to module sensor is well defined for each hit on the track. The instantaneous energy loss per unit path length dE/dx in the silicon is then approximated by the quantity $\Delta E/(\Delta L \cdot sec\ \theta)$, where ΔE is the cluster charge expressed in units of MeV, and ΔL is the thickness of the active volume of the silicon sensor.

The main point in determining energy loss per unit path length is that, for a given medium, dE/dx depends largely on the velocity of the traversing particle. By combining dE/dx information with the measured momentum p of a track, one can determine the mass of the traversing particle.

On the scale of charged particle momenta in CMS collisions, there is only a limited range, near the low end, where the difference in β values is significant enough to distinguish among long-lived hadrons. To this end, the following relation between dE/dx, p, and m is assumed for the momenta below the minimum-ionizing region:

$$dE/dx = K\frac{m^2}{p^2} + C \tag{2.2}$$

The proton line in is used to extract the parameters K and C.

2.3 Upgrade

The performance of the CMS Tracker, which exploits an all-silicon technology, with a pixel and a strip detector, has so far been excellent. Anyway, the foreseen increase of both the instantaneous and the integrated luminosity by the LHC, during the next ten years, will ask for a stepwise upgrade of the CMS tracking detector [18].

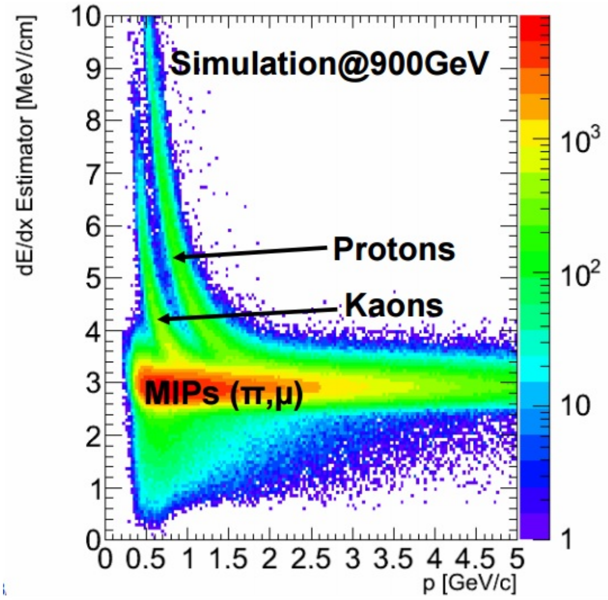

Figure 2.5: Simulation of the energy loss dE/dx as a function of p at 900 GeV in the centre of mass, for some particles.

2.3.1 Phase-1 upgrade

During the 2015-2016 data-taking period the peak luminosity has already doubled the design one, of $10^{34}\ cm^{-2}s^{-1}$. Since the pixel detector is the first part of the tracker that shows limitations in a high-rate enviroment, this will be replaced during the extended winter technical stop 2016-2017. This is referred to as the "Phase-1 Pixel Upgrade".

The goal of the upgraded Phase-1 pixel detector is to be fully efficient at a luminosity of $2 \times 10^{34}\ cm^{-2}s^{-1}$, with less material and with four hit coverage up to $|\eta| < 2.5$. For this reasons, a new pixel detector, with a fourth barrel layer, an extra disk on each side, and a new ROC (ReadOut Chip) has been proposed. The layout of Phase-1 pixel detector compared to the current one is shown in Fig. 2.6.

The upgraded front-end electronics is required to enhance the robustness of the system at high rate. At the design luminosity $10^{34}\ cm^{-2}s^{-1}$, the buffer size and the readout speed of the current pixel ROC will lead to a dynamic inefficiency in the pixel detector of 4% (16%) with 50 ns (25 ns) bunch spacing. The inefficiency increases exponentially with luminosity. The new "PSI46dig" ROC is made in 250-nm CMOS technology, as the present chip (PSI46), and is heavily based on it. Both

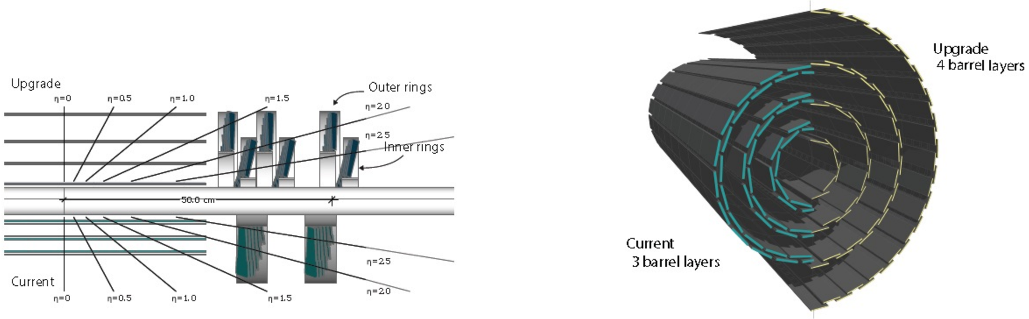

Figure 2.6: Pixer detector layout, comparing the different layers and disks in the current and upgrade pixel detectors. Left; view in the y-z plane, comparing barrel and endcap layers. Right; transverse-oblique view comparing the pixel barrel layers in the two detectors, [18].

chips feature a column drain architecture. To reduce data losses, the depths of data and time stamp buffers have been increased. Simulations indicate that data losses in the first layer will decrease from 16.0% (50%) to 2.4% (4.8%) for a bunch spacing of 50 ns (25 ns) at $2 \times 10^{34} cm^{-2} s^{-1}$.

The current detector contains also significant passive material, that degrades the measurements, due to multiple scattering, photon conversions, and nuclear interactions. An optimization of the mechanics and services, together with a two-phase CO_2 cooling, will provide a substantial reduction of material in the tracking volume. This reduction in the amount of passive material will have a large impact on the track reconstruction efficiency, as well as on electron and photon identification and resolution, thus playing an important role in the reconstruction of the final-state signatures involving electrons and photons.

All the improvements of the Phase-1 Pixel detector have a net effect on the expected performances; pattern recognition, track parameter resolution, vertexing, and b-tagging performance of the upgraded detector are expected to be significantly better than in the current detector.

The loss in tracking efficiency, due to the dynamic data loss and to the effect of the high pile-up expected at 2×10^{34} $cm^{-2} s^{-1}$ and 25 ns crossing time, would be about 10%(16%) for $t\bar{t}$ (muons). For the upgraded detector this is reduced to 1.5%(3.7%) for $t\bar{t}$ (muons). See Fig.2.7 (left) for the $t\bar{t}$ efficiency as a function of pile-up.

The track fake rate rapidly increases with pile-up, but is about a factor of two lower for the upgraded pixel detector, due to the reduced multiple scattering, especially for low momentum tracks, see Fig.2.7 (right) for $t\bar{t}$ average fake rate. Fake tracks are caused by the incorrect association of hits, and are much more likely in regions with more passive material.

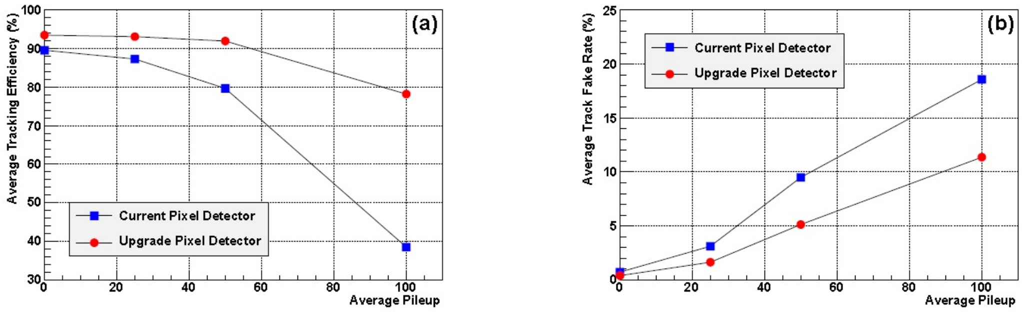

Figure 2.7: Performance of the current pixel detector (blue squares) and upgraded pixel detector (red dots) for $t\bar{t}$ events; average tracking efficiency (left) and fake rate (right) as function of the average pile-up, [18].

The improvement in tracking efficiency, fake rate, impact parameter resolution, and vertexing all contribute to significantly increase the b-tagging performance of the new detector. The tagging of b jets is a key ingredient of many physics analyses; indeed, b jets are often produced in association with the Higgs boson or in its decays, and final states involving b jets are also expected in many new physics models.

No tracker upgrades are foreseen for Long Shutdown 2, LS2 (2018-2019), but a replacement of the innermost layer of the pixel detector might be required after 250 fb^{-1} of integrated luminosity, because the radiation hardness of the detector is not sufficient for operation to the end of Phase 1.

The new pixel detector and the current outer strip tracker will provide optimal tracking performance to CMS through 2020.

2.3.2 Phase-2 upgrade

An upgrade of the accelerator complex is foreseen for the beginning of the next decade, during the Long Shutdown 3, LS3 (2020-2022). The LHC is expected to turn into the HL-LHC, that is planned to deliver an instantaneous luminosity of $5 \times 10^{34}\ cm^{-2}s^{-1}$. The quoted luminosity corresponds to a number of pile-up events which can vary from 100 to 200, according to the operation frequency. This represents a much more demanding condition for the detectors. In such scenario, CMS will eventually collect up to 3 000 fb^{-1}, after several years of operation.

The CMS tracking system will have to be improved in terms of radiation resistance, readout granularity and speed, and capability to contribute information to the Level-1 trigger. A whole new tracking system, both pixel and outer tracker, is hence needed, which will be installed during LS3. This is referred to as the "Phase2 Upgrade" of the CMS tracker [18].

The upgraded tracker will have to provide improved tracking performance in a more challenging enviroment, while producing at the same time fast information for the Level-1 trigger [38]. The tracking should be robust enough in order to sustain operations with up to 200 collisions per bunch crossing in the worst-case scenario of 20 MHz operation, thus increased granularity is required to maintain the occupancy at the level of a few percent.

The detector should provide satisfactory performance up to an integrated luminosity of about 3 000 fb^{-1}, to be compared with the original figure of 500 fb^{-1}; this requires the selection of more radiation hard silicon sensor material, especially for the innermost regions, as well as more stringent criteria in the qualification of electronics and mechanical assemblies.
The amount of material is the most severe limitation on the performance of the present tracker, and it is dominated by electronics and services (notably in the region between barrel and endcap). Thus, to improve the tracking performances at low transverse momentum, the new tracker should foresee a significant reduction of the material. This fact together with the request for an increased granularity drives the choice of technologies for sensors, readout, powering and cooling.
Intense *R&D* activities are going on to identify the most suitable sensors for the Phase-2 tracker. Wafers of different materials, polarities, and thickness, equipped with test structures and test sensors with different strip lengths, pitches, and strip widths have been tested, and irradiated with both protons and neutrons.

At HL-LHC, the combinatorial background poses also problems to the Level-1 trigger, to the point where it is not possible to keep the trigger rate within the nominal range, manteining reasonably low cuts on the trigger variables. The CMS collaboration plans to improve the trigger, for example by installing a fourth layer of the Cathode Strip Chambers muon detector, and re-designing the Level-1 trigger hardware.

Nevertheless, these improvements will be insufficient for the HL-LHC luminosity. A large event-rate reduction factor is currently achieved in the High-Level software Trigger by using information from the tracker. Including this information in the Level-1 processing would allow a much better rejection of combinatorial background. The collaboration is therefore studying the option of sending tracking information in real time to the Level-1 trigger.

In addition, to reduce the volume of the trigger data, low p_T tracks are locally rejected. So-called "p_T modules" will perform the discrimination between high and low p_T tracks. Only Level-1 tracks with p_T above a certain threshold (e.g. 2 GeV) are formed at the back-end. This could be achieved by performing an on-module p_T selection, exploiting the CMS 3.8-T magnetic field.
The basic concept consists of correlating signals in two closely-spaced sensors; the distance between the hits in the x-y plane is correlated with the particle p_T, allowing the p_T discrimination to be made. A pair of hits that fulfils the selection cut is called a "stub" (Fig. 2.8). For a given p_T, the distance between the hits forming the stub is larger at larger radii. Thus, the effective p_T cut provided by the modules in the different locations has to be optimized, by tuning both sensor spacing and acceptance window. The coordinates of stubs selected by the p_T modules are sent to the trigger electronics at the back-end, where they have to be combined to form Level-1 tracks.

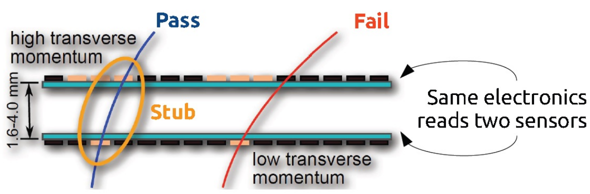

Figure 2.8: Sketch illustrating the stub selection, exploiting the correlation of the two hits signals in two closely-spaced sensors, [38].

Two types of p_T modules are under development to instrument the radial region below (PS modules) and above 40 cm (2S modules), Fig.2.9.

- 2S modules; constitute a sandwich of two strip sensors, read out at the edges, by the same set of front-end ASICs that implements the correlation logic, on a high-density substrate. They are two sensors of about 10×10 cm^2 with

5-cm-long strips and a pitch of 90 μm, mounted on a mechanical structure that provides support and cooling.
The sensors are wire-bonded from top and bottom to the readout hybrids, each of them carries eight CMS Binary Chips (CBCs) plus a Data Concentrator chip. The estimated power consumption for the readout electronics, including the correlation logic, is below 2 W, comparable to the lowest values in the present tracker.
The main limitation of this type of module is the lack of segmentation in the z direction. In order to implement effective isolation cuts on calorimeter clusters, the Level-1 tracks must also have a reasonable precision in the z coordinate. In addition, the relatively long strips limit the use of this module to the radial region above 40 cm, because of the occupancy.

- PS modules; based on the assembly of one strip and one pixel sensor, they overcome the limitation of the 2S modules, and can be emplyed at radius lower then 40 cm in the tracker.
  The PS module is half as large as 2S module. The upper sensor carries short strips with dimensions of 2.5 $cm \times 100\ \mu m$, which are wire-bonded to hybrids with readout chips. The lower sensor is structured with large pixels of dimensions 1.5 $mm \times\ 100\ \mu m$, and is bump-bonded to dedicated readout chips.
  Compared to the 2S module, this concept offers a sufficiently precise measurement of the z coordinate from the pixellated sensor, while the 2.5-cm-long strips allow the module to be used down to 20-25 cm radius. On the other hand the power consumption is expected to be more than 4 W, dominated by the pixel ASICs.

Both 2S and PS modules carry a DC-DC converter and a GBTX chip plus opto-electrical converters on service hybrids. *R&D* on the CBC is well advanced. The 2×127 channel chip is fabricated in 130 nm CMOS technology, and features unsparsified binary readout. The chip receives data from both sensors. After amplification and hit detection, clusters are formed. Following a cluster width discrimination step, clusters from the lower and upper sensor, within a programmable window, and with programmable channel offset, are correlated. Stubs are formed and passed to the Data Concentrator.

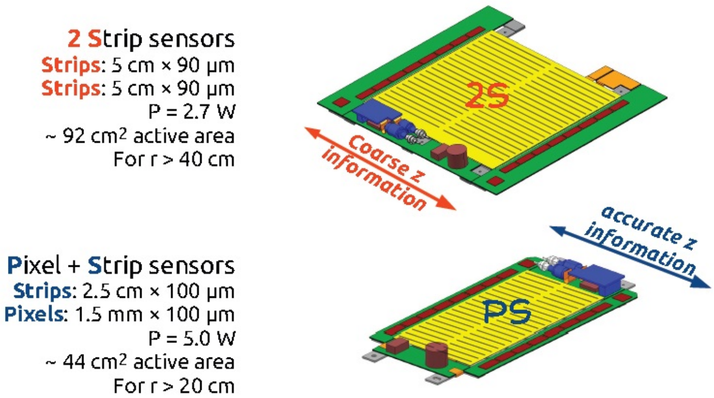

Figure 2.9: Model of a 2S (top) and a PS (bottom) p_T module [38].

Chapter 3

Hunting for new physics

3.1 Current state

The discovery of the Higgs boson at the LHC was announced together by the CMS and ATLAS collaborations in 2012, and has opened a new exciting era for the high-energy physics. Albeit the huge efforts put in by these experiments, the hunting for new particles has been unsuccessful so far, and the robustness of the Standard Model (SM) has been continuously confirmed.
However, unexplained phenomena and problems, for example the dark matter, the difficulty of incorporating gravity, and the hierarchy problem, suggest that beyond the Standard Model (BSM) physics is required to accurately describe the universe we observe. Many such new physics models exist, conventionally separated into supersymmetry models and all other BSM models, referred to as exotica. This provides a rich terrain to probe experimentally, and both ATLAS and CMS experiments at the Large Hadron Collider (LHC) have run extensive physics programs to cover as many scenarios as possible.

The current Run II of the LHC started in June 2015; the machine reached an energy of 13 TeV in the centre of mass of the colliding protons, and collected an integrated luminosity ot 4.2 fb^{-1} and fb^{-1} for 2015 and 2016 data respectively, marking new records for the hadron colliders. These new experimental conditions are providing a greater statistics and cross section, for the discovery of new particles or for the extension of the exclusion limits in their search.

The main aims of the ongoing Run II are a detailed characterization of the Higgs boson and the continuance of the search for new physics.

3.2 Susy and exotic world

For the sake of simplicity, the new physics searches are splitted in Susy and exotic searches [19], [20]. In the first group are all the analyses based on the Supersymmetry model, in the second one can find all the other kind of beyond Standard Model analyses.

Supersymmetry (SUSY) provides a solution to the hierarchy problem, which refers to divergent corrections to the Higgs mass squared parameter, due to loop diagrams of couplings between the Higgs and massive SM particles.
A symmetry relating fermions to bosons is proposed, resulting in a supersymmetric partner for each SM particle, with spin differing by 1/2. All SM fermions will have a SUSY boson partner, and all SM bosons will have a SUSY fermion partner. These SUSY partners are at a displaced mass scale, due to the breaking of supersymmetry, the exact nature of which is not fixed, except the fact that the added terms must be gauge invariant.
Returning to the divergent Higgs mass squared correction terms, there is now a cancellation between the divergent loop corrections of the SM particles, and the equivalent terms from their supersymmetric partners. Models with lights SUSY partners of the heavier SM particles, are referred to as more "natural", as the cancellations will be closer to zero.
In addition to solving the hierarchy problem, SUSY also leads to the unification of the strong, weak, and electromagnetic forces, and can provide suitable dark matter candidates. This has caused it to be considered one of the most popular BSM theories, and both ATLAS and CMS have an extensive range of analyses covering many of the possible phenomenologies resulting from many additional parameters which are not strongly constrained.

In addition to SUSY, many other BSM theories are considered by both experiments, we mention here just few examples.

For istance, the SM fermions may be composite objects, connected by a new interaction, at an energy scale higher than the one explored experimentally so far. Such a new interaction, at an energy scale Λ, much higher than the parton collision energy, would be observed as contact interactions between SM quarks and/or leptons. Depending on the properties of the new interaction and substructure particles, various contact interaction terms and different interference terms with the SM processes are possible. A set of benchmark interaction terms is considered in the searches.

The large range between the EWK (electroweak) scale (1 TeV) and the Planck scale (10^{16} TeV) raises the question why the gravity is so weak, compared to the other forces. A possible solution is given by Randrall-Sundrum (RS) model of extra spacial dimensions. It assumes that gravity can propagate in warped extra dimentions, appearing weak in the standard known dimensions, to which the other forces are restricted. The experimental evidence for this model are excitations of the gravitons, referred to as Kaluza-Klein excitations. They could be measured as narrow resonances, decaying into a pair of bosons, jets or leptons.

In principle, all these searches are based on similar methods; defining regions in which to compare the number of expected and observed events. There are also some new physics scenarios, whose signal can be distinguished from the background in quite specific and novel ways, for example the long-lived particles.
Background estimation methods tend to vary from analysis to analysis, with some normalising MC simulations, and some employing more sophisticated data-driven or semi-data-driven techniques.

Due to the number and diversity of the considered models, and the similarity of the signatures many would give at the LHC, these searches can be better categorised by the search methods and final states, rather than the model.

The dilepton plus dijet final state is one of the more promising channels, in the new physics search; it is sensitive to many theoretical models beyond the Standard Model. They can include scalar leptoquarks of the three generations and heavy Majorana neutrinos, e.g. arising from the seesaw mechanism, in the context of a LR-symmetry extension or in a compositeness scenario, as we will discuss in the following sections.

3.3 Leptoquarks and heavy neutrinos models

In this section, a very incomplete theoretical indroduction is presented about models that foresee the existence of leptoquarks and heavy neutrinos, and that can produce, in some benchmark process, a final state of two same flavour leptons plus two jets, considered in various analyses of CMS; [7], [8], [9], [10], [11], [12], [13].

Several models beyond the Standard Model (BSM), like Grand Unification, compositness, superstrings and technicolor include leptoquarks (LQ) of the three generations. These new particles are scalar or vector bosons which carry non-zero leptonic and baryonic number, color charge and fractional electric charge.
Experimental limits suggest that their research should be mainly focused on LQ pair production, via gluon fusion or quark annihilation, and on the dominant decay process in a lepton and a quark of the same generation of the LQ. In these theories, the free parameters are the LQ mass (M_{LQ}) and the BR decay in a charge lepton plus a quark, usually denoted as β. Since the production is in pairs, the final state of this kind of processes presents two same flavour leptons plus two jets.

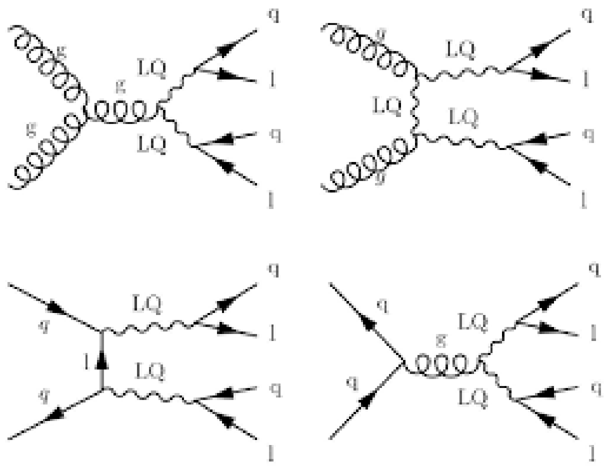

Figure 3.1: Some Feynman diagrams for the pair production of leptoquarks.

The SM assumes that the neutrinos of the three generations are massless, however, the observation of neutrino oscillations implies a non-zero mass, and definitely points to new physics models.
The leading model that naturally generates light neutrino masses is the "seesaw" mechanism that, in its simplest implementation, justifies the smallness ot the observed neutrino masses, introducing a heavy neutrino state N. The SM neutrino mass is given by $m_\nu \sim y_\nu^2 v^2/m_N$, where y_ν is a Yukawa coupling of ν to the Higgs field, v is the Higgs vacuum expectation value in the SM, and m_N is the mass of a new heavy neutrino state, N.
If the seesaw mechanism was the right way to explain the masses of the known neutrinos, both the light and heavy neutrinos would have to be Majorana particles,

so processes that violate the lepton number conservation by two units would be possible.
Therefore, searches for heavy Majorana neutrinos at the colliders are very important in resolving the nature of neutrinos and the origin of masses.

A natural way to confer mass to neutrinos is provided by the Left-Right Symmetry extension, LRSM, in which the SM group $SU_L(2)$ has a right-handed counterpart and the symmetry group is $SU_C(3) \otimes SU_L(2) \otimes SU_R(2) \otimes U(1)$, originally introduced to explain the reason of parity non conservation in weak interactions. The new $SU_R(2)$ group, similar to the $SU_L(2)$, predicts the existence of three new gauge bosons, $W_R^{\pm}$ and Z', and three heavy right-handed neutrino states N_ℓ ($\ell = e, \mu, \tau$), partners of the light neutrinos states ν_ℓ, and can explain the neutrinos' mass hierarchy in the context of the seesaw mechanism.
A refererence process allowed by this model is the production of a heavy neutrino through a W_R boson and its decay into a same flavour lepton plus another W_R which decays hadronically: $qq \to W_R \to \ell + N_\ell \to \ell + (W_R + \ell) \to \ell + (qq') + \ell$, this process gives two jets and two same flavour leptons in the final state.

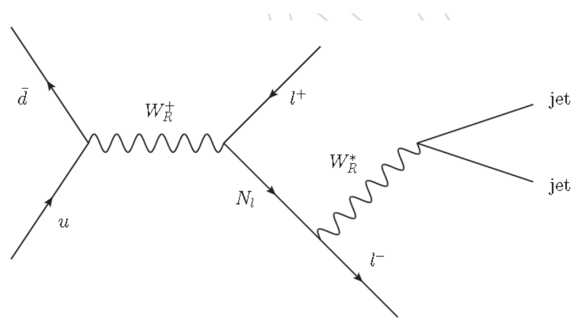

Figure 3.2: Feynman diagram of the heavy neutrino production through a W_R boson.

3.4 Run I searches

Using an integrated luminosity of 19.7 fb^{-1}, collected by CMS, during Run I, at an energy of 8 TeV in the centre of mass, several searches for heavy Majorana neutrinos and leptoquark has been conducted, that have in common the dilepton plus dijet final state.
A first analysis [9] considers a Type-1 seesaw model with at least one heavy neutrino,

that mixes with the SM neutrinos. The neutrino's mass and $V_{N\ell}$, the mixing element describing the mixing of the heavy neutrino with the SM neutrino, are the free parameters of the model. The heavy Majorana neutrinos (N), produced togheter with a lepton, decays into a W boson, featuring hadronic decay, and another lepton. This gives a final signature of two jets and either two same sign electrons or a same sign electron-muon pair. The data are found to be consistent with the expected Standard Model background, and limits are set on the cross section times branching fraction for production of heavy Majorana neutrinos in the mass range between 40 and 500 GeV.
A similar search [8] is performed for heavy Majorana neutrinos (N), using an event signature defined by two same-sign muons and two jets, adopting a more phenomenological approach, in the same range of neutrino's mass. No excess of events is observed beyond the expected Standard Model background, and new limits are set.
Finally, a search for heavy, right-handed, neutrinos $N_\ell(\ell = e, \mu)$ and right-handed W_R bosons, which arise in the left-right symmetric extension of the standard model, has been performed [7]. The search was based on a sample of two same-flavour lepton plus two jet events. For models with strict left-right symmetry and assuming only one N_ℓ flavor contributes significantly to the W_R decay width, the region in the two-dimensional $(M(W_R), M(N_\ell))$ mass plane excluded, at a 95% confidence level, has been significantely extended. The $\mu\mu jj$ and $eejj$ channels have been investigated, and a broad excess around $M_N = 2,2$ TeV has been measured, with respect to the cross section of the SM background, corrisponding to 2.8 σ. This cannot be explained considering the LR model parametrization of the analysis (Fig. 3.3).

Concerning the LQ scenario, with the LQ produced in pairs, it has been possible to exclude, at the 95% of confidence level, for the first generation (LQ_1) $M_{LQ1} < 950(845)\ GeV$ with $\beta = 1(0.5)$, for the second generation (LQ_2) $M_{LQ2} < 1070(785)\ GeV$, with $\beta = 1(0.5)$ [11], and for the third one (LQ_3) $M_{LQ3} < 740\ GeV$ [12], with $\beta = 1$. An excess of $2.4(2.8)\sigma$ with respect to the predicted contribution from the SM background has been observed at around 650 GeV in the $eejj(e\nu jj)$ final state. This excess cannot be explained within the LQ_1 model considered in the analysis [11] (Fig. 3.4).

To summarize, the CMS measurements in the Run I, looking for first generation leptoquarks and heavy neutrinos, have shown two significant excesses, in the final state with two electrons and two jets, in analyses performed at the center of mass energy of 8 TeV, using 19.7 fb^{-1}. No excess has been observed in the dimuon plus dijet channel. The ditau plus dijet signature has not yet been explored for the heavy neutrinos specific search, but only for searches motivated by leptoquarks models, in the final state where the tau pair is produced with two b or two t quarks, giving results in agreement with the SM expectation.

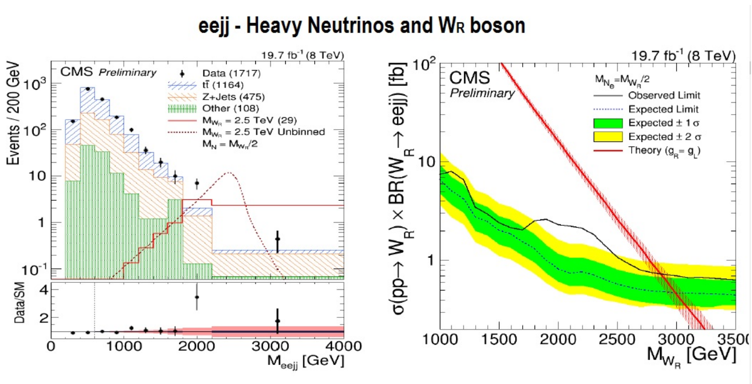

Figure 3.3: Results of the heavy neutrino's and W_R search of Run I. On the left the distribution of the invariant mass of the system. On the right the exclusion plot showing the excess, [7].

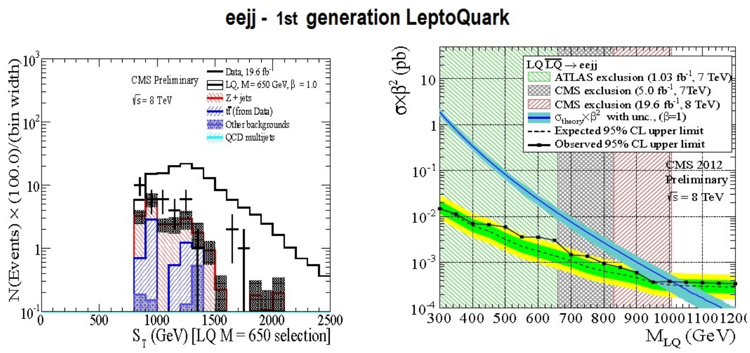

Figure 3.4: Results of the first generation leptoquark search of Run I. On the left the distribution of the S_T, that is the p_T sum of the four objects in the final state. On the right the exclusion plot showing the excess, [11].

3.5 Run II searches

Using the first 13 TeV data collected by CMS, during the Run II of LHC, new analyses have been pubblished, referring to heavy neutrinos and leptoquark searches.

A search for heavy, right-handed neutrinos, N_ℓ , and right-handed W_R bosons, which arise in the left-right symmetric extensions of the standard model, has been performed [10]. The search focuses on the scenario where the W_R and N_ℓ decay chains result in a pair of high-p_T τ leptons, which decay hadronically, besides two high-p_T jets.
The analysis is performed using 2.1 fb^{-1} of data, collected by the CMS experiment, in 2015, at 13 TeV. For models with strict left-right symmetry and assuming that only the N_τ flavor contributes significantly to the W_R decay width, W_R masses below 2.35 (1.63) TeV are excluded at 95% of confidence level, assuming the N_τ mass is 0.8 (0.2) times the mass of W_R boson. Limits are also set on pair production of third generation scalar leptoquarks.

A second search is presented for pair-produced second generation scalar leptoquarks, using 2.7 fb^{-1} of data collected by CMS during the 2015 [13] . A final state signature, containing two high p_T muons and at least two jets, is taken into account. Second generation scalar leptoquarks with masses less than 1165 (960) GeV are excluded, when assuming the leptoquark branching fraction to a charged lepton and a quark $\beta = 1$ ($\beta = 0.5$).

Both these searches of the Run II have not found any excess respect with the SM background.

Search	Exclusion	Excess
Leptoquarks (8 TeV) [11]	$M_{1st-gen} < 1010(850)$ Gev $M_{2nd-gen} < 1080(760)$ GeV for $\beta = 1$ ($\beta = 0.5$)	2.4 σ in $eejj$, 2.6 σ in $e\nu jj$ No
Leptoquarks (13 TeV) [13]	$M_{2nd-gen} < 1165(960)$ GeV for $\beta = 1(\beta = 0.5)$	No
Leptoquarks and heavy neutrinos (13 TeV) [10]	$M_{3rd-gen} < 740$ GeV $M_{W_R} < 2.35(1.63)$ TeV with $M(N) = 0.8(0.2)M_{W_R}$	No No
W_R and heavy neutrinos (8 TeV) [9]	$M_{W_R} < 3$ TeV	2.8σ in $eejj$, no in $\mu\mu jj$
heavy Majorana neutrinos type-1 seesaw (8 TeV) [8]	on $\|V_{\mu N}\|^2$, $\|V_{eN}\|^2$ $\|V_{eN}V^*_{\mu N}\|^2/(\|V_{eN}\|^2 + \|V_{\mu N}\|^2)$ mass range 40-500 GeV	No

Table 3.1: CMS results in searches for leptoquarks and heavy neutrinos in Run I and Run II.

3.6 A new search for heavy neutrinos

Several theoretical attempts have been made to justify the excess in the electron channel, observed in a search for heavy neutrinos within LR-symmetry extension and in a search for leptoquarks of first generation during Run I. Some of them are; a LR-symmetry extention with $g_L \neq g_R$, the W_R and Z' gauge boson production and decay, R-parity violating processes via the resonant production of a slepton, and models which connect leptoquarks to dark matter.
Besides the extensions of the SM that has been already considered, in order to clarify the nature of these deviations of the data from the SM expectations, we have studied a model in which the heavy Majorana neutrino arises, assuming the compositeness of fermions, [14] .

Within a composite model for heavy Majorana neutrinos, a benchmark process with a same flavour dilepton plus dijet signature is taken into consideration, to provide a possible explanation of the excess, and to extend the limits on the parameters of the heavy neutrinos search, exploiting the Run II data. The new model and the analysis strategy will be described in the two following chapters.

Chapter 4

A new model for heavy neutrinos

4.1 A composite heavy Majorana neutrino

Compositeness is a possible scenario beyond the Standard Model [14] . In this approach, quarks and leptons are assumed to have an internal substructure, which should become manifest at some sufficiently high energy scale, the compositeness scale Λ. Ordinary fermions are thought to be bound states of some, as yet unobserved, fundamental constituents generically referred to as "preons".

Quite natural and model independent properties of this picture are;

- the prediction of heavier excited states of the SM fermions, such as q^*, ℓ^*, ν^*, with masses $m^* \leq \Lambda$,
- the existence of a contact interaction, a residual force of the internal dynamics, acting between ordinary fermions and also between ordinary and excited fermions.

The SM fermions are expected to interact with the heavier excited states, such as the heavy neutrinos of the three generations (N_e, N_μ, N_τ), by means of both contact and gauge couplings.

Let us consider here the various possible composite models, with respect to the idea of introducing lepton number violation (LNV), via a composite Majorana neutrino. For simplicity's sake, we are going to show explicitly the singlets and doublets only for the first generation.

- Homo-doublet model;
  contains a left handed excited doublet and a right handed excited doublet

$L_L^* = \begin{pmatrix} \nu_L^* \\ e_L^* \end{pmatrix}$, $L_R^* = \begin{pmatrix} \nu_R^* \\ e_R^* \end{pmatrix}$.
Typically the left and right handed doublet are assumed to have the same mass. The two left and right Majorana fields, with the same mass, combine to give a Dirac field, with a Dirac mass. The homo-doublet model cannot provide Majorana excited neutrinos and, hence, lepton number violation (LNV). This becomes only possible, introducing a difference of mass between the left and right doublet (mixing) or, in other words, a breaking of the LR symmetry.

On the other hand, if we do not want to introduce a mass splitting between the left and right components, we can account for LNV, advocating models which naturally accomodate a Majorana neutrino. These are the two following.

- Sequential type Model;
  contains a left handed excited SU(2) doublet and a right handed SU(2) singlet $L_L^* = \begin{pmatrix} \nu_L^* \\ e_L^* \end{pmatrix}$; e_R^*, $[\nu_R^*]$. The notation $[\nu_R^*]$ means that ν_R^* is necessary if the excited neutrino is a Dirac particle, while it could be absent for a Majorana excited neutrino.

- Mirror type Model;
  assumed to contain a right handed doublet and left handed singlet e_L^*, $[\nu_L^*]$; $L_R^* = \begin{pmatrix} \nu_R^* \\ e_R^* \end{pmatrix}$. We may suppose that there is no left handed excited neutrino (ν_L^*), associate to ν_R^* a Majorana mass term, and treat ν^* as a Majorana particle.

The above mirror type model is the one to which we will refer our detailed simulation of the same sign dilepton signature at the Run II of the LHC.

For an excited Majorana neutrino $N = \nu^*$, arising from this model, the relevant charged current of the gauge interaction is;

$$\mathcal{L}_G = \frac{gf}{\sqrt{2}\Lambda}\bar{N}\sigma_{\mu\nu}\ell_L\partial^\nu W^\mu + h.c.$$

Contact interactions between ordinary fermions and between ordinary and excited fermions may arise by constituent exchange and/or by exchange of the binding quanta of the new unknown interaction. The dominant effect is expected to be given by the dimension-6-four-fermion interaction, which scales with the inverse square of the compositeness scale Λ;

$$\mathcal{L}_C = \frac{g*^2}{2\Lambda^2} j^\mu j_\mu$$

$$j_\mu = \eta_L \bar{f}_L \gamma_\mu f_L + \eta'_L \bar{f}^*_L \gamma_\mu f^*_L + \eta''_L \bar{f}^*_L + h.c.$$

The gauge interactions and the contact interactions have been both implemented in the process generation.

A heavy Majorana neutrino N can be produced, in association with a lepton ℓ in p-p collisions. The production $q\bar{q}' \rightarrow \ell N$ proceeds through flavour conserving but non-diagonal terms, which couple excited states with ordinary fermions. We have conducted a study with the CalcHEP generator which shows that the production cross section of the heavy neutrino is dominated by the contact interaction, greater then the gauge one of 3-4 orders of size, depending on the heavy neutrino's mass hypothesis (Fig. 4.1).

The heavy composite Majorana neutrino can decay again through both gauge and contact interactions, though in this case the dominant interaction changes depending on Λ and neutrino's mass. The possible decays are;

$$N \rightarrow \ell q\bar{q}', \; N \rightarrow \ell^+\ell^-\nu(\bar{\nu}), \; N \rightarrow \nu(\bar{\nu})q\bar{q}'.$$

The decay channel with the highest BR (branching ratio) is $N \rightarrow \ell q\bar{q}'$ (see the corresponding decay amplitudes in Fig. 4.2). For that reason, we chose as our benchmark process: $pp \rightarrow \ell N \rightarrow \ell(\ell q\bar{q}')$. Although the dilepton plus dijet final state can occur via a virtual (t-channel) or a resonant (s-channel) neutrino, the production of a virtual neutrino is negligible. Thus, the final cross section is calculated considering only the s-channel, see the Feynman diagram in Fig.4.4.

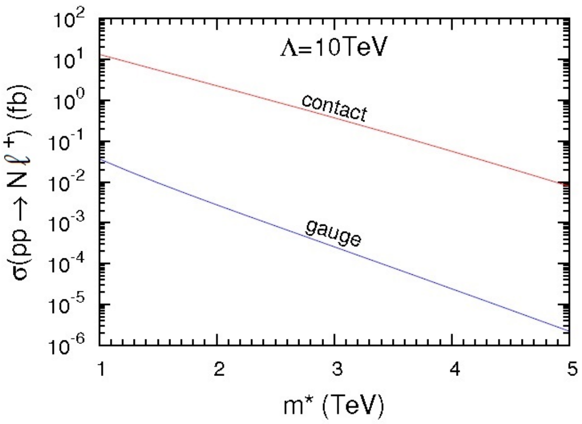

Figure 4.1: Contribution of gauge (blue line) and contact (red line) interaction to the cross section of production of the heavy neutrino, in the process $pp \to N_\ell \ell^+$ with $\ell = e, \mu$, as a function of its mass m^*, setting $\Lambda = 10$ TeV.

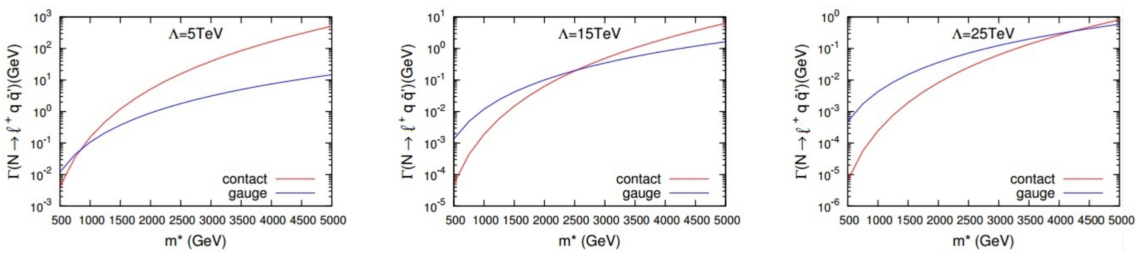

Figure 4.2: Contribution of gauge (blue line) and contact (red line) interaction to the decay amplitude of the heavy neutrino, in the process $N \to \ell^+ qq'$, where $\ell = e, \mu$, as a function of its mass m^*, considering three different values of Λ; 5, 15 and 25 TeV.

In this analysis the final state $\ell\ell jj$ will be considered, particularly the cases in which ℓ is either an electron or a muon, giving rise to the $eejj$ or $\mu\mu jj$ channel. The dacay vertex of this process can see the competition of the contact and gauge interactions, which depends on the choice of the free parameters of the model; the neutrino's mass, m^*, and the energy scale, Λ.

We decided to do not ask for any charge requirement for the final state leptons in the analysis, because we would like to be experimentally sensitive to both the following hypoteses.

- Same sign leptons, obtainable only via a Majorana neutrino and a leptonic number violation $\Delta L = \pm 2$.

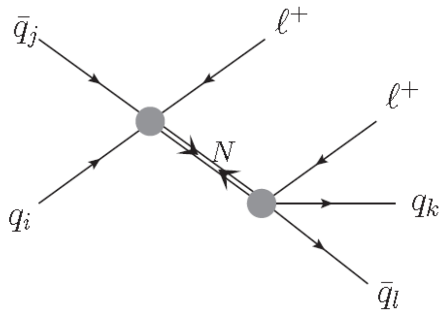

Figure 4.3: Feynman diagram of the benchmark process

- Opposite sign leptons, possible via both Majorana and Dirac neutrino, with the leptonic number conservation.

4.2 Kinematical and topological study

A kinematical and topological study has been performed at generator level on signal samples at $\Lambda = 5$ TeV and for three values of the heavy neutrino's mass; 500, 1500 and 2500 GeV, at the energy of 13 TeV in the centre of mass. We show this study only for the $\mu\mu jj$ channel, but all the considerations can be extended to the $eejj$ channel as well.
The considered objects are the partonic muon (Mupart) and the products of the heavy neutrino's decay; the other muon (Muhn), the leading quark (q1), and the subleading quark (q2). Only if we have a gauge decay vertex, the two quarks originate from a W Standard Model boson. Finally we take into account the heavy neutrino itself (N).

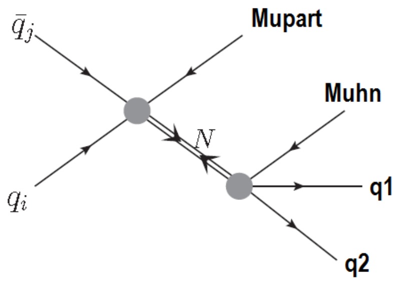

Figure 4.4: Feynman diagram of the benchmark process.

The topology of the signal has been explored, by considering the angular opening between each pair of objects in the finale state, and between the heavy neutrino and each one of them. We show the distributions for the variable ΔR (Fig.4.5,4.6), defined as $\Delta R = \sqrt{(\Delta\eta)^2 + (\Delta\phi)^2}$, and for $cos(\Delta\phi)$ (Fig.4.7,4.8).
The kinematical behaviour in terms of p_T and η is shown for all the final state objects and for the heavy neutrino (Fig.4.9,4.10).

The two muons tend to have a back to back configuration in all the cases of mass. The products of the heavy neutrino's decay show a more collinear topology at a mass of 500 GeV, respect with the other two cases of 1500 and 2500 GeV, where we observe a greater angular opening. This is more evident for the pair of quarks that are angularly very close at 500 GeV, see Fig.4.5 and Fig.4.7.

The explanation for this behavior is that the curves of gauge and contact amplitude at the decay vertex, setting $\Lambda = 5$ TeV, intersect in corrispondence of a mass value of about 1000 TeV (Fig.4.2). Thus, at a mass of 500 GeV we are dominated by the gauge contribution, that implies a forward decay due to the boost of the neutrino ($M_N >> M_W$) and the mediation of a W boson that correlates the two quarks.
From 1 000 GeV forward, the greater is the mass, the stronger is the contact contribution. A contact vertex implicates a decay of the heavy neutrinos in three objects, without any W mediation. This results in a more randomized topology for the decay products and in a clear separation in the ΔR distribution of the two partons.
The lower plot on the right of Fig.4.5 shows the peak at low values due to the gauge events and the broader peak at higher values ascribable to the contact decays, for the $\Delta R(q1, q2)$ distribution.

In addition, we learn from the topological study, that there is always a not negligible probability, greater then 10%, to produce events with two very collinear quarks ($\Delta R < 0.4$), which end up in merged jets at reconstruction level. It will be necessary to apply specific techniques and algorithms, to deal with such overlapped jets, referred to hereafter as "fat jets".

Secondly, both the kinematical and topological study suggest that there is not a clear mass indipendent pattern to define a criterion for distinguishing the partonic muon from the heavy neutrino's muon. The topological (Fig.4.5,Fig.4.7) and kinematical (Fig.4.9,4.10) behaviour of the two muons varies with mass, due to the variable contribution of gauge and contact interactions. Thus, we abandon the purpose of tagging the muon origin.

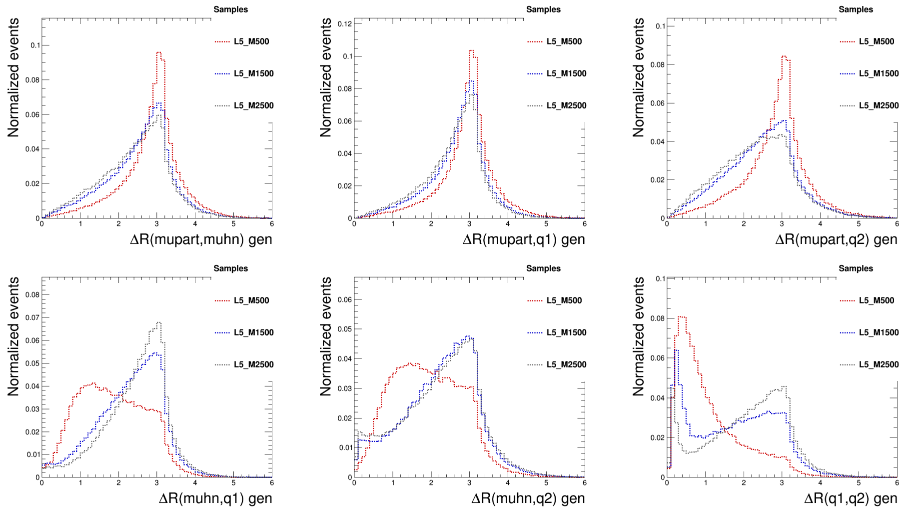

Figure 4.5: The ΔR distribution of all the possible couples of objects in the final state.

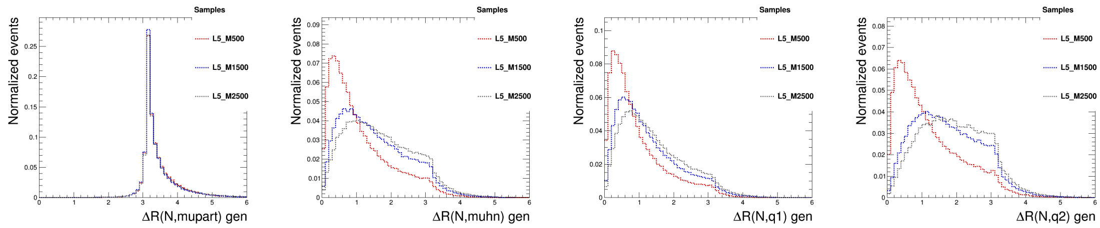

Figure 4.6: The ΔR distribution between the neutrino and each one of the final state objects.

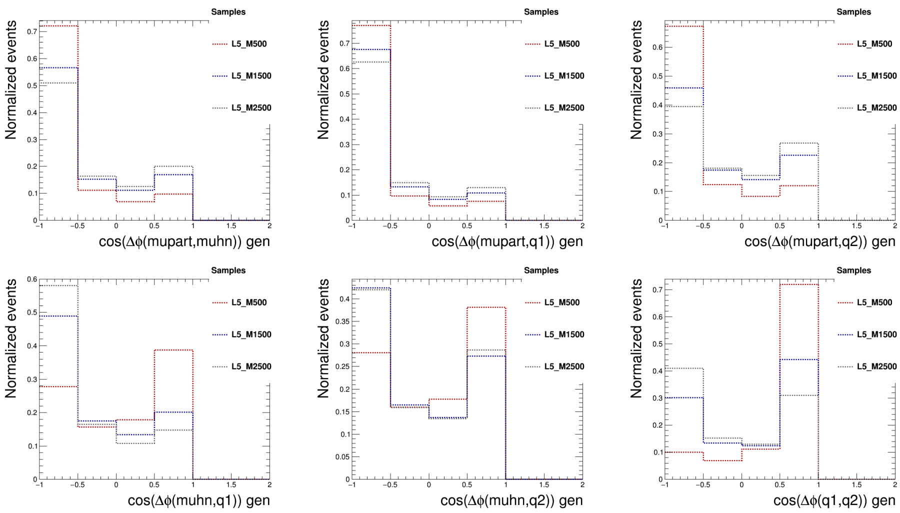

Figure 4.7: The $cos(\Delta\phi)$ distribution of all the possible couples of objects in the final state.

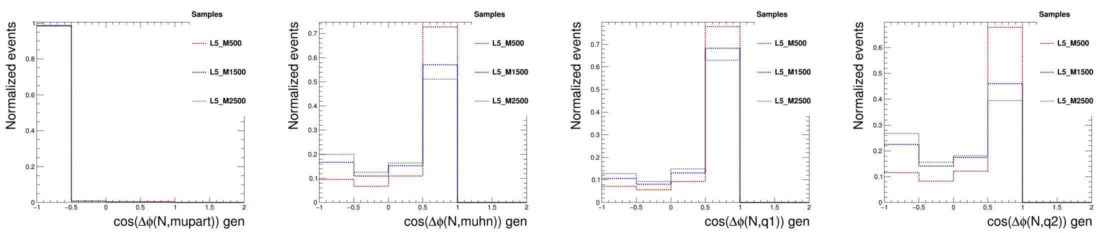

Figure 4.8: The $cos(\Delta\phi)$ distribution between the neutrino and each one of the final state objects.

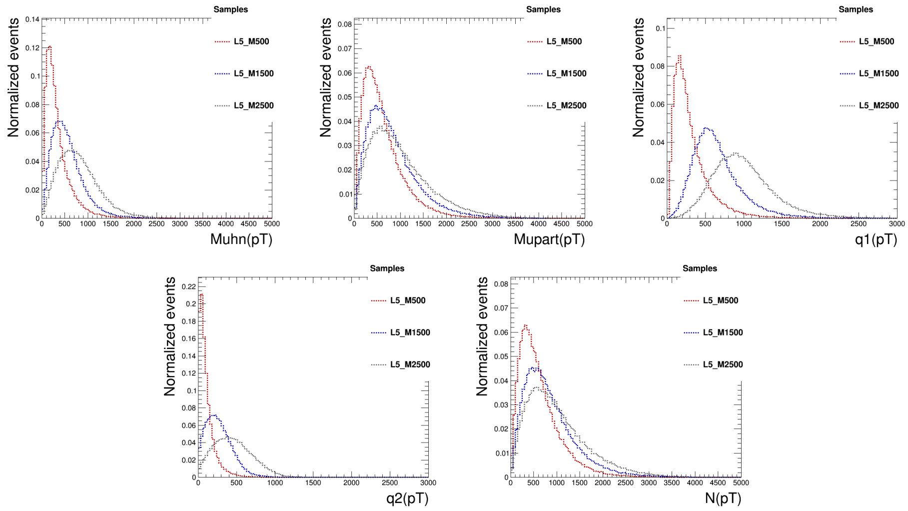

Figure 4.9: The p_T distribution of the final state objects and of the heavy neutrino.

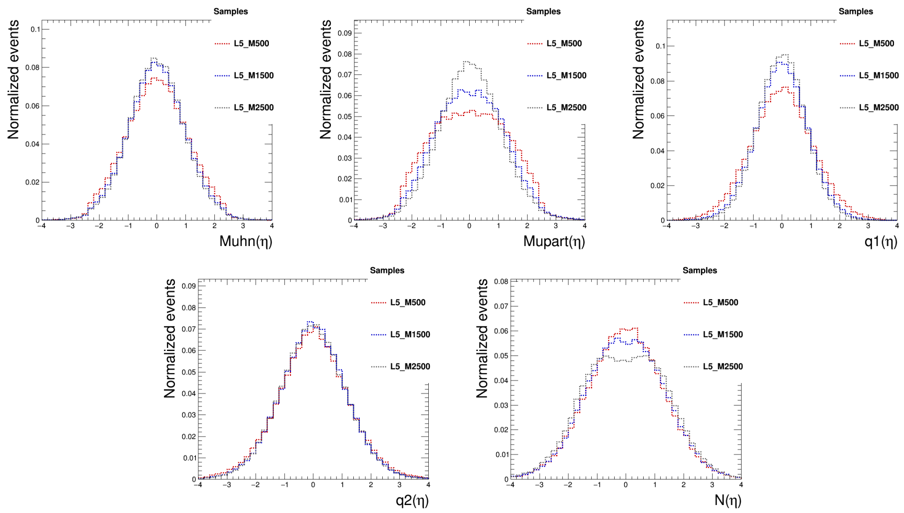

Figure 4.10: The η distribution of the final state objects and of the heavy neutrino.

Chapter 5

Analysis' strategy

5.1 Datasets

The data used in this analysis were collected during the 2015 proton-proton run, were reconstructed using $CMSSW\_7\_6\_3$, and were preselected for good luminosity sections, using the JSON file $Cert\_13TeV\_16Dec2015ReReco\_Collisions15\_25ns\_JSON.txt$.

The data samples considered for the $eejj$ and $\mu\mu jj$ channels, each corresponding to an integrated luminosity of 2.3 fb^{-1}, are reported in Table 5.1.

The Monte Carlo samples used were produced within the campaign;
$RunIIFall15MiniAODv2\text{-}PU25nsData2015v1\_76X\_mcRun2\_asymptotic\_v12\text{-}v1$. The list of samples for the backgrounds, with their cross sections at 13 TeV, is reported in Table 5.2.
The $t\bar{t}$, tW, WW, inclusive DY, and inclusive $W + jets$ backgrounds are calculated at the NNLO, the WZ and ZZ backgrounds are calculated at the NLO; whilst the binned DY and the binned W + *Jets* are calculated at the LO, and their cross sections are multiplied for a k-factor.

The MC samples for the signal are generated with CalcHEP, for each mass point of the heavy neutrino's mass, ranging from 500 to 4500 GeV, every 1000 GeV and for the Λ parameter set at a value of 5 TeV. The list of the simulated signal samples, together with their cross section at 13 TeV is shown in Table 5.3.

The MC samples have been adjusted according to the following corrections.

- For $DYJetsToLL\_M\text{-}50\_TuneCUETP8M1\_13TeV\text{-}madgraphMLM\text{-}pythia8$ and $WJetsToLNu\_TuneCUETP8M1\_13TeV\text{-}madgraphMLM\text{-}pythia8$, only events with gen HT< 100 GeV are considered, where gen HT is the hadronic activity of the event at gen level.

- Events are normalised to the integrated luminosity of data.
- Events are reweighted, in order to account for differences between the distributions of the number of pile-up interaction, compared to data. The generated pile-up conditions in MC sample are meant to cover the expected pile-up scenario for each run of 2015. Anyway, the data-taking distributions could be not exactly matched by MC ones. Therefore, the measured distribution from data H_{data}(i) is divided by the MC one, H_{sim}(i), to obtain the final distribution of weights $w(i)$, as a function of the number of interactions per bunch crossing, i;
$$w(i) = \frac{H_{data}(i)}{H_{sim}(i)}. \tag{5.1}$$
- Events are weighted considering the lepton scale factors [25], [26].

Data sample	Luminosity (fb^{-1})
/SingleElectron/Run2015D-16Dec2015-v1/MINIAOD	2.3
/SingleMuon/Run2015D-16Dec2015-v1/MINIAOD	2.3

Table 5.1: Data samples.

Background sample	Cross section (pb)
$TT\_TuneCUETP8M1\_13TeV - powheg - pythia8$	831.76
$ST\_tW\_top\_5f\_inclusiveDecays\_13TeV - powheg - pythia8\_TuneCUETP8M1$	35.6
$ST\_tW\_antitop\_5f\_inclusiveDecays\_13TeV - powheg - pythia8\_TuneCUETP8M1$	35.6
$DYJetsToLL\_M - 50\_TuneCUETP8M1\_13TeV - madgraphMLM - pythia8$	6025.2
$DYJetsToLL\_M - 50\_HT - 100to200TuneCUETP8M1\_13TeV - madgraphMLM - pythia8$	147.40*1.23
$DYJetsToLL\_M - 50\_HT - 200to400TuneCUETP8M1\_13TeV - madgraphMLM - pythia8$	40.99*1.23
$DYJetsToLL\_M - 50\_HT - 400to600TuneCUETP8M1\_13TeV - madgraphMLM - pythia8$	5.678*1.23
$DYJetsToLL\_M - 50\_HT - 600toInfTuneCUETP8M1\_13TeV - madgraphMLM - pythia8$	2.198*1.23
$WJetsToLNu\_TuneCUETP8M1\_13TeV - madgraphMLM - pythia8$	61526.7
$WJetsToLNu\_HT - 100To200TuneCUETP8M1\_13TeV - madgraphMLM - pythia8$	1345*1.21
$WJetsToLNu\_HT - 200To400TuneCUETP8M1\_13TeV - madgraphMLM - pythia8$	359.7*1.21
$WJetsToLNu\_HT - 400To600TuneCUETP8M1\_13TeV - madgraphMLM - pythia8$	48.91*1.21
$WJetsToLNu\_HT - 600To800TuneCUETP8M1\_13TeV - madgraphMLM - pythia8$	12.05*1.21
$WJetsToLNu\_HT - 800To1200TuneCUETP8M1\_13TeV - madgraphMLM - pythia8$	5.501*1.21
$WJetsToLNu\_HT - 1200To2500TuneCUETP8M1\_13TeV - madgraphMLM - pythia8$	1.329*1.21
$WJetsToLNu\_HT - 2500ToInfTuneCUETP8M1\_13TeV - madgraphMLM - pythia8$	0.03216*1.21
$WW\_TuneCUETP8M1\_13TeV - pythia8$	118.70838
$WZ\_TuneCUETP8M1\_13TeV - pythia8$	47.13
$ZZ\_TuneCUETP8M1\_13TeV - pythia8$	16.523

Table 5.2: Background MC samples.

Signal sample	Cross section (pb)
$ExtendedWeakIsospinModel\_\ell\ell jj\_L5000\_M500\_CalcHEP$	331.7e-03
$ExtendedWeakIsospinModel\_\ell\ell jj\_L5000\_M1500\_CalcHEP$	114.4e-03
$ExtendedWeakIsospinModel\_\ell\ell jj\_L5000\_M2500\_CalcHEP$	22.36e-03
$ExtendedWeakIsospinModel\_\ell\ell jj\_L5000\_M3500\_CalcHEP$	5.029e-03
$ExtendedWeakIsospinModel\_\ell\ell jj\_L5000\_M4500\_CalcHEP$	1.282e-03

Table 5.3: Signal MC samples.

5.2 Object selection

A selection of the objects in the final state (muons, electrons and jet) has been estabilished, in agreement with the POG (Physics Object Group) dedicated groups, in order to assure the highest efficiency and the lowest possible fake rate, in the object reconstruction and identification.

5.2.1 Muons

In the $\mu\mu jj$ channel we use the trigger HLT_Mu50, which is applied also to the MC samples. The muons are taken from the collection "slimmedMuons", and are identified according to the "High-pT" working point and the "Loose" tracker isolation selection [21], recommended by the Muon POG and described in the following. The minimum p_T of the leading muon has to be 53 GeV, whilst that of the subleading is 30 GeV. The muon candidates are required to be within $|\eta| < 2.4$. We use the data/MC scale factors according to the indications reported in [26].
In the $eejj$ channel we rely on the "Loose" working point [21] and Loose tracker isolation to veto the presence of muons in the selected events. In this case muons are required to have $p_T > 20$ GeV and $|\eta| < 2.4$.

The four quality selections for muons, in order of increasing purity are: "Loose", "Soft", "Tight" and "High-pT". Among them, we choose the "High-pT" selection for the signal muons, because we deal with an high mass resonance decaying in high p_T particles. This selection consists in the following requests.

- IsGlobalMuon; a muon is called global when it has been reconstructed with both tracker and muon chambers sub-detectors.

- Number of valid hits> 0; at least one muon chamber hit included in the global-muon track fit, to suppress hadronic punch-through and muons from decays in flight.

- Number of matched stations> 1; muon segments in at least two muon stations, to suppress punch-through and accidental track-to-segment matches.

- $|d_{xy}| < 0,2$ cm; this upper limit in the transverse impact parameter of the muon track, referred to the primary vertex, suppresses cosmic muons and muons from decays in flight.

- $|d_z| < 0,5$ cm; this upper limit in the longitudinal parameter of the muon track, referred to the primary vertex, further suppresses cosmic muons, muons from decays in flight and tracks from PU.

- Number of valid inner hits> 0; at least one pixel hit in the track of the global muon, to further suppress muons from decays in flight.

- Number of tracker layers> 5; at least 5 layers are passed trough the tracker, to guarantee a good p_T measurement and to suppress muons from decays in flight.

- $\Delta p_T / p_T < 0,3$; this limit on the relative error on p_T suppresses grossly misreconstructed muons.

The "High-pT" selection is complemented with the requirement of an isolation criterion for both muons in the final state. The choosen criterion is $TrackerIso$ at the Loose working point. This means that the variable, where ΔR is taken respect with the muon candidate,

$$TrackerIso = \sum p_T(track\ within\ \Delta R < 0.3)/p_T(\mu), \tag{5.2}$$

is requested to be $TrackerIso < 0.10$.

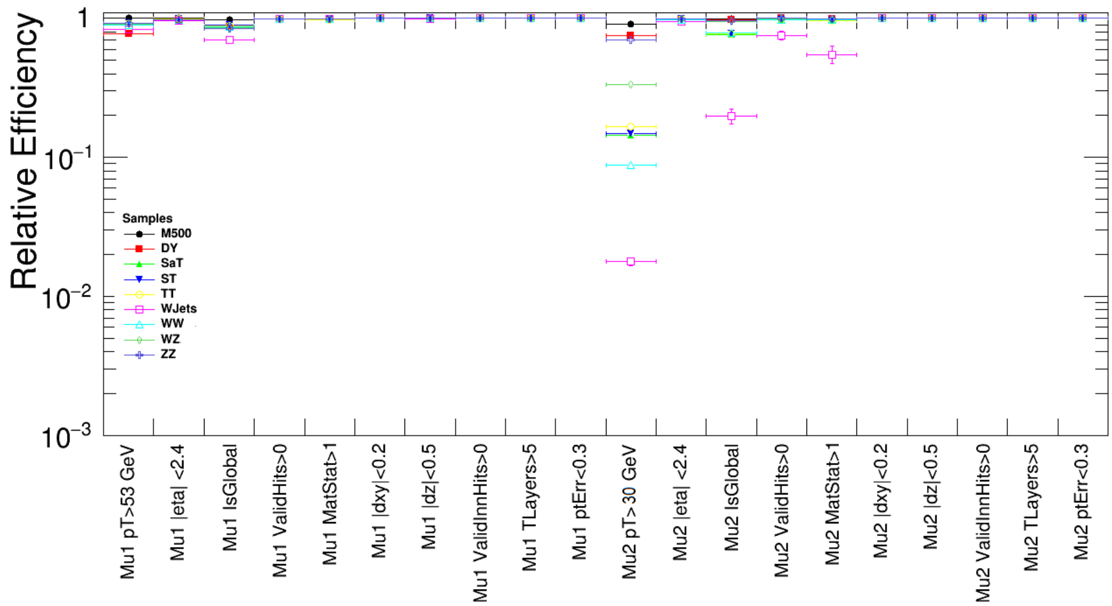

Figure 5.1: Relative efficiency of each request of the "High-pT" selection, sequentially applied to the leading muon, Mu1, and to the subleading muon, Mu2, "M500" is the signal sample featuring $\Lambda = 5$ TeV and $M(N) = 500$ GeV.

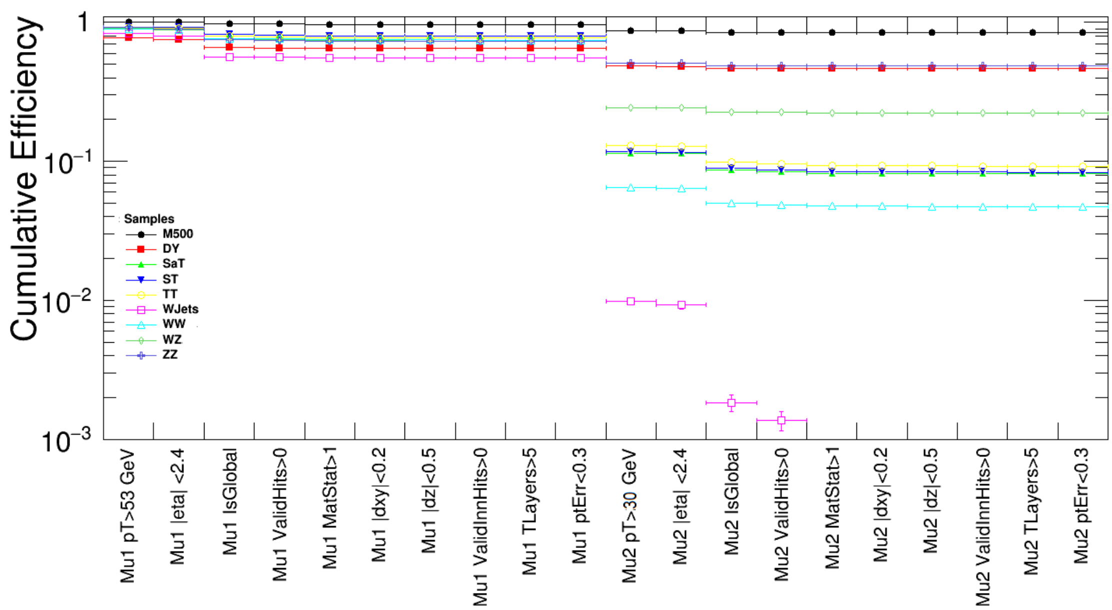

Figure 5.2: Cumulative efficiency of each request of the "High-pT" selection, sequentially applied to the leading muon, Mu1, and to the subleading muon, Mu2, "M500" is the signal sample featuring $\Lambda = 5$ TeV and $M(N) = 500$ GeV.

5.2.2 Electrons

In the eejj channel we use the trigger $HLT\_Ele105\_CaloIdVT\_GsfTrkIdT$, which is applied also to the MC samples. The electrons are taken from the collection "slimmedElectrons", and are identified according to the "HEEP" selection [22], described in the following.
The minimum p_T of the leading electron has to be 110 GeV, whilst that of the subleading one 35 GeV. The electron candidates are required to be within $|\eta| < 2.4$. We use the data/MC scale factors according to the measurement reported in [25].
In the $\mu\mu jj$ channel we use the "Veto" working point described in [23] to veto the presence of electrons in the selected events. In this case electrons are required to have $p_T > 20$ GeV and $|\eta| < 2.4$.

The "HEEP" selection for the electrons contains the following requests.

- $E_T > 35$ GeV, where E_T is the corrected supercluster transverse energy.
- $|\eta_{sc}| < 1.4442$ for a barrel electron and $1.566 < |\eta_{sc}| < 2.5$ for an endcap electron, where η_{sc} is the super cluster pseudorapidity.
- isEcalDriven=1; electrons can be ecal driven (found using egamma techniques) or tracker driven (found using particle flow). Currently, while useful for low energy non isolated electrons, particle flow is not useful or validated for high energy electrons. Hence, we require the electrons to be ecal driven.
- $\Delta\eta_{in}^{seed} < 0.004$ for a barrel electron and $\Delta\eta_{in}^{seed} < 0.006$ for an endcap electron. This is the difference in η of the track, as measured in the inner layer, extrapolated to the interaction vertex and then extrapolated to the calorimeter, and the η of the supercluster. Instead of the supercluster pseudorapidity, it uses the one of the seed of the supercluster, which is a more accurate indication of the η of the original electron before bremsstrahlung.
- $\Delta\phi_{in} < 0.06$; the difference in ϕ between the track position as measured in the inner layer, extrapolated to the interaction vertex and then extrapolated to the calorimeter, and the ϕ of the supercluster.
- H/E <2/E + 0.05 for a barrel electron and H/E < 12.5/E + 0.05 for an endcap electron, where H/E is the ratio of the hadronic energy of the CaloTowers,

in a cone of radius 0.15 centred on the electron's position, in the calorimeter, over the electromagnetic energy of the electron's supercluster.

- Full 5×5 $\sigma_{i\eta i\eta} < 0.03$ for the endcap electrons; a condition on the spread in eta in units of crystals of the electron's energy in the 5x5 block centred on the seed crystal.
- Conditions on the shape of the energy deposition in the ECAL calorimeter cristals.
- An isolation request based on the energy deposition in the calorimeter.
- A tracker isolation criterion, based on the p_T sum of the tracks in a ΔR cone of 0.3 around the electron.
- Inner Layer Lost Hits < 2.
- $d_{xy} < 0.02$ and $d_{xy} < 0.05$, respectively for a barrel and endcap electron.

5.2.3 Jets

Jets are collections of particles, originating from a common parton, as a result of the hadronization process. They are emitted within a relative small cone, the higher is the momentum magnitude of the original parton, the smaller is the cone amplitude.
The aim of the jet clustering algorithms (JCAs) is to properly identify, and cluster the final state particle of the same jet, ignoring potential fakes.
Two main difficulties arise in identifying jets. The first, known as collinearity, arises when two close particles are not resolved; the JCA interprets them as one single energetic particle, which leads to an incorrect jet seed. The second problem, infrared sensitivity, involves soft radiation between two seeds from different jets; the JCA produces a single merged jet.

Two collections of jets are considered in this analysis: "slimmedJets" and "slimmedJetsAK8". The first one was used only when optimising the definition of the signal region, whilst the second one is actually used in the main analysis. In both cases, the jets that we consider are identified according to the recommended "Tight" working point, in [24], whose cuts are briefly described below.
For $|\eta| < 3$;

- Neutral hadronic energy fraction $< 0,9$,
- Neutral electromagnetic energy fraction $< 0,9$,
- Number of constituents > 1,
- Charged hadronic energy fraction > 0,
- Charged multiplicity > 0,
- Charged electromagnetic energy fraction $< 0,99$.

For $|\eta| \geq 3$;

- Neutral electromagnetic energy fraction $< 0,9$,
- Number of neutral particles > 10.

The kinematic and geometric acceptance cuts are;

- $p_T > 30$ GeV ($p_T > 190$) for slimmedJets (slimmedJetsAK8),
- $|\eta| < 2,4$ GeV for both.

We further perform a cleaning against electrons and muons for slimmedJets ($\Delta R > 0.4$) and slimmedJetsAK8 ($\Delta R > 0.8$).The jet candidates are corrected according to the most updated JER reported in [27]. In the following we will call "jet" any of the slimmeJets, and "fat jet" any of the slimmedJetsAK8 satisfying the requirements described in this section.

During the optimisation of the signal selection, we have considered the possibility to use the b-jet tagging information, relying on the pfCombinedInclusiveSecondaryVertexV2BJetTags discriminator and the "Loose", "Medium" or "Tight" working points indicated in [28].

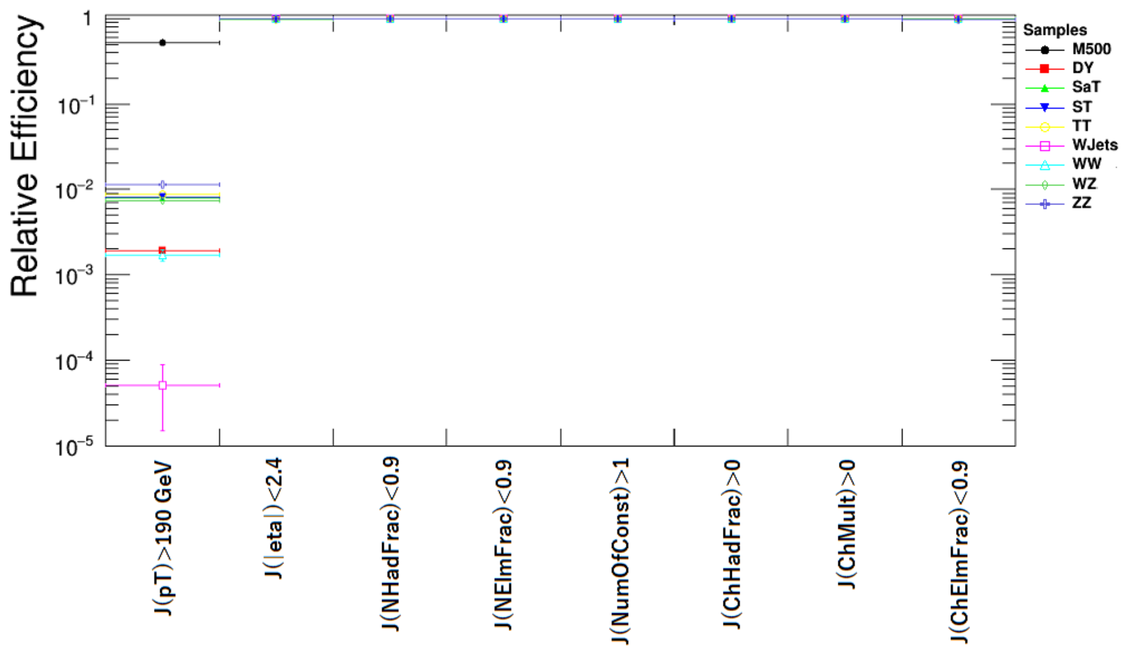

Figure 5.3: Relative efficiency of each request of the "Tight" selection, applied to the leading fat jet, "M500" is the signal sample featuring $\Lambda = 5$ TeV and $M(N) = 500$ GeV.

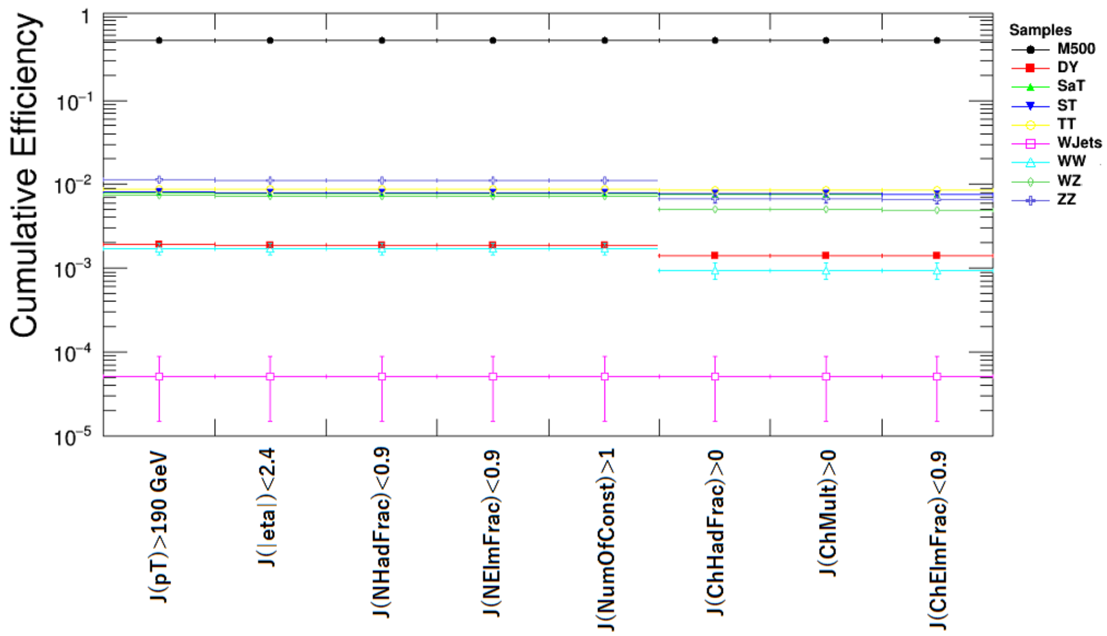

Figure 5.4: Cumulative efficiency of each request of the "Tight" selection, applied to the leading fat jet, "M500" is the signal sample featuring $\Lambda = 5$ TeV and $M(N) = 500$ GeV.

5.3 Trigger selection

A systematic study, here shown for the $\mu\mu jj$ channel, has been taken on about the performances of eight high level trigger (HLT) paths on our signal samples.

The total trigger efficiency is reported in Table 5.4, setting $\Lambda = 5$ TeV and for three values of mass; 500, 1500 and 2500 GeV. To measure these efficiency, we select first only the events that contain gen-level muons overcoming a p_T threshold 5 GeV greater then the trigger threshold. Secondly, we apply the trigger to these preselected events. The ratio of the number of events after trigger over the number of preselected events is the total trigger efficiency.

The plots of the trigger efficiency, as a function of the observables p_T, η, and the number of vertices, are shown in Fig. 5.5,5.6,5.7, setting $\Lambda = 5$ TeV and for a mass of 500 GeV, the results are analogous for the other mass values.
The final choice is in favour of the high level trigger path HLT_Mu50, which gives the highest performances in terms of efficiency and stability, and has already been implemented and further tested in previous analyses.

Trigger path	M(N)=500 GeV	M(N)=1500 GeV	M(N)=2500 GeV
$HLT\_Mu17\_TkrIsoVVL\_Mu8\_TkrIsoVVL\_DZ$	89.2 ± 0.3	87.5 ± 0.4	86.8 ± 0.3
$HLT\_Mu17\_TkrIsoVVL\_TkMu8\_TkrIsoVVL\_DZ$	94.7 ± 0.2	94.5 ± 0.5	94.1 ± 0.2
$HLT\_IsoMu20$	98.4 ± 0.1	98.6 ± 0.5	97.7 ± 0.1
HLT_Mu45_eta2p1	99.4 ± 0.1	99.9 ± 0.3	99.2 ± 0.1
HLT_Mu50	99.3 ± 0.1	99.9 ± 0.5	99.1 ± 0.1
$HLT\_IsoMu17\_eta2p1$	98.4 ± 0.1	98.5 ± 0.5	97.7 ± 0.1
$HLT\_IsoMu24\_eta2p1$	98.3 ± 0.1	98.4 ± 0.5	97.6 ± 0.1
$HLT\_IsoTkMu20$	98.3 ± 0.1	98.3 ± 0.5	97.9 ± 0.1

Table 5.4: Trigger efficiency on the signal, setting $\Lambda = 5$ TeV and for the three values of mass 500,1 500, and 2 500 GeV.

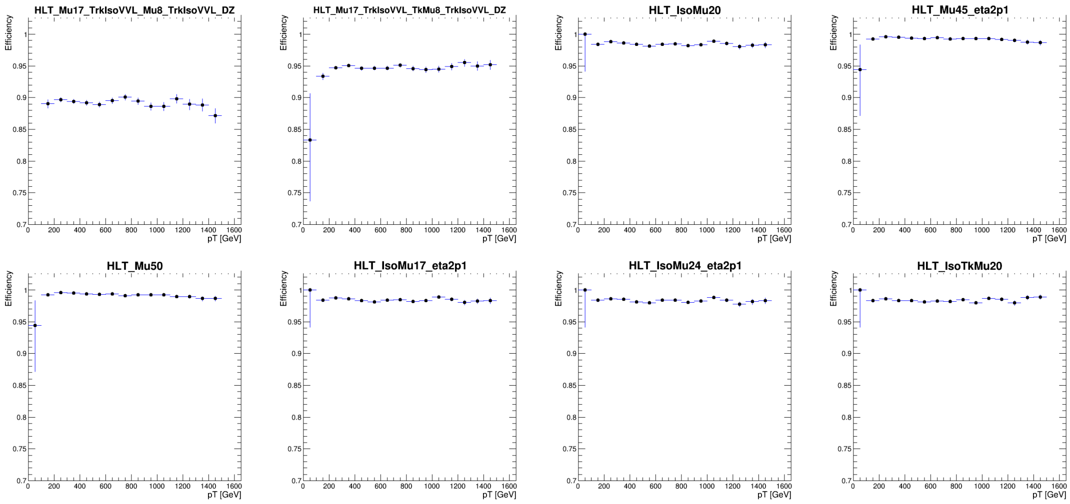

Figure 5.5: Efficiency as a function of p_T of the gen-level leading muon, plotted for each one of the eight tested trigger paths.

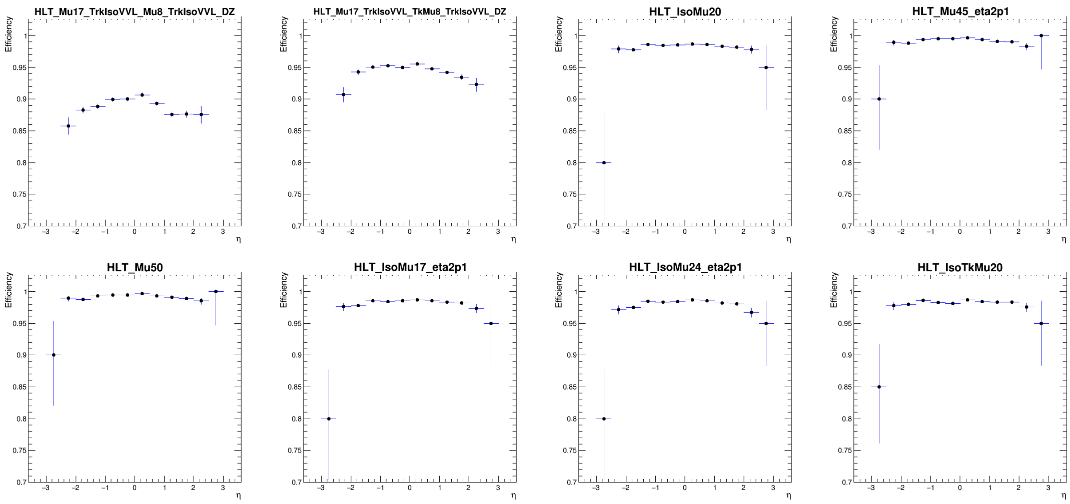

Figure 5.6: Efficiency as a function of η of the gen-level leading muon, plotted for each one of the eight tested trigger paths.

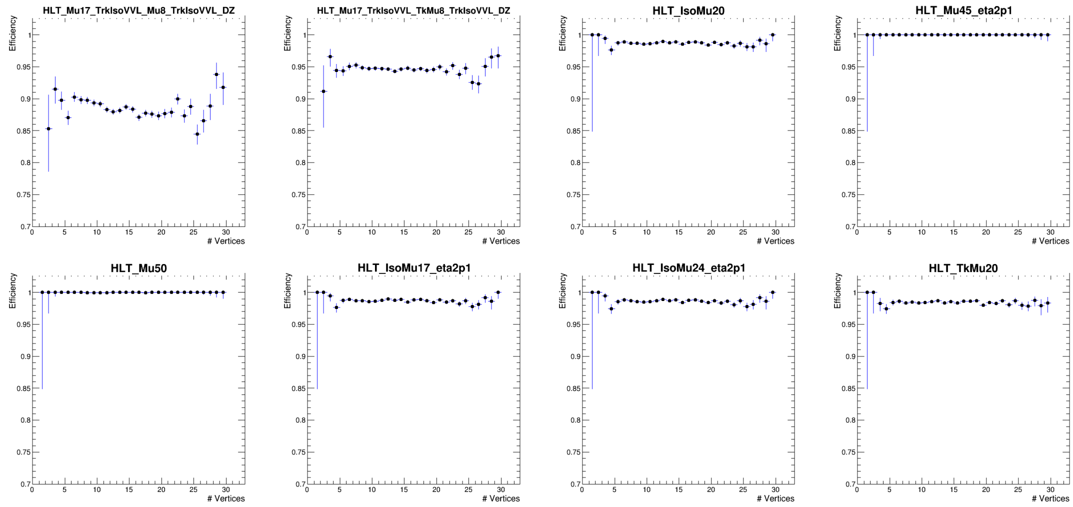

Figure 5.7: Efficiency as a function of the number of vertices plotted for each one of the eight tested trigger paths.

5.4 Signal region

The signature of this analysis is, in principle, characterised by the presence of two same flavour leptons and two jets.

Because of the topology of our signal, we expect that, in a high fraction of events, the two jets are generated close to each other, ending up in a single reconstructed fat jet. The more dominant is the gauge interaction, the more likely this eventuality is, due to the presence of a boosted W boson mediation.

Having a look at the distributions of the fat jets multiplicity Fig. 5.8, reported for the various masses at $\Lambda = 15$ TeV, we actually observe that the highest bin moves from 1 to 2 passing from 500 to 4500 GeV. The Λ value of 15 TeV has been chosen here, because it ensures to move from a clear gauge dominance at mass 500 GeV, to a clear contact dominance at mass 4 500 GeV(see the central plot in Fig. 4.2).

At low masses, the two jets tend to be merged, as expected, giving only one fat jet in the final state. On the other hand, also at higher masses, where the contact interaction dominates and the jets should not be emetted so angularly close, we have more then 90% of events with at least one fat jet. This can be justified by considering the final state radiation of these high energy jets, which enlarges their reconstruction cone.

One can also notice that in the case of mass 500 GeV the bin at zero assumes the highest value, compared to the other masses, despite the boost effect of the gauge interaction should be the most considerable. This is due to the fact that the boosting depends on the mass difference between the heavy neutrino and the W; the lower is the neutrino's mass, the less pronounced this effect is.

To summarise, the study of the fat jet multiplicity shows that, regardless of the mass value choosen, we have a probability greater then 70% to end up with at least one fat jets in the signal event. The reason for this is the jet merging, at lower masses, and the jet radiation, at higher masses.

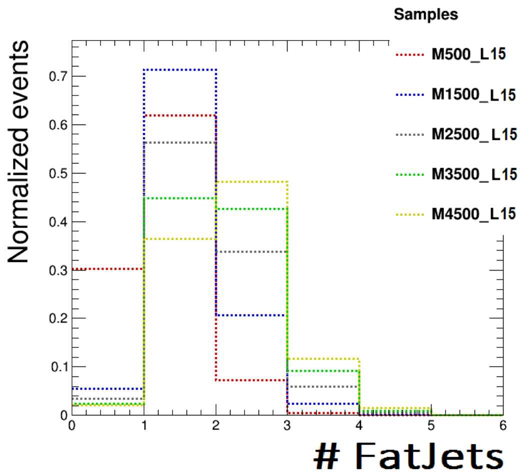

Figure 5.8: Multiplicity of fat jets, setting $\Lambda = 15$ TeV, and considering the mass values of 500, 1500, 2500, 3500 and 4500 GeV

In order to understand which jet request is the most suitable for the analysis, we have compared two cases in which we selected; two leptons and two jets (reconstructed with a jet radius of R = 0.4) or two leptons and at least one fat jet (with a jet radius of R = 0.8). We also add a request on b-tag jets, that could be useful to reduce the $T\bar{T}$ background (Fig. 5.10, 5.11).
This optimisation study has been performed restricting the selection to the high-mass region given by $M(\ell, \ell) > 300$ GeV, where we expect our signal to compete against the background, as you can observe in Fig. 5.9.
We have found that the selection with two leptons and at least one fat jet has the highest significance, defined as $S = \frac{s}{\sqrt{s+b}}$, where s is the expected number of signal events and b of background events, from MC samples normalised to 2.3 fb^{-1}.

The condition on the b-tag jets is irrelevant, infact the significance grows increasing the number of b-tag jets up to 2, that means not reducing signifianctly the $t\bar{t}$ background.
This conclusion has been demonstrated to be valid for any mass hypothesis considered.

The signal region is finally defined asking two leptons and at least one fat jet, which satisfy the already mentioned requirements, plus $M(\ell, \ell) > 300$ GeV. For the sake of simplicity, despite the variable number of jet in the final state of signal events, we will keep on denoting $eejj$ and $\mu\mu jj$ the signal signature, respectively for the electron and muon channel.

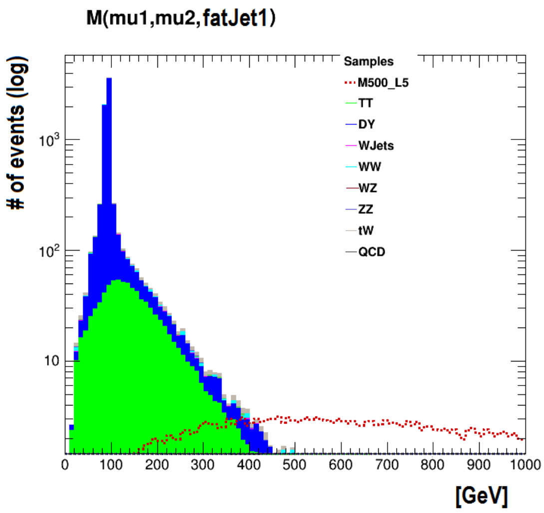

Figure 5.9: Distribution of the invariant mass $M(\mu_1, \mu_2)$ for backgrounds (stackplot) with overlaid signal featuring M=500 GeV and $\Lambda = 5$ TeV (red dotted line) in logarithmic scale.

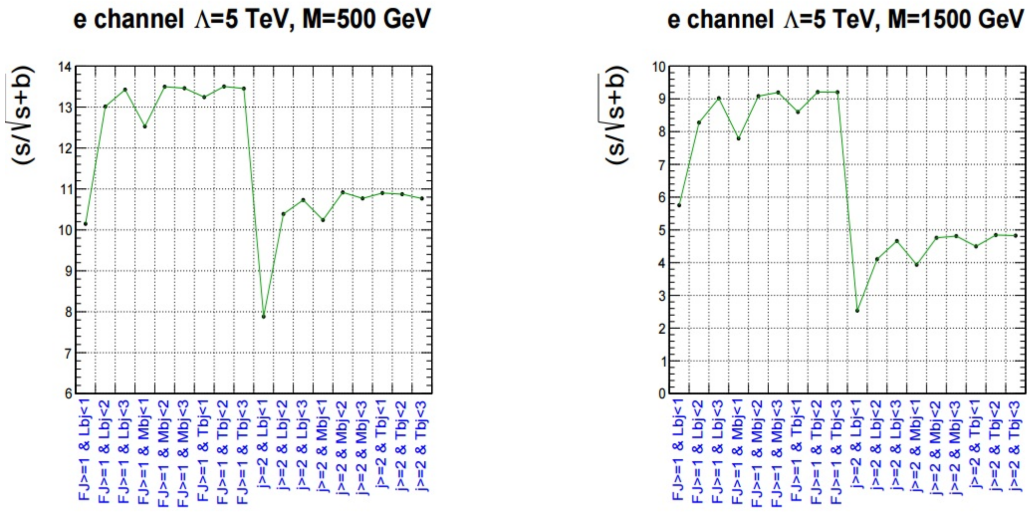

Figure 5.10: Significance plot for the various jet requests, for the $eejj$ channel, at Λ=5 TeV and for a neutrino's mass of 500 GeV (left) or 1500 GeV (right). The labels stay for; FJ=fat jets, j=jets, Lbj=loose b-tag jets, Mbj=medium b-tag jets, Tbj=tight b-tag jets.

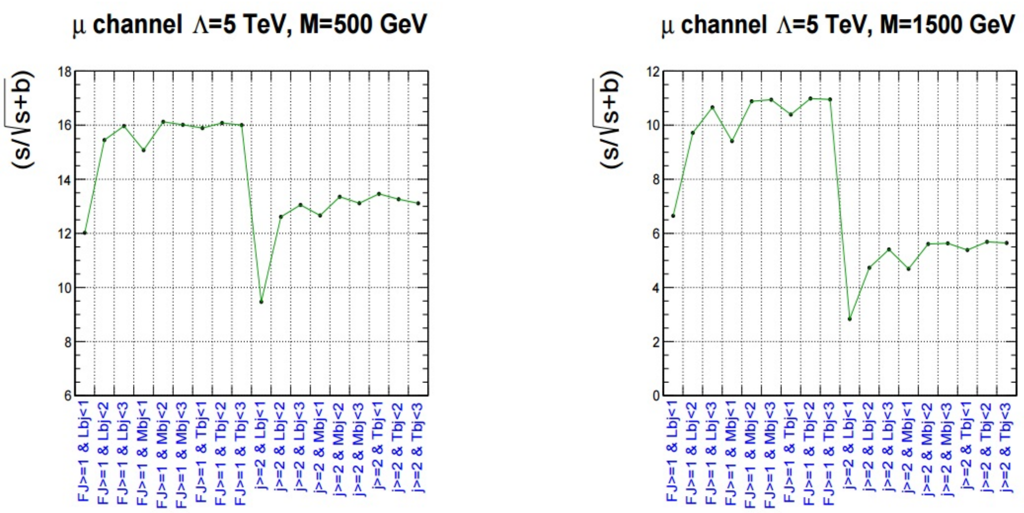

Figure 5.11: Significance plot for the various jet requests, for the $\mu\mu jj$ channel, at Λ= 5 TeV and for a neutrino's mass of 500 GeV (left) or 1500 GeV (right). The labels stay for; FJ=fat jets, j=jets, Lbj=loose b-tag jets, Mbj=medium b-tag jets, Tbj=tight b-tag jets.

5.4.1 eejj channel

The signal region (SR) for the $eejj$ channel is defined by;

- $HLT\_Ele105\_CaloIdVT\_GsfTrkIdT$,
- 2 electrons, with $p_T(e_1) > 110$ GeV and $p_T(e_2) > 35$ GeV and $|\eta| < 2.4$,
- at least 1 fat jet, with $p_T > 190$ GeV and $|\eta| < 2.4$,
- $M(e_1, e_2) > 300$ GeV.

e_1 and e_2 indicate the leading and subleading electron, respectively.

5.4.2 $\mu\mu jj$ channel

The signal region (SR) for the $\mu\mu jj$ channel is defined by;

- HLT_Mu50,
- 2 muons, with $p_T(\mu_1) > 53$ GeV and $p_T(\mu_2) > 30$ GeV and $|\eta| < 2.4$,
- at least 1 fat jet, with $p_T > 190$ GeV and $|\eta| < 2.4$,
- $M(\mu_1, \mu_2) > 300$ GeV.

μ_1 and μ_2 indicate the leading and subleading electron, respectively.
The results of the signal region selection in the $\mu\mu jj$ channel, in terms of cumulative efficiency for each request, are reported in Table 5.5 and 5.6, for signal and backgrounds, respectively.

Selection	$M500\_L5$ (%)	$M1500\_L5$ (%)	$M2500\_L5$ (%)
HLT_Mu50	89.5±0.1	94.78±0.07	95.61±0.07
# of HighPt mu==2	79.3±0.1	82.1±0.1	80.8±0.1
# BoostedJet> 0	55.3±0.2	77.5±0.1	78.0±0.1
M(mu1,mu2)> 300 GeV	49.3±0.2	75.2±0.1	76.8±0.1

Table 5.5: Cumulative efficiency of each request of the signal region selection, on signal samples, at $\Lambda = 5$ TeV and for the three values of mass 500, 1500 and 2500 GeV.

Selection	TT	DY	WJets	WW	WZ	ZZ	ST /SaT
HLT_Mu50	3.849±0.002	4.182±0.007	0.168±0.001	1.03±0.01	1.97±0.01	3.10±0.02	3.52±0.02
# of HighPt mu==2	0.369±0.001	1.808±0.004	0±0	0.207±0.005	0.716±0.009	1.36±0.01	0.421±0.007
# BoostedJet> 0	0.056±0.001	0.057±0.001	0±0	0.010±0.001	0.071±0.003	0.124±0.004	0.050±0.002
M(mu1,mu2)> 300 GeV	0.004±0.001	0.0010±0.0001	0±0	0.0010±0.0001	0.0010±0.0001	0.0020±0.0001	0.007±0.001

Table 5.6: Cumulative efficiency of each request of the signal region selection, on background samples.

5.5 Variable for the signal extraction

We want to perform a shape analysis, the variable we use for extracting the signal is $M(\ell, \ell, J)$, the invariant mass of the two leptons and the leading fat jet. The main reason for choosing this variable is that this has been used in the previous analysis during Run I, see [7], and we would like to obtain comparable results.
Secondly, we have found out in 4.2 that the reconstruction of the neutrino's invariant mass, which would require the tagging of the muons origin, is not a feasible alternative.

In Fig.5.12 we plot the distribution of $M(\ell, \ell, J)$ in the SR, and report the number of events of signal and of background expected from simulation. The considered backgrounds are DY, $t\bar{t}$, tW, $WJets$, WW, WZ, ZZ, QCD.
From the plot in Fig. 5.12 we can see that $DY, t\bar{t}$ and tW are the most relevant, while the other backgrounds are expected to contribute less, and will be referred all together as "Other". The plots also show that the observable $M(\ell, \ell, J)$ can effectively separate the signal from the background.

5.6 Background estimation

In this section we describe the estimation of the backgrounds. We use semi-data-driven techniques for DY, $t\bar{t}$ and tW. We evaluate the QCD contribution with a complete data-driven method.

5.6.1 DY

The DY contribution to the signal region (SR) is estimated normalizing the MC simulation to the data in a control region (CR), defined with the same cuts of the signal region selection, but using as observable the dilepton invariant mass, taken

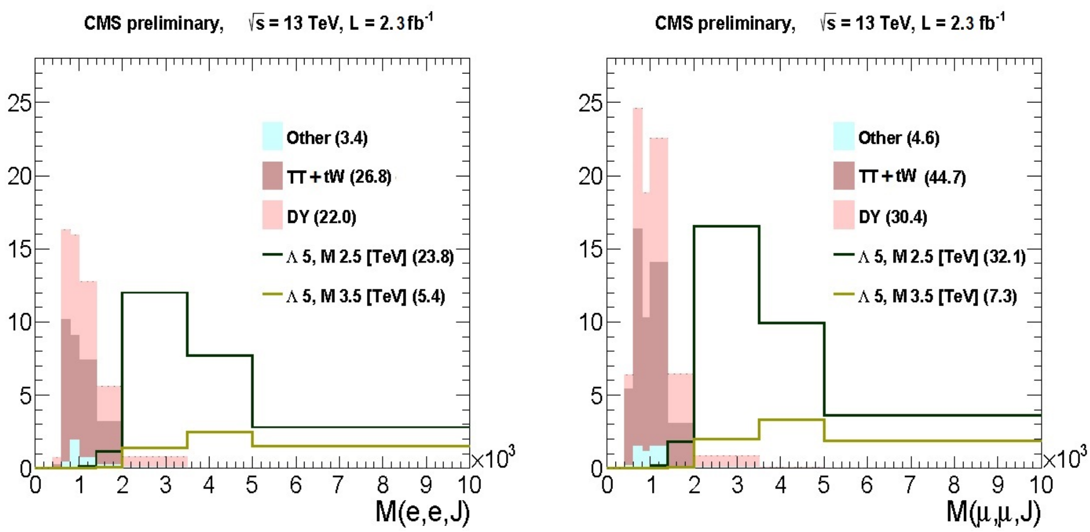

Figure 5.12: Invariant mass of the system eeJ (left) and $\mu\mu J$ (right) in the signal region, for background (stackplot) and overlaid signal (green lines).

around the Z peak, $80 < M(\ell, \ell) < 100$ GeV (Fig. 5.13). A scale factor (SF) is evaluated in this control region as

$$SF = \frac{N_{DY}^{data}}{N_{DY}^{MC}},$$

where N_{DY}^{data} is the number of only DY data, after substracting the MC minority contribution of the other backgrounds, $N_{DY}^{data} = N^{data} - N_{notDY}^{MC}$. The scale factor for $eejj$ channel is 1.08 ± 0.02, while for $\mu\mu jj$ it is 1.16 ± 0.02.

This SF is assumed to be the same in the signal region of our analysis. In order to check the validity of this assumption, we have extended the region of mass up to 300 GeV, to remain out from the signal region, and we have evaluated the same ratio. We have found a constant value comparable with the one taken between 80 and 100 GeV, the 2% difference is used to quote a systematic uncertainty.

5.6.2 $t\bar{t}$ and tW

For the estimation of the $t\bar{t}$ and tW backgrounds, first we take the shape of $t\bar{t}$ plus tW in an $e\mu$ control region (CR) from data, subtracting the other backgrounds. Then, we use the $t\bar{t}$ and tW MC samples to estimate the ratio of events of the signal region over the control region, $R_{SR/CR}$.

This $e\mu$ control region is defined exactly as the signal region, but substituting the

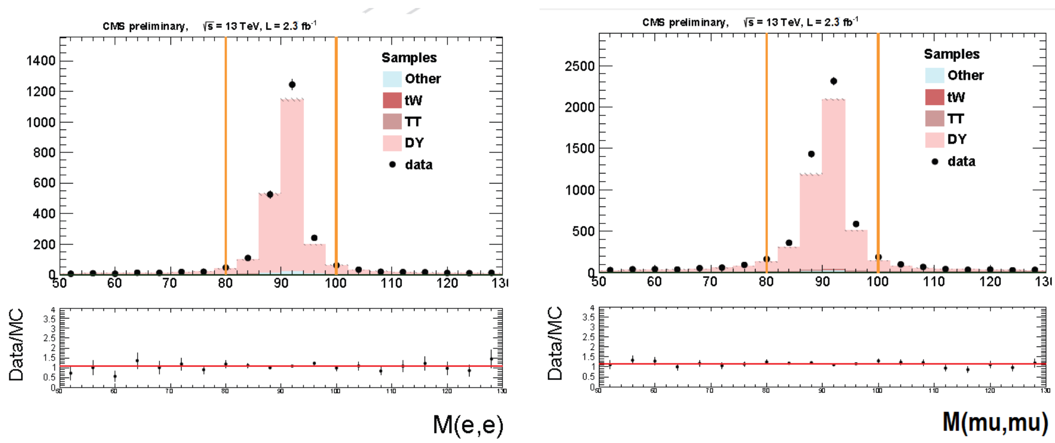

Figure 5.13: $M(\ell,\ell)$ distribution for data (black dots) and backgrounds (stack plot) around the Z mass peak, for electron (left) and muon channel (right), the bottom plot reports the Data/MC ratio bin by bin.

subleading lepton with a lepton of the other flavor. This will be a High-pt muon, selected with loose tracker isolation and the same kinematic requirements of the subleading electron, in the eejj channel, and a HEEPv6.0 electron, with the same kinematic requirements of the subleading muon, in the $\mu\mu jj$ channel.
Finally we estimate the $t\bar{t}$ plus tW contribution to the signal region as

$$N^{SR}_{t\bar{t}+tW} = (N^{CR}_{data} - N^{CR}_{Not\ t\bar{t},tW\ \ MC}) \times R_{SR/CR}.$$

Since we perform a shape analysis, the previous formula has to be read considering it for all the bins of the $M(\ell,\ell,J)$ distribution. In particular both the variables $N^{CR}_{data} - N^{CR}_{Non\ t\bar{t},tW\ \ MC}$ and $R_{SR/CR}$ are bin dependent.

In order to validate this method we need to check the following two points.

- The consistency of the shape of $M(\ell,\ell,J)$ distribution between the signal and the control region for the $t\bar{t}$ and the tW processes, using the MC samples. This is proved by the plots in Fig. 5.14 and 5.15, where the two distributions, normalized to 1 are overlapped, both the $eejj$ and $\mu\mu jj$ are presented.

- The $e\mu jj$ or μejj control region has a high purity in $t\bar{t}$, and tW and the MC simulation is well modelled for these processes. These two facts are shown to be valid by the plots in Fig. 5.16, for $eejj$ and for $\mu\mu jj$ channel.

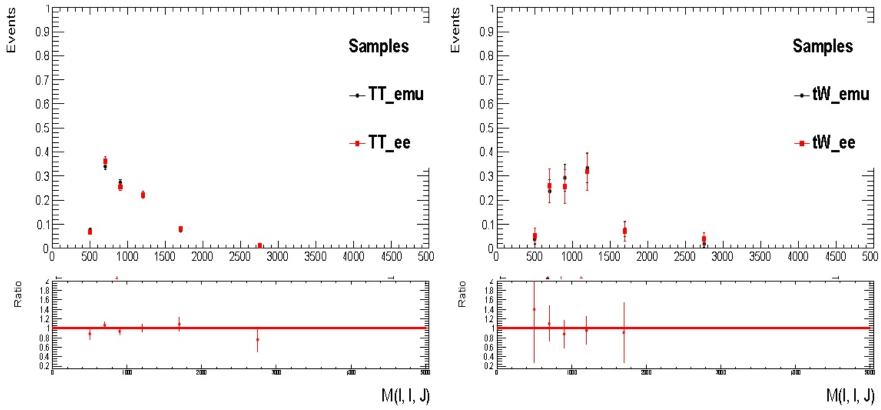

Figure 5.14: Distributions of $M(e, e, J)$ and $M(e, \mu, J)$ for the MC backgrounds $t\bar{t}$ (left) and tW (right), respectively in the signal region (red dots) and in the control region (black dots). The distributions are normalized to 1 for shape comparison.

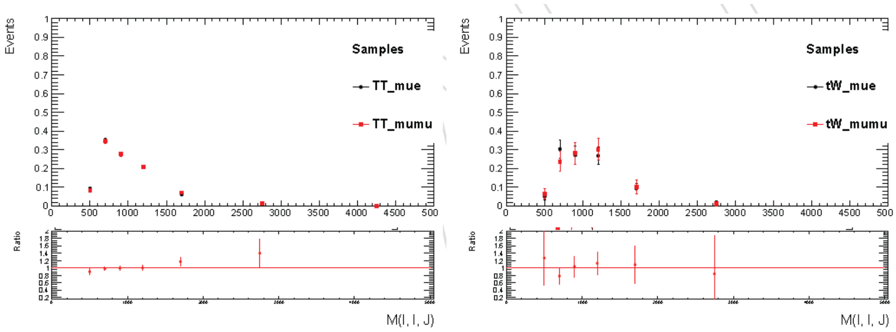

Figure 5.15: Distributions of $M(\mu, \mu, J)$ and $M(\mu, e, J)$ for the MC backgrounds $t\bar{t}$ (left) and tW (right), respectively in the signal region (red dots) and in the control region (black dots). The distributions are normalized to 1 for shape comparison.

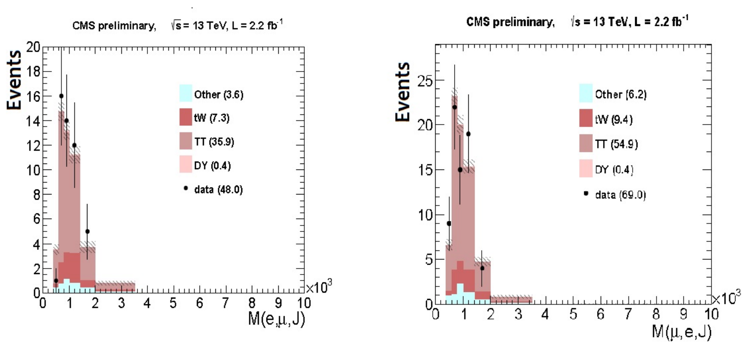

Figure 5.16: Stack plot of the backgrounds with overlaid data for the distribution $M(e, \mu, J)$ for the eejj channel (left) and $M(\mu, e, J)$ for the $\mu\mu jj$ channel (right), in the control region.

Finally, we need to estract the bin per bin ratio $R_{SR/CR}$, using the MC samples. The distribution of $M(\ell\ell J)$ and the resulting ratio are reported in Fig.5.17. The explicit values of the ratios are also illustrated in the Table 5.7.

The final estimation of $t\bar{t}$ and tW backgrounds is shown in Fig. 5.18, where we also overlap, for comparison, the nominal MC expectation of the $t\bar{t}$ and tW processes in the SR. The agreement between the data-driven estimation and the MC expectation is found to be good.

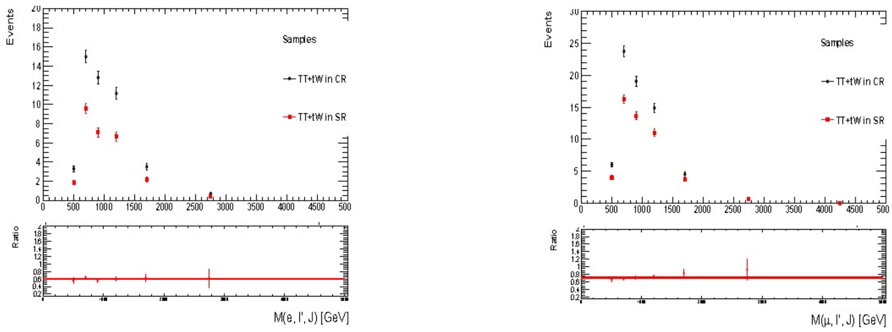

Figure 5.17: Distributions of $M(e, e, J)$ and $M(e, \mu, J)$ for the MC backgrounds $t\bar{t}$ + tW (right), respectively in the signal region (red dots) and in the control region (black dots), for e-channel (left) and μ-channel (right). The distribution are normalised to the integrated luminosity. The bottom plot shows the ratio for each bin, between the number of events in signal and control region.

Bin	400-600	600-800	800-1000	1000-1400	1400-2000	2000-3500
$t\bar{t} + tW$ e-channel	0.56 ± 0.09	0.64 ± 0.05	0.55 ± 0.05	0.59 ± 0.06	0.63 ± 0.10	0.62 ± 0.24
$t\bar{t} + tW$ μ-channel	0.67 ± 0.07	0.69 ± 0.04	0.72 ± 0.04	0.74 ± 0.05	0.83 ± 0.10	0.92 ± 0.28

Table 5.7: Ratio, bin by bin, between the number of events in the SR and in the CR, for the $t\bar{t} + tW$ MC samples.

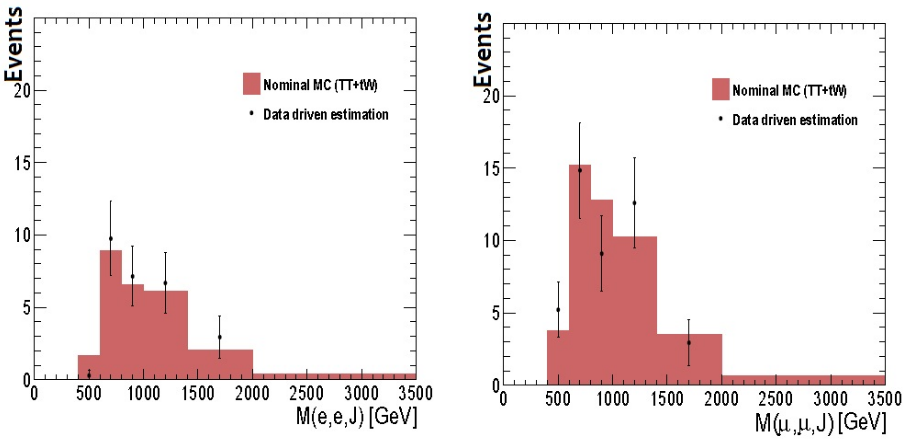

Figure 5.18: $M(e, e, J)$ in $eejj$ channel and $M(\mu\mu jj)$ in $\mu\mu jj$ channel, the data-driven estimation for $t\bar{t}$ and tW (black dots) is compared to the nominal MC prediction.

5.6.3 QCD

We evaluate the QCD multijet background from poorly identified, non-isolated lepton canditates selected from data and weighted by a correction factor, which allows to extrapolate the final contribution to the signal region.
We rely on the method developed by the $Z' \to \ell\ell$ group [29]. The used formula is:

$$QCD_{SR} = QCD_{CR} \times W^{i}_{SR/CR} \times W^{j}_{SR/CR}$$

where QCD_{SR} is the multijet contribution, in terms of number of events, estimated in the signal region; QCD_{CR} is taken from the data, applying the signal region requests, but on leptons taken with a looser selection, referred below as fake-rate preselection. $W^{i,j}_{SR/CR}$ is the p_T and η-dependent weight, used to correct QCD_{CR}, in order to estimate QCD_{SR}, and i, j refer to the two lepton candidates. For $W^{i,j}_{SR/CR}$, we rely on the measurement carried on by the $Z' \to \ell\ell$ group [29].
The fake rate preselections for electrons and muons, in $\mu\mu jj$ and $eejj$ respectively, are defined in Table 5.8 and 5.9 .
The weight $W_{SR/CR}$ is defined as $W_{SR/CR} = FR(1 - FR)$ and the FR functional form, depending on the lepton kinematic variables, is reported in Table 5.10 and 5.12 for electrons and muons.

Variable	Barrel	Endcap
$\sigma_{i\eta i\eta}$	< 0.13	< 0.34
H/E	< 0.15	< 0.10
# missing hits	< 2	< 2
$\lvert d_{xy}\rvert$	< 0.02	< 0.05

Table 5.8: Fake selection for electrons, in the $eejj$ channel.

Variable	Cut value
$\lvert d_z\rvert$	< 1.0
# of tracker layer with measurement	> 5
# valid pixel hits	> 0

Table 5.9: Fake selection for muons, in the $\mu\mu jj$ channel.

η region	E_T range	functional form
Barrel	$35 \leq E_T \leq 76.1$	$0.0524 - 0.000589 \times E_T$
	$76.1 \leq E_T \leq 145.6$	$0.0124 - 6.38 \times 10^{-5} \times E_T$
	$E_T \leq 145.6$	0.00315
Endcap $\lvert\eta\rvert < 2.0$	$35 \leq E_T \leq 75.8$	$0.0953 - 0.000815 \times E_T$
	$75.8 \leq E_T \leq 186.9$	$0.0377 - 0.000558 \times E_T$
	$E_T \leq 186.9$	0.0273
Endcap $\lvert\eta\rvert > 2.0$	$35 \leq E_T \leq 88.6$	$0.0824 - 0.000492 \times E_T$
	$88.6 \leq E_T \leq 145.7$	$0.0321 + 7.52 \times 10^{-5} \times E_T$
	$E_T \leq 145.7$	0.0506

Table 5.10: Funcional form of FR for electrons, in the $eejj$ channel.

η region	p_T range	functional form
Barrel	$p_T > 50$	$2.22 \times 10^{-2} + exp(-3.16 + 2.80 \times 10^{-2} \times p_T)$
Endcap	$50 < p_T < 110$	$8.83 \times 10^{-3} + exp(5.93 - 1.33 \times 10 \times p_T)$
Endcap	$p_T > 110$	$-2.91 + exp(1.08 + 1.32 \times 10^{-4} \times p_T)$

Table 5.11: Funcional form of FR for muons, in the $\mu\mu jj$ channel.

In the electron channel, we find out that QCD_{SR} is ~ 0.3. As it is lower than the other backgrounds, we decided to neglect it.
In the muon channel, we calculate that QCD_{SR} is 1.5 ± 1.2. As it is low, but not negligible, we decided to consider it in the analysis. It will be included in the final distribution of $M(\mu, \mu, J)$, among the minor backgrounds that are labelled as "Other".

5.7 Systematic uncertainties

Systematic effects on the background estimations and the simulated MC signals have to be considered, before dealing with the interpretatiton of the results. For the uncertainty on the luminosity we consider a value of 2.7% on the normalisation of both backgrounds and MC signals [30]. For the uncertainties related to the corrections, which we apply to the MC samples, we proceed as follows;

1. We take the central value of our measurement given by the distribution $M(\ell, \ell, J)$, which contains the backgrounds estimated according to the methods described in Section 5.6.

2. For every systematic effect we repeat the whole analysis twice, considering the deviations up and down due to the systematic, and producing two distributions

accordingly; $M(\ell, \ell, J)Up$ and $M(\ell, \ell, J)Down$.

3. We perform the subtractions $|M(\ell, \ell, J)Up - M(\ell, \ell, J)|$ and $|M(\ell, \ell, J)Down - M(\ell, \ell, J)|$, and take the maximum difference in every bin. This new distribution of the maximum difference, $M(\ell, \ell, J)Sys$, shows the shape of the systematic errors.

This procedure is used for all the backgrounds and the MC signal samples, and for both $eejj$ and $\mu\mu jj$. The approach is used for the following systematic uncertainties.

- Pile-up; the pileup weights are re-calculated by varying the value 69000 mb of minBiasXsec of 5%.
- Electron scale factors; they are varied by the uncertainty measured in [31].
- Muon scale factors; they are varied by the uncertainty associated to the central value, according to the indications in [32].
- JEC (Jet Energy Corrections); they are varied by the uncertainty taken according to the prescriptions in [33].
- JER (Jet Energy Resolution); they are varied by the uncertainty taken according to the prescriptions in [34].

We further consider a systematic associated to the methods used for estimating the backgrounds. In this analysis all the backgrounds are estimated with a formula that can be generalised as; $Bkg_{SR} = Bkg_{CR} \times w$. Bkg_{SR} represents the background contribution extrapolated to the signal region, Bkg_{CR} the background in a given CR, and w a weight used to normalise Bkg_{CR} to the signal region. The systematic error, on the estimation of Bkg_{SR}, is given by

$$\delta Bkg_{SR} = \sqrt{(\delta Bkg_{CR} \times w)^2 + (Bkg_{CR} \times \delta w)^2}.$$

This formula is used for every bin of the distributions of the estimated backgrounds, in both the $eejj$ and $\mu\mu jj$ channels.
Moreover, to account for the theoretical uncertainty that may affect the $M(\ell, \ell, J)$ distribution of the Drell-Yan process, we also consider the variation on the Drell-Yan mass shape, which is estimated relying on the PDF4LHC prescription [35].

In Appendix there are all the plots for the MC signal samples and the backgrounds considered in the $eejj$ and $\mu\mu jj$ channels, for all the above listed systematic effects. The average uncertainty for each systematic effect is reported in Table 5.12.

Systematic %	Bkg ($eejj$)	Sig ($eejj$)	Bkg ($\mu\mu jj$)	Sig ($\mu\mu jj$)
Luminosity	2.7	2.7	2.7	2.7
Pile-up	4	2	4	1
Electron SFs	1	2	1 (TT+tW only)	-
Electron en. scale	5	3	-	-
Muon SFs	2 (TT+tW only)	-	6	10
Muon pT scale	-	-	6	4
JER	2	0.4	2	0.4
JES	3	1	4	1
Background	15	-	15	-
Drell-Yan theory	10	-	10	-

Table 5.12: Systematic errors for signal and background in $eejj$ and $\mu\mu jj$ channels.

5.8 Results

In this section we illustrate the results of our search.
In Fig.5.19 we show the distribution of the variable $M(\ell, \ell, J)$ for the estimated SM backgrounds (stackplots), the signal (lines), having considered the parameters $\Lambda = 5$ TeV and the masses $M(N) = 2500$ GeV and $M(N) = 3500$ GeV, and the data (black points), for the $eejj$ (top) and the $\mu\mu jj$ (bottom) channels. The error bars stand for the statistical plus systematic uncertainty. The observations are in agreement with the expectations from the SM.

Since there is no evidence of new physics decaying to two leptons and a fat jet, we set corresponding upper limits on the existence of heavy composite Majorana neutrinos. The upper limits have been evaluated using the tool "combine" and the method "Asymptotic", providing as inputs the mass shape of estimated backgrounds, the expected signal, and the data.
We further include the systematic uncertainties described in 5.7, which are treated as uncorrelated among the bins of the $M(\ell, \ell, J)$ distributions, for systematic related to the background, and as correlated for the other systematics. We put the datacards and the rootfiles used for the limit estimations in
$/afs/cern.ch/work/f/fromeo/public/HeavyNeutrino/Limit$, for the interested reader.

The results are shown in Fig.5.20 for the $eejj$ channel (a) and the $\mu\mu jj$ channel (b). The mass of the heavy composite Majorana neutrino can be excluded up to 4.35 GeV in the $eejj$, and up to 4.50 GeV in the $\mu\mu jj$ channel, for a value of Λ of 5 TeV, with good agreement between expected and observed limit.

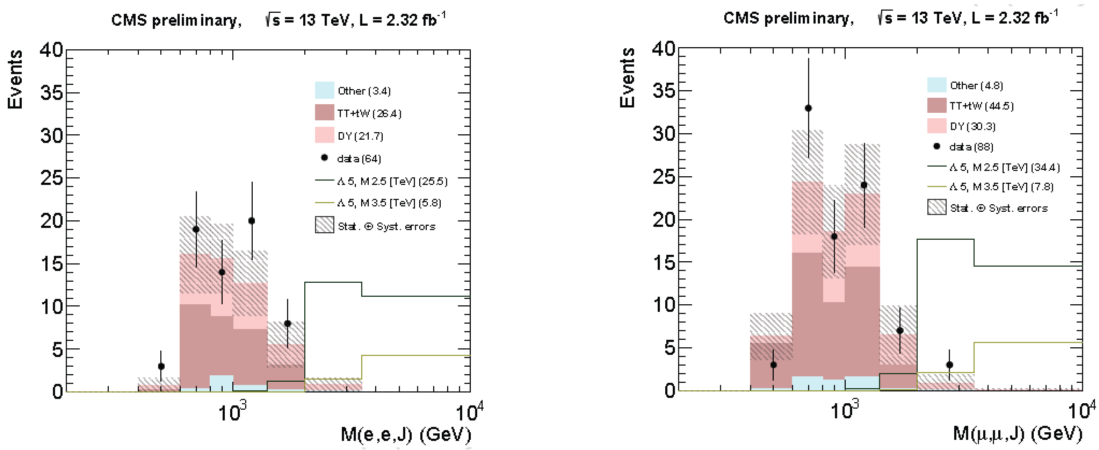

Figure 5.19: Distribution of the variable $M(\ell,\ell,J)$ for the estimated SM backgrounds (stackplots),the signal (lines) having considered the parameters $\Lambda = 5$ TeV and two masses of N equal to 2500 and 3500 GeV, and the data (black dots) for the $eejj$ (left) and the $\mu\mu jj$ (right) channels. The error bars stand for the statistical plus systematic uncertainty.

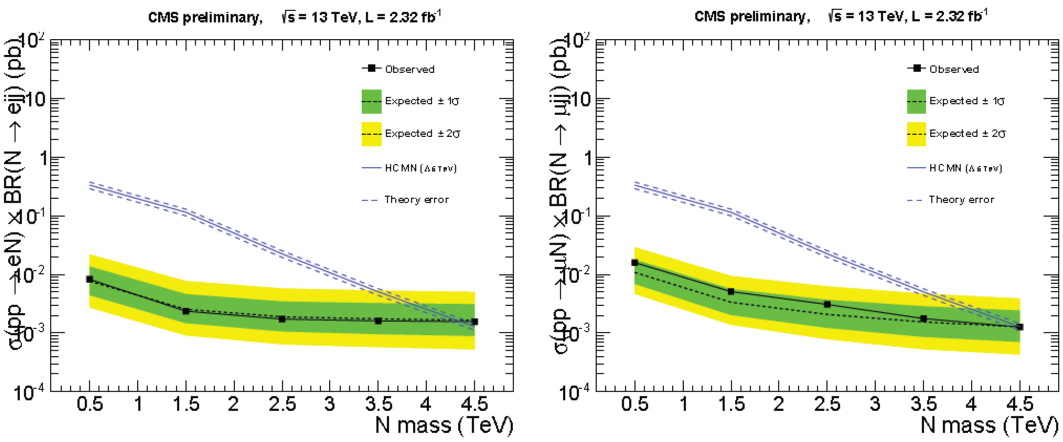

(a) (b)

Figure 5.20: The observed 95% CL upper limits (solid black lines) on $\sigma(pp \to \ell N) \times BR(N \to \ell qq)$, having analysed the $eejj$ (a) and the $\mu\mu jj$ (b) final states, as a function of the mass of the heavy composite Majorana neutrino, N. The corresponding expected limits are shown by the dotted lines, and the coloured bands represent the one (green) and two (yellow) standard deviations obtained from the background-only hypothesis. The continuous and dashed blue curve indicates the theoretical prediction in pb and its error for $\Lambda = 5$ TeV.

Chapter 6

CMS track trigger towards the HL-LHC

6.1 LHC status and future plans

The original design of the LHC was to operate at $10^{34}\ cm^{-2}s^{-1}$ of instantaneous luminosity, with 25 ns bunch spacing and approximately 25 simultaneous inelastic collisions per crossing (pile-up). After upgrades to the LHC, the luminosity and the pile-up will more than double, during the Phase 2. A serious effort will be necessary to improve the performance of the Level-1 trigger system of the CMS detector [36], [37], [38].

The current LHC plan calls for a series of long periods of data-taking, referred to as Run I, Run II, etc. interleaved with long shutdowns, indicated as LS1, LS2, LS3, etc., the whole schedule is in Fig.(6.1)
Run I is the name given to the completed data-taking period in 2011 and 2012. During the first long shutdown, LS1, which started in 2013, and ended at the beginning of 2015, some modifications were made to the LHC, to enable it to run at the center of mass energy of 13 TeV.
Run II began in 2015, and is still ongoing. The bunch spacing has been reduced to 25 ns, from 50 ns. The original performance goal for the LHC, to operate at an instantaneous luminosity of $10^{34}\ cm^{-2}s^{-1}$, with 25 ns bunch spacing, has been achieved relatively soon after the startup. Under these conditions, early in Run II, CMS experienced an average of about 25 inelastic interactions per bunch crossing, referred to as pile-up. This is the operating scenario the CMS experiment was

designed for.

A new scheme to form the bunch trains in the Proton Synchrotron (PS) will allow the luminosity to overtake the original design before the second long shutdown, LS2, planned for 2018-2019. In LS2, the injector chain will be further improved and upgraded to deliver very bright bunches. The peak luminosity shoud reach 2×10^{34} $cm^{-2}s^{-1}$ in this first phase of the LHC program, providing an integrated luminosity of over 300 fb^{-1}, by 2023. To maintain its present performance in this period, the CMS detector will undergo an upgrade program, called "CMS Phase-1 Upgrade".

By 2023, the quadrupoles that focus the beams at the ATLAS and CMS collision regions will be replaced, and crab cavities will be added to optimize the bunch overlap at the interaction region. These modifications will produce a significant increase in the LHC luminosity.

The high luminosity period that follows LS3, with the upgraded LHC, is referred to as HL-LHC or Phase 2. The proposed operating scenario is to level the instantaneous luminosity at 5×10^{34} $cm^{-2}s^{-1}$ and to deliver 250 fb^{-1} per year for a further ten years of operation. Under these conditions the event pile-up will rise substantially, to become a major challenge for the experiments and the performance degradation, due to integrated radiation dose, will need to be addressed.

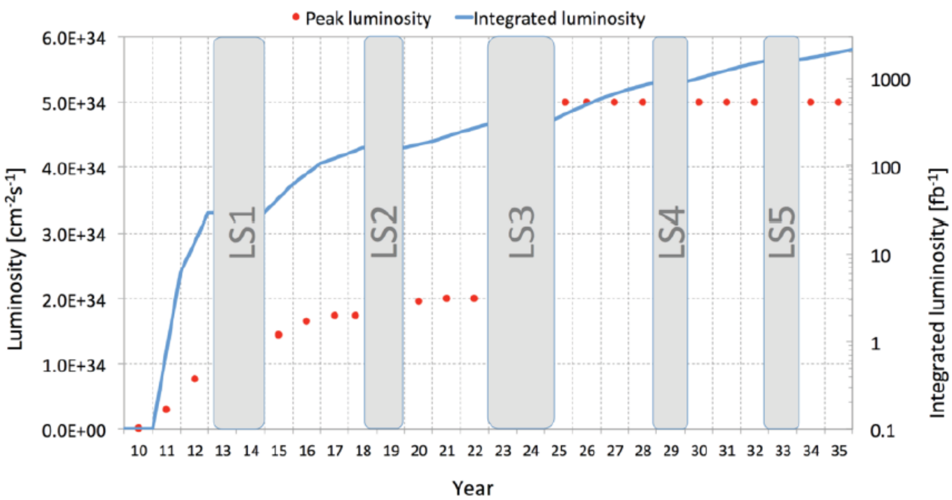

Figure 6.1: LHC luminosity plan, [36].

6.2 CMS trigger upgrade for Phase 2

The central mission of the CMS HL-LHC physics program will include precise measurement of the properties of the recently discovered Higgs boson and further searches for new physics beyond the Standard Model. Higher luminosity will extend the discovery mass reach, allow more sensitive searches for signatures for new physics, and enable studies of any newly found particles and their interactions.

The tricky goal of the Phase-2 upgrade [36] will be to maintain the overall physics acceptance under the challenging HL-LHC conditions. CMS must mantain its capability to efficiently trigger events originating from low mass physics processes (e.g. Higgs production at 125 GeV), and to perform precision measurements of low to medium p_T physics objects, leptons (e, μ, τ), photons, jets (including b tagging), and missing transverse energy (MET).

To achieve this, a number of major trigger upgrades are foreseen during the third Long Shutdown (LS3) [38]. The main one is the addition of a tracker trigger at L1, which is an integral part of the design of the new silicon tracker. CMS also plans an upgrade to the detector readout, L1 trigger, and HLT systems. This would allow up to 750 kHz L1 readout, compared to the current 100 kHz; up to 12.5 μs L1 latency, compared to the current 4 μs; up to 7.5 kHz permanent event storage rate, compared to the current 1 kHz.

These upgrades are motivated by dedicated L1 menu studies. They show that, using L1-trigger algorithms designed for the Phase-1 detector, for beam conditions of 140 events of pile-up, at least 1 500 kHz of L1 acceptance rate would be required to maintain the same physics acceptance of the Phase 1. For an environment of 200 pile-up events, the same L1 menu would require almost 4 000 kHz. Such bandwidth is beyond the technical feasibility of the CMS upgrades.
However, the same studies also demonstrate that, adding tracking information to L1 trigger, substantially, reduces these rates to about 260(500) kHz for the same beam conditions of 140(200) pile-up. These estimates do not include any uncertainty, such as simulation imperfections, limitation in releasing the L1 track based triggers in hardware and other ones. If we consider that, accounting for these uncertainties, requires a margin of 50% in the total L1 acceptance rate, we expect that the inclusion of a track trigger at L1, in conjunction with a L1 bandwidth increased up to 750 kHz, will enable CMS to retain its Phase-I physics acceptance up to 200 pile-up [37].

6.3 CMS Level-1 track trigger

6.3.1 Track-trigger motivations

The tracker will provide L1 tracks, built from the outer tracker information, for each bunch crossing. These tracks, parameterized by five helix track parameters, will be used in the L1 trigger to form the trigger decision, by combining the tracks with the information delivered by the muon and calorimeter trigger system.

The inclusion of the tracker in the trigger decision should allow to;

- better identify charged leptons (e, μ, τ),
- improve the p_T determination of charged leptons,
- determine the isolation of leptons and photons with respect to the neighboring tracks,
- determine the provenance vertex of charged leptons and jets,
- determine an event primary vertex and the transverse missing energy carried by L1 tracks that come from this vertex.

With the L1 tracks, the Global Trigger will have several new handles to increase its selectivity.
It will be possible to improve the selection of isolated leptons and photons by imposing a tracker based isolation requirement, that is more robust, with respect to pile-up, than isolation criteria which rely solely on calorimeter information.
Multi-object triggers can also be made more robust, by imposing that the objects come from the same interaction, exploiting their z-vertex.
Hadronic triggers, that require that the scalar or vector sum of the transverse energies of jets be above a given threshold, will also be improved, by restricting these sums to the jets that come from a common vertex.

Chapter 7

New L1-track-trigger system based on PCA

7.0.2 Track-finding process

A tracking algorithm has the aim to reconstruct the track trajectory of a charged particle, using the hits left in each component of the tracker detector. Given the trajectories of each event, one can know the p_T of the tracks, thanks to the curvature due to the magnetic field, and the primary vertices, and the secondary vertices coordinates of the event.
The CMS challange is now to develope an online tracking algorithm with a decision time compatible with the L1 trigger latency time, of 12.5 μs, and high quality reconstruction performances. Specially in higher rate conditions and raised number of pile-up events, the tracking algorithm has the challanging task of solving the combinatorial problem to associate the N hits of an event to a set of track candidates, distinguishing whose track is each group of hits, and throwing out the fake tracks.
To be more precise, the information left in the CMS tracker goes through different steps;

- First, a preselection of hits is enstabilished according to the cluster width, that is proportional to the radial distance of the sensor from the collision point and inversely proportional to the p_T.
- Secondly, according to the correlation between preselected hits in nearby sensors, track stubs are selected, only above a given p_T threshold of 2-3 GeV, thanks to the track direction of flight measurement.

We end up with a set of stubs for each event, to be associated to tracks featuring a p_T greater then 2-3 GeV. The track-finding problem will be solved in two levels, here presented.

1. Pattern recognition; a certain number of patterns, that reproduce physically interesting events is stored in bank files. The pattern recognition is the comparison, in parallel, between the stubs of the data event and each stored pattern. Each pattern contains a set of low resolution tracks; the roads. The Associative Memory (AM) chip receives the event stubs, and looks for compatible roads. The output of this process are the addresses of all the patterns with matched roads. Then, the interesting roads are extracted by each pattern, and associated to the high resolution stubs which will be used to perform the fit.

2. Track fitting; this is the second step of the track-finding process, it takes as input the coordinates of the selected stubs, and gives as output the parameters of each track. In principle, it can be performed with various algorithms, exploiting the hardware device of the Field Programmable Gate Array (FPGA).

The Phase-2 tracker will be involved in the L1 Trigger and, taking advantage of both the Associative Memories and the FPGA device, will ensure a trigger decision in proper time and with satisfactory performances.

7.0.3 A track fitting based on PCA

The "trick" to improve the quality in the events selection, and gain a reduction factor is to anticipate at L1 the reconstruction process, that now is performed only in the High Level Trigger (HLT). At each bunch crossing, the stubs data are processed to form L1 tracks, that are the tracker primitives to combine to the other subdetectors information to perform the L1 trigger.
The track finding process has to be very fast, and can benefit from the employment both of the Associative Memories (AM), a custom chip already used in the CDF experiment, and of the programmable device FPGA. The junction of these two tecnologies provides a faster pattern recognition function, thanks to the parallelism of the AM chips, and the extraction of high quality tracks, implementing the track fitting algorithm in the FPGA device.

One of the proposed algorithms for the fitting is based on the Principal Component Analysis method, and will be presented in the following text.

The Principal Component Analysis (PCA) is probably the oldest and best known of the techniques of multivariate analysis. The central idea of the PCA is to reduce the dimensionality of a dataset, in which there is a large number of interrelated variables, while retaining as much as possible of the variation present in the dataset. This reduction is achieved by transforming the initial set of variables to a new set of variables, called principal components, which are ordered, so that the first few retain most of the variation present in all of the original variables, and are not correlated. The computation of the principal components reduces to the solution of an eigenvalue-eigenvector problem for a positive semidefinite symmetric matrix.

In the fitting case, the transformation takes as input the coordinates of the stubs, and gives as output the track fitting parameters. In the simplest and ideal scenario, a track crossing all the barrel outer layers of the tracker, one stub per layer, leaves $3 \times 6 = 18$ stub coordinates. However, a track has 5 degree of freedom, so only 5 parameters are needed to define that.
Thus, five locally linear functions should exist, that link the track parameters to the stub coordinates;

$$p_i \sim \sum_j A_{ij} x_j + q_i, \quad i = 1, ..., 5 \ j = 1, ..., 18 \tag{7.1}$$

The validity of the linearity of the functions p(x) improves, diminishing the starting variability of the coordinates, for instance, if one restricts the geometry amplitude of the tracker sector where the tracks are taken from.

The PCA method studies the coordinates and parameters correlation, in order to find the transformation constants (A_{ij} and q_i). The PCA constant calculation uses simulates samples of PGUN prompt muons, and is the most computing laborious step of the fitting procedure. A different set of constant is needed for each geometrical sector of the tracker, that can be only barrel, only endcap or hybrid.
The starting requirement is to minimize the mean difference in absolute module between the fitted and the true (with hat) track parameters;

$$min < \hat{p}_i - p_i >, \ i = 1, ..., 5. \tag{7.2}$$

This leads to the PCA constant resulting formulas;

$$A_{li} = \sum_m V^{-1}_{lm} (< x_m \hat{p}_i > - < x_m >< \hat{p}_i >), \tag{7.3}$$

$$q_i = \hat{p}_i - \sum_j A_{ij} x_j. \tag{7.4}$$

- A_{il} are the element of the rotation matrix of the PCA transformation,
- q_i are the elements of the translation vector of the PCA transformation,
- x_m are the stub coordinates,
- $\hat{p}_i$ are the true track parameters,
- V_{lm} is the coordinates covariance matrix.

Once one have stored the PCA constant in dedicated files, the PCA fitting simply takes as input the stub coordinates, and gives as output the track fitted parameters, through a simple scalar product, using the known constants, Eq. 7.1.

7.0.4 The PCA fitting simulation

Using the framework in
$http://sviret.web.cern.ch/sviret/Welcome.php?n = CMS.HLLHCTuto620$,
we are able to simulate the expected geometry for the Phase 2, to generate simulated data of PGUN muons, and to perform the pattern recognition.

In addition, we have developed a new track fitter class that, taking as input the stubs matched in the pattern recognition process, gives as outputs the L1 fitted tracks. The PCA constants to perform the fitting are stored in .txt files for each tower, "tower" is the neomeclature used by CMS to indicate a geometrical sector of the outer tracker 7.1. The developed code is in $https://github.com/lstorchi/pca\_fit$. The interested reader can set up our software environment on lxplus following the instructions in $https://github.com/lstorchi/pca\_fit/wiki$.

Preliminar tests

As a pleriminar test, to get in touch with this statistical method, we used two elements of the PCA analysis; the covariance matrix eigenvalues and the scores.
We perform the tests, first using all the tracks in the 18 barrel tower, then taking the tracks from a more restricted geometrical sector, a subtower included in the 18

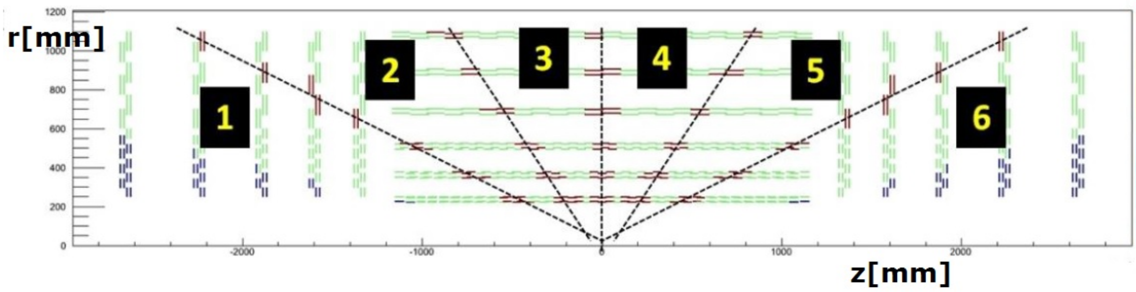

Figure 7.1: The tracker is divided into 48 trigger towers, 8 divisions in ϕ and 6 in η (here shown). This repartition ensures an optimal data sharing; a stub cannot belong to more than 4 towers.

tower see Fig. 7.2. The 18 barrel tower is defined in the range of η from -0.6 to 0.4 and ϕ from 1.1 to 2.9. The sample of muons, generated in the p_T range (2, 200) GeV, contains 10 milions of events.

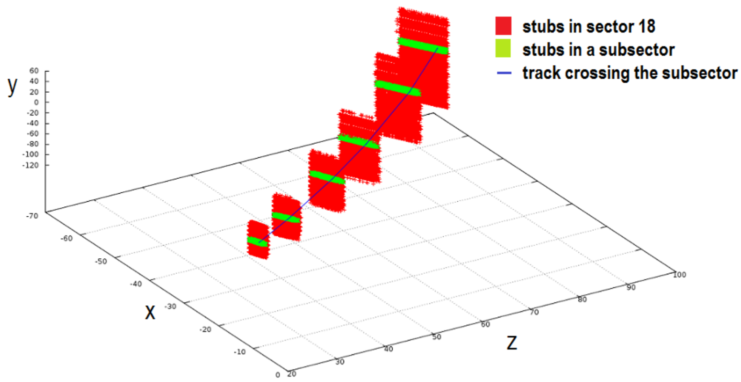

Figure 7.2: Representation of the stubs in the 18 barrel tower of the outer tower (red dots) and within one of its subtowers (green dots), in a xyz reference frame with the z axis parallel to the beam line. The blue line represents a track crossing this tower.

To perform the calculations we use the Armadillo library, that is a high quality C++ linear algebra library, aiming towards a good balance between speed and ease of use, has API syntax similar to Matlab (Octave), and can work with external libraries such as LAPACK, BLAS and ATLAS.
As input we use the 18 stub coordinates and the 5 track true parameters per track extracted from the muon training sample.

The elements of the 18×18 covariance matrix of the stub coordinates are

$V_{ij} =< x_i x_j > - < x_i >< x_j >$. In principle, we expect as eigenvalues of the covariance matrix; 5 greater eigenvalues corrispondent to the 5 degrees of freedom of the tracks and 13 negligible eigenvalues. These 13 eigenvalues contribute to the calculation of χ^2, a quality parameter that can discriminate between tracks and random combinations of stubs.

The score matrix T is the projection of the initial coordinates x_i in the new Principal Component frame of reference, it is defined as:

$$T = XL$$

where X is the x_i coordinate matrix and L is the eigenvector matrix, each column of which is an eigenvector of the covariance matrix. The score plots are the representation of this projections in the Principal Component frame (e.g. on the first 3 PC axes, because we can depict up to three dimensions), and show the behaviour of the object analised (the tracks). It is possible to point out; groups of similar objects (clusters), particular objects (outliers), and new variables correlation. The expectation is that the more the PCA method works, the more compact the resulting cluster are, and the lower is the number of outliers.

The results of this preliminar and qualitative test show that the first 5 eigenvector, expeted to be the Principal Component, assume greater values for a subtower, compared to a tower, and the variance they cover increases from 98.89% to 99.61%, restricting the geometry. The 18 eigenvalues for the two cases are reported in Table 7.1.

In addition, the scores plot, in Fig. 7.3, gives encouraging results as well; If we take all the tracks within the tower 18 we see a main cluster and some outliers. Restricting to the tracks of a subtower the outlier fraction is reduced and 7 clusters can be clearly observed, which reveal the geometrical substructure of the subtower itself.

Tower eigenvalues	Subtower eigenvalues
56.686	1565.29
16.272	57.878
7.091	21.495
1.836	7.026
1.149	1.814
0.528	1.393
0.206	1.233
0.094	1.069
0.041	0.959
0.028	0.629
0.021	0.542
0.005	0.375
0.003	0.091
0.002	0.045
0.002	0.026
0	0.021
0	0.014
0	0.003

Table 7.1: Coordinate coovariance matrix eigenvalues for the 18 tower and for a subtower within the 18 tower. The first 5 lines correspond to the 5 degrees of freedom of a track.

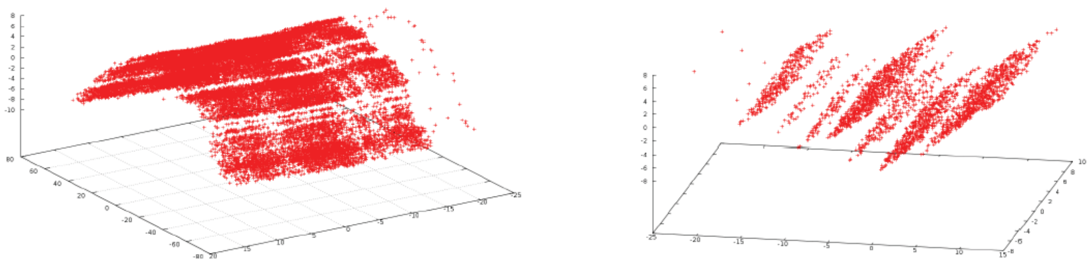

Figure 7.3: Score plot for the 18 tower (left) and for a subtower within the 18 tower (right).

The first results

Now we are more confident about the statistical operation of the PCA method, and decide to perform the fitting procedure using the muon simulated samples within the same 18 tower. The aim is to compare the resulting fitting parameters of the tracks with the true parameters.
For the choice of the fitting parameters are important; the linearity, between the variables measured by the tracker and the fitting parameters, and the flatness of the fitting parameter distributions in the training muon sample. Taking this in mind, we chooce as 5 independent parameters of the track; the longitudinal impact parameter z_0, the transverse impact parameter d_0, the pseudorapidity η, the azimuthal angle ϕ and the curvature c/p_T.
First, the fitting problem has been divided in two sub-problems;

- in plane $r - z$, from the coordinates (r_i, z_i), where i is referred to the stub, we find the two parameters of the track; z_0 and η. There are $2 \times 6 = 12$ stub coordinates for each track.

- In plane $r - \phi$, from the coordinates (r_i, ϕ_i), where i is referred to the stub, we find the two parameters of the track; c/p_T and ϕ, where c is the charge. Here it is possible to use only the three more internal layers to perform the fitting, so we have as input $2 \times 3 = 6$ stub coordinates for each track.

One can notice that the parameter d_0 is non extracted via this fitting procedure, but it is left to a second step. This is possible if one assumes that the beam spot of the collisions is perfectly centered, this means that you do not have any systematical diplacement of the beam spot and neither of the prompt tracks in the transverse plane. In other words, we have one parameter already set, because is $d_0 = 0$ in any event featuring a not displaced beam spot. Thus, we start here showing the plots referred to a 4-parameter fit.

We plot for each of the four parameter the resolution, defined as the module of the difference between the fitted and the true (hat notation) track parameter;

$$\Delta p = |p_{fit} - \hat{p}|,$$

and we consider the RMS (Root Mean Square) parameter as a first estimate of the resolution value. The results are shown in Fig.7.4 and Fig.7.5 for three different intervals for η in the $r - z$ plane and for p_T in the $r - \phi$ plane. It is possible to observe that, resctricting the intervals, the fitting resolution tends to improve, as expected. Anyway, increasing the number of subintervals, means to increase the number of set of constant to be stored, so implementing the resources of memory in the FPGA.

An optimization procedure has to be followed, in order to obtain a compromise between the resolution quality and the number of set of PCA constants to be stored.

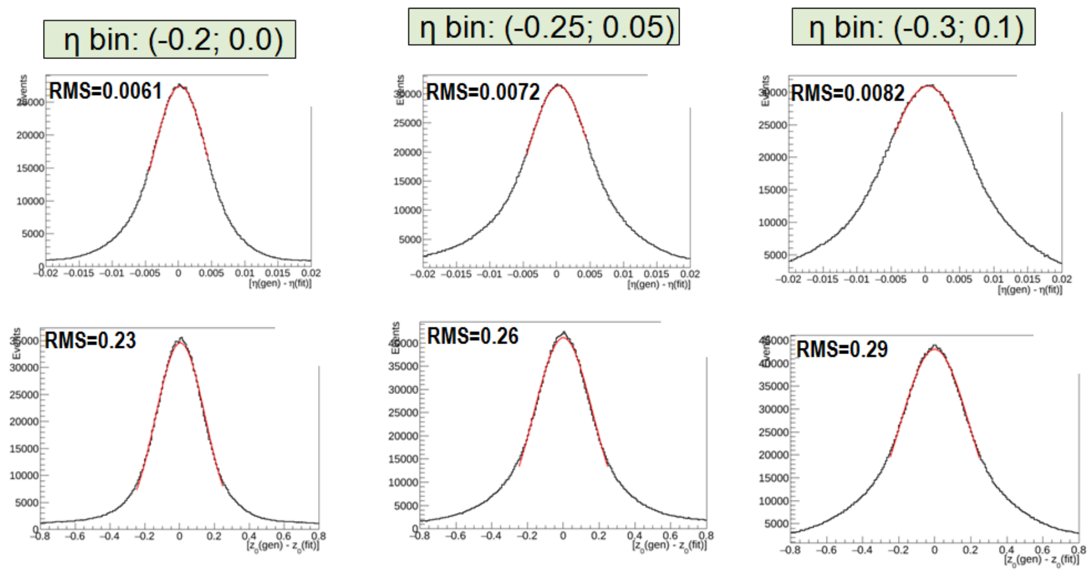

Figure 7.4: Resolution distributions for the two parameters extracted in the $r-z$ plane; η (above) and z_0 (below). Three different intervals in η have been considered.

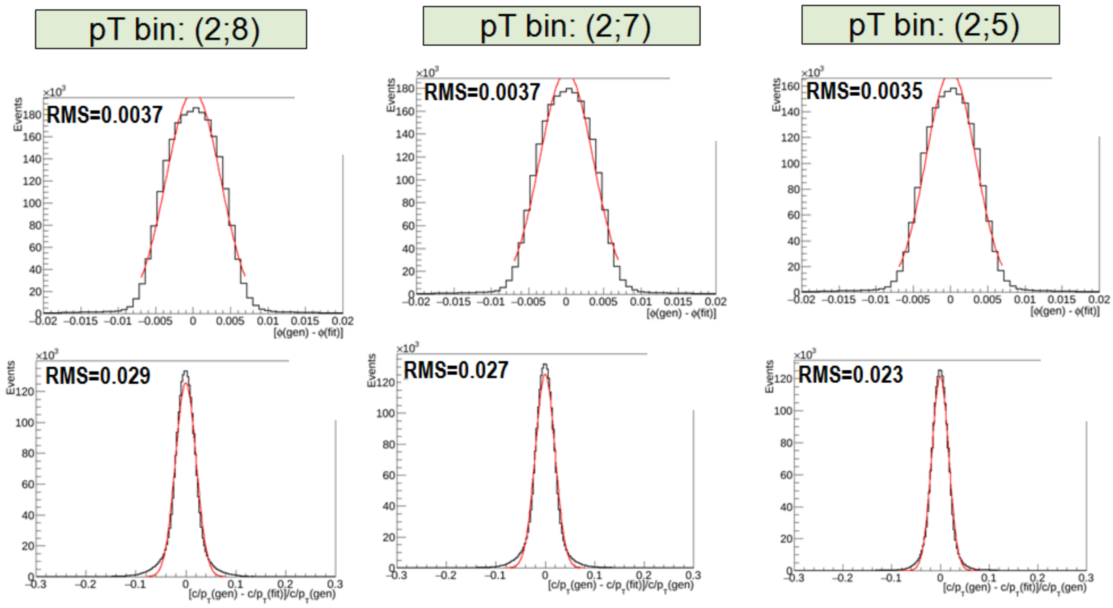

Figure 7.5: Resolution distributions for the two parameters extracted in the $r-\phi$ plane; ϕ (above) and c/p_T (below). Three different intervals in p_T have been considered.

We repeated the fitting procedure chosing different binnings in η for the $r-z$ plane and different binnings in p_T for the $r-\phi$, and for all the barrel towers. Here we present the final configuration, that ensures a good resolution and a feasible implementation in the FPGA.

- In $r-z$ plane we have 20 bins in η, so 20 sets of constants per barrel tower;
- In $r-\phi$ plane we have 7 bins in p_T and separate positive and negative muons, this gives $7 \times 2 = 14$ sets of constants per barrel tower.

The resulting values of the resolutions are reported in Table 7.2, mediated for the various barrel towers.

These results are in line with the requirements of CMS for the resolution of the L1 tracks, the study has been extended to the hybrid and endcap towers and to the case of missing stub in one layer. The whole code has been transferred in the CMSSW framework, an integer version has been coded to make the input parameter readable by the FPGA.

The final aim is the full integration of a demostrator that will evaluate these results, compare them to the simulation/emulation ones, and provide a final estimate

$\Delta\eta$	0.0024
Δz_0	0.089 cm
$\Delta\phi$	0.0002-0.0017
$\Delta c/p_T$	(0.8 - 4.1) %

Table 7.2: The values of the mean parameter resolutions, adopting a 20-binning in η and a 7-binning in p_T, respectively in $r - z$ and $r - \phi$ plane. We report only one value for η and z_0 because the resolution is stable versus η, whilst we indicate a range for ϕ and c/p_T because the resolution varies with p_T.

of the time of the L1-track reconstruction, which has to be lower then the L1 trigger latency time of the Phase 2, 12.5 μs.

7.0.5 Level-1 tracking demostrator

The goal of the CMS Level-1 tracking demonstrator is to establish the feasibility of the online tracking, within 4 μs, for particles with p_T down to 3 GeV. The different CMS Level-1 tracking approaches are studying the performances of their proposed systems in software, and implement them in small-scale prototype hardware devices. The three main approaches evaluated by CMS are;

1. AM + FPGA, based on Associative Memories (AM) for pattern recognition and FPGA for track fitting (such as the PCA aproach described so far).
2. Geometry-Based Time-Multiplexed Trigger (TMT), uses hough transform + track fit algorithm, both implemented in the FPGA.
3. Tracklet-Based, algorithmic approach, entirely based on FPGA.

The demonstration studies will utilise information obtained from several sources;

- Simulation will be used to evaluate the tracking performance (e.g. tracking efficiency, parameter resolution, track rates) and its impact on tracking-associated trigger quantities (e.g. track isolation, tracks within jets), specially in non-nominal conditions.
- Hardware emulation, means to understand how simulated tracking performances translate to hardware. Emulation software will directly correspond

to the algorithms studied in the simulation and implemented in the hardware demonstrator.

- Hardware demonstration is needed for the bitwise validation of the emulations, and for providing measurements of the overall latency associated with L1 track finding.
- Scaling/Projection will be required to extrapolate from demonstration results in terms of performance, scale and cost of the final system.

The baseline geometry to be used for the demonstrators is the standard TP2014 [39] available in $CMSSW\_SLHC\_6\_2\_X\_SLHC$. Hardware demonstrators and emulators should proceed with this standard geometry.

The simulated tracking performances will be shown using the entire tracker detector. To reduce reconfiguration and operational overhead, the hardware demonstrators may instead target a subset of tracker modules.
The hardware systems have to demonstrate the L1 track finding in a representative η slice of the detector, then the results should be easily scaled to a full system. This region should be commonly defined, so that per-track comparisons between the different approaches can be performed at the hardware level. For these reasons, each of the Level-1 tracker hardware demonstrators will explore a ϕ range between 1.346 and 1.122, spanning positive η values.

The demonstrators will evaluate the tracking performances using the data samples listed in Table 7.3. These datasets, which range from simple single particle events to more complex physics topologies (e.g. $t\bar{t}$ + PU), will provide an understanding of the intrinsic performance of L1 tracking, and of its dependence on pile-up and physics conditions. Average pile-up conditions of 0, 140 and 200 will be explored. Semileptonic top decays will be used to investigate the tracking performance for high-p_T leptons in a busy physics enviroment. Hadronic W decays and b-jets in the top sample will also be used to explore the performance of tracking within jets.

Single μ samples:
/RelValSingleMuPt1*/CMSSW_6_2_0_SLHC17-DES23_62_V1_UPG2023Muon-v1/GEN-SIM-DIGI-RAW
/RelValSingleMuPt10*/CMSSW_6_2_0_SLHC17-DES23_62_V1_UPG2023Muon-v1/GEN-SIM-DIGI-RAW
/RelValSingleMuPt100*/CMSSW_6_2_0_SLHC17-DES23_62_V1_UPG2023Muon-v1/GEN-SIM-DIGI-RAW
/RelValSingleMuPt1000*/CMSSW_6_2_0_SLHC17-DES23_62_V1_UPG2023Muon-v1/GEN-SIM-DIGI-RAW
/RelValSingleMuPt1/CMSSW_6_2_0_SLHC26-DES23_62_V1_LHCCRefPU140-v1/GEN-SIM-DIGI-RAW
/RelValSingleMuPt10/CMSSW_6_2_0_SLHC26-DES23_62_V1_LHCCRefPU140-v1/GEN-SIM-DIGI-RAW
/RelValSingleMuPt100/CMSSW_6_2_0_SLHC26-DES23_62_V1_LHCCRefPU140-v1/GEN-SIM-DIGI-RAW
/RelValSingleMuPt1/CMSSW_6_2_0_SLHC26-PU_DES23_62_V1_LHCCRefPU200-v1/GEN-SIM-DIGI-RAW
/RelValSingleMuPt10/CMSSW_6_2_0_SLHC26-PU_DES23_62_V1_LHCCRefPU200-v1/GEN-SIM-DIGI-RAW
/RelValSingleMuPt100/CMSSW_6_2_0_SLHC26-PU_DES23_62_V1_LHCCRefPU200-v1/GEN-SIM-DIGI-RAW
Single e samples:
/RelValSingleElectronPt10*/CMSSW_6_2_0_SLHC17-DES23_62_V1_UPG2023Muon-v1/GEN-SIM-DIGI-RAW
/RelValSingleElectronPt35*/CMSSW_6_2_0_SLHC17-DES23_62_V1_UPG2023Muon-v1/GEN-SIM-DIGI-RAW
/RelValSingleElectronPt1000*/CMSSW_6_2_0_SLHC17-DES23_62_V1_UPG2023Muon-v1/GEN-SIM-DIGI-RAW
/RelValSingleElectronPt10/CMSSW_6_2_0_SLHC26-DES23_62_V1_LHCCRefPU140-v1/GEN-SIM-DIGI-RAW
/RelValSingleElectronPt35/CMSSW_6_2_0_SLHC26-DES23_62_V1_LHCCRefPU140-v1/GEN-SIM-DIGI-RAW
/RelValSingleElectronPt10/CMSSW_6_2_0_SLHC26-DES23_62_V1_LHCCRefPU200-v1/GEN-SIM-DIGI-RAW
/RelValSingleElectronPt35/CMSSW_6_2_0_SLHC26-DES23_62_V1_LHCCRefPU200-v1/GEN-SIM-DIGI-RAW
Single π:
/RelValSinglePiE50HCAL/CMSSW_6_2_0_SLHC17-DES23_62_V1_UPG2023Muon-v1/GEN-SIM-DIGI-RAW
Single $t\bar{t}$:
/RelValTTbar$_1$4TeV/CMSSW_6_2_0_SLHC26-DES23_62_V1_LHCCRefPU140-v1/GEN-SIM-DIGI-RAW
/RelValTTbar$_1$4TeV/CMSSW_6_2_0_SLHC26-PU_DES23_62_V1_LHCCRefPU200-v1/GEN-SIM-DIGI-RAW

Table 7.3: Single μ, Single e, Single π and $t\bar{t}$ samples used for the simulations. The strings $PU140$ and $PU200$ indicate the number of pile-up events, whilst the samples not containing this string do not simulate the pile-up.

The L1-tracking groups will analyze their results using the tools developed by for the Technical Proposal [36] and Scope Document [37]. These tools expect input files with trees containing TrackingParticles, which represent Monte Carlo truth, and TTTracks, that are the tracks after fitting. To use these tools, the simulation frameworks of the different L1-tracking approaches must produce compatible output trees. The trees used by the groups to produce simulation results will be made publicly available, so that the groups can easy compare relative performance.

The track objects used for L1-tracking performance measurements are;

- Truth, TrackingParticles in the low and high-p_T regimes, with $|\eta^{TP}| \leq 2.4$, with $|z_0^{TP}| \leq 30$ cm, with $p_T > 3$ GeV, with $d_{xy} < 1$ cm.

- GoodTracks, TTTracks corresponding to fit tracks from simulation, with $|\eta^{fit}| \leq 2.4$ with $|z_0^{fit}| \leq 30$ cm that satisfy all other L1-tracking selections/constraints (e.g. χ^2).

- MatchedTracks, GoodTracks output from simulation, matched to Truth using the trackToTrackingParticleMap.

The L1-tracking teams should characterize tracking performance separately in low-p_T (3 - 8 GeV) and high-p_T (8 - 100 GeV) ranges. The motivation here is to delineate performance in p_T regimes in which multiple scattering is more/less relevant.

The primary quantities of interest with regard to L1-tracking performances are efficiency, parameter resolutions and the total rate of tracks output from the L1-tracking system. The definitions of these quantities are given below.

- Efficiency;
$$\epsilon = \frac{N_{matched}}{N_{truth}}.$$
- Resolution;
$$\sigma = RMS(p_{matched} - p_{truth}).$$
- Rate;
$$f = N_{fit}/BX,$$
defined as the average number of fit tracks per bunch-crossing. The rate should be examined in the low p_T range (starting from 3 GeV threshold) and at higher momentum ($p_T > 10$ GeV). The rate at low momentum drives the total rate that the L1 trigger has to deal with, and the rate at higher range gives an estimate of the purity and fake rate of the tracks.

The efficiency and resolution metrics should be assessed for single electrons, muons and pions from the particle gun samples, and for electrons and muons in the $t\bar{t}$ samples. Tracking efficiency and resolutions should also be evaluated inclusively for the $t\bar{t}$ samples. As mentioned, efficiencies and resolutions should be produced separately for the low and high p_T ranges.

Track isolation and vertex-based pile-up rejection will become important handles for the rate reduction in the HL-LHC CMS trigger. The ability to perform tracking within jets could also lead to the development of new classes of L1 triggers that use jet properties or substructure.

- To define the track isolation the variable is;
$$Iso_{trk} = \frac{\sum_i p_T(i)}{p_T(trk)},$$

where the sum extends over the i particles in a ΔR cone centered on a track (trk) of interest. Demonstrator studies will investigate the efficiency of a Iso_{trk} selection for truth-matched muon tracks with $p_T \geq 20$ GeV in the single muon 0, 140, 200 pile-up datasets. These studies will use a ΔR cone of 0.3 and include all particles with $p_T > 3$ GeV and with $|z_{muon} - z_i| < 0.5$ cm.

- Pile-up rejection;
  the performance of pile-up rejection will be assessed with a selection on the z_0 parameter of fit tracks. The TrackingParticles in the $t\bar{t} + pile - up$ samples will be associated with the primary vertex using the algorithm described in the Technical Proposal [36], which is implemented in the tools.

- Tracking within Jets;
  a basic performance evaluation of L1 tracking within jets will be performed using the hadronic decays of W bosons in $t\bar{t}$ samples. Track parameter resolutions and relative track multiplicities with respect to charged final-state TrackingParticles within the jets will be plotted against jet p_T, η, and pile-up.

In conclusion, the performance of the L1 track finding must be shown to be robust under non-nominal conditions for the Tracker TDR. The L1-tracking demonstrations should pursue additional simulation and hardware studies to help to establish this requirement. The aim of these studies will be to demonstrate performance stability with respect to; module loss, higher pile-up, and beamspot displacement.

7.0.6 A pattern recognition mezzanine for L1 track triggers

One prososed prototype for the pattern recognition and fitting of the Level-1 tracks is a Pattern Recognition Mezzanine (PRM), that combines the power of both Associative Memory custom ASIC and modern Field Programmable Gate Array (FPGA) devices [40].

To deal with the HL-LHC rate, the key is the usage of the precise tracker information for the reconstruction of the largest number of particle tracks in each individual event, in the required latency of few microseconds. A dedicated hardware processor is hence needed to select interesting signatures at the 40 MHz, and currently such class of processors is provided by the Associative Memory (AM) technology, already adopted in the CDF experiment, and recently in the ATLAS Level-2 trigger, the

Fast Tracker processor, at the High Level Trigger stage, where a longer latency is allowed. CMS is pursuing a vigorous *R&D* to demonstrate the feasibility of such an approach with the state of the art of the AM technology.

The block diagram of the tracker algorithm implemented in the Pattern Recognition Mezzanine (PRM) board consists of two sequential steps (Fig.7.6);

1. In the first step, the pattern recognition algorithm is carried out, by using the AM chip, which finds track candidates in a coarse resolution, called roads.

2. In the second step, the FPGA device performs the fitting algorithm, in which the full resolution stubs are used to fit the matched roads and to determine the track helix parameters and the goodness of the fit.

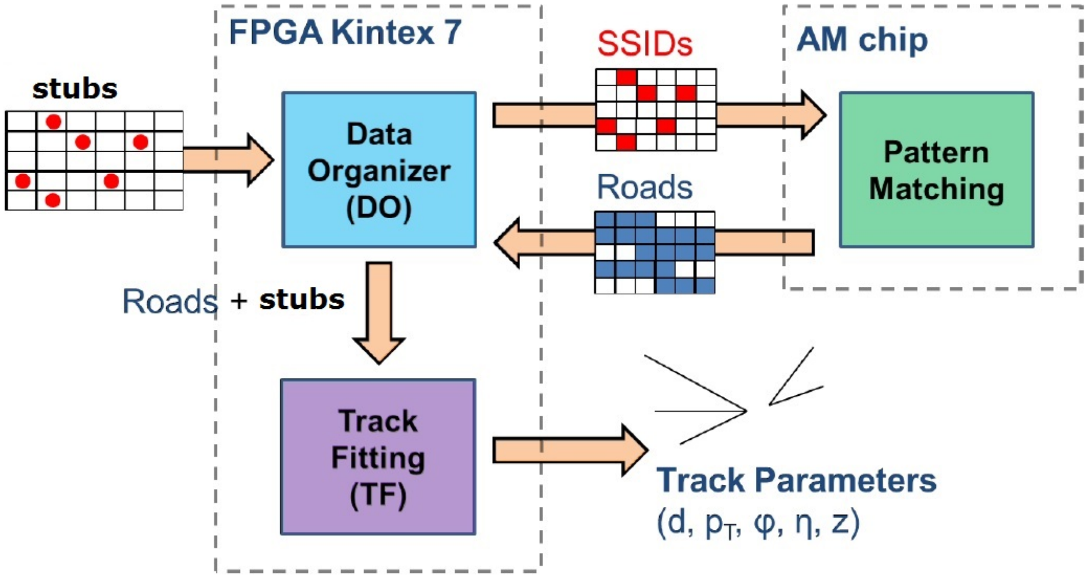

Figure 7.6: A schematic view of the Pattern Recognition Mezzanina workflow.

The full resolution stubs are received from the tracker by a Data Organizer (DO) module, that consists in a Smart Data Base where the stubs are stored in a format that allows rapid access. In addition to storing stubs at full resolution, the DO also converts them to coarser resolution hits, the Super Strip IDentification (SSID), appropriate for pattern recognition in the AM.

The generated SSIDs are sent at the same clock cycle to all the AM devices, that work similarly to a Content-Addressable Memory (CAM). Each pattern is stored in

8 independent 16-bit words, in which the coordinates, where the particle hits the silicon detector, are stored. Data are sent on 8 parallel buses, one for each word of the pattern. The feature of this device consists that all words in the AM are independent and simultaneous compared with the data presented on its own bus. Every time a match is found, the match flip-flop is set and remains set until the end of the event processing, when a reset signal is propagated.

The results of the pattern matching stage are collected inside the FPGA, and all the possible combinations are produced to form track candidates, by using the stub information stored in the DO. The so-called Track Fitting (TF) algorithm can provide high-resolution track parameters, using the values for the center of the road, and applying corrections that are linear in the actual stub position in each layer.

For each combination a fast linear fit is performed computing the χ^2 value and the track parameters. Those tracks with a χ^2 value below a predetermined threshold are considered to be good quality fits. The fit is using the same method as in FTK , based on the Principal Component Analysis (PCA), implemented by using the Digital Signal Processing (DSP) logic block inside the FPGA.
The FPGA implements, in addition, the auxiliary functions to control the AM devices (configuring and programming the bank) and also several tools for monitoring and debugging the internal data flow.

Conclusioni

The original anspect of this thesis are; a search for heavy Majorana neutrinos based on a composite model that includes the contact interaction, and a feasibility study for a new Level-1 track trigger expected to be ready for the Phase 2 of the LHC, for the CMS detector.

The new analysis has been carried on the 2015 data collected by the CMS detector. The observed data are in good agreement with the standard model prediction. An upper limit at 95% CL on the product of the cross section of the heavy composite Majorana neutrino is calculated as a function of its mass. The presence of the heavy composite Majorana neutrinos is excluded for masses up to 4.35 TeV and 4.50 TeV for a value of Λ of 5 TeV, having analysed the $eeqq$ channel and the $\mu\mu qq$ channel, respectively.

The ongoing efforts to build a solution for the High Luminosity perspective of LHC in its phase 2 have been discussed, focusing on the L1 track trigger. The results of the simulations of a new track trigger using the PCA method is giving encouraging results.The proposed processor for the hardware implementation will provide high computation power combining the Associative Memory and the FPGA technologies. The integration of firmware and hardware is going to bring to a L1-tracker demostrator planned to be ready for the end of the year, that has the aim to establish the feasibility of this track trigger project.

Appendice

Mette qui l'appendice

Bibliography

[1] http://ab-div.web.cern.ch/ab-div/Publications/LHC-DesignReport.html

[2] CMS Collaboration (2008), "The CMS experiment at the CERN LHC", JINST.

[3] CMS collaboration (1998), "CMS, tracker technical design report", CERN-LHCC-98-006.

[4] CMS collaboration (1997),"The CMS electromagnetic calorimeter project : Technical Design Report" , CERN-LHCC-97-033.

[5] CMS collaboration (1997), "CMS, The Muon Project, Technical Design Report", CERN/LHCC 97-32.

[6] CMS collaboration (2000), "CMS, The TriDAS Project, Technical Design Report, Volume 1: The Trigger Systems", CERN/LHCC 2000 - 38.

[7] CMS Collaboration (2014) "Search for heavy neutrinos and W bosons with right-handed couplings in proton-proton collisions at $\sqrt{s} = 8$ TeV", CMS-EXO-13-008.

[8] CMS Collaboration (2015) "Search for heavy Majorana neutrinos in $\mu^{\pm}\mu^{\pm}+$ jets events in proton-proton collisions at $\sqrt{s} = 8$ TeV", CMS-EXO-12-057.

[9] CMS Collaboration (2016) "Search for heavy Majorana neutrinos $e^{\pm}e^{\pm}+$ jets and $e^{\pm}\mu^{\pm}+$ jets events in proton-proton collisions at $\sqrt{s} = 8$ TeV", CMS-EXO-14-014.

[10] CMS Collaboration (2016) "Search for heavy neutrinos and third-generation leptoquarks in final states with two hadronically decaying τ leptons and two jets in proton-proton collisions at $\sqrt{s} = 13$ TeV", CMS PAS EXO-16-016.

[11] CMS Collaboration (2016) "Search for pair production of first and second generation leptoquarks in proton-proton collisions at $\sqrt{s} = 8$ TeV", CMS-EXO-12-041.

[12] CMS Collaboration (2014) "Search for pair production of third-generation scalar leptoquarks and top squarks in proton-proton collisions at $\sqrt{s} = 8$ TeV", CMS-EXO-12-032.

[13] CMS Collaboration (2016) "Search for pair-production of second-generation scalar leptoquarks in pp collisions at $\sqrt{s} = 13$ TeV with the CMS detector", CMS PAS EXO-16-007.

[14] R. Leonardi, L. Alunni, F. Romeo, L. Fanò and O. Panella (2016), "Hunting for heavy composite Majorana neutrinos at the LHC", arXiv:1510.07988.

[15] CMS Collaboration (2010) "CMS Tracking Performance Results from Early LHC Operation", CMS-TRK-10-001.

[16] CMS Collaboration (2014) "Description and performance of track and primary-vertex reconstruction with the CMS tracker", CMS-TRK-11-001.

[17] CMS Collaboration (2014) "Alignment of the CMS tracker with LHC and cosmic ray data", CMS-TRK-11-002.

[18] A. Tricomi (2014) "Upgrade of the CMS tracker", IOPScience.

[19] P. De Jong (2012) "Supersymmetry searches at the LHC", Proceedings of the PIC 2012.

[20] A. Hinzmann (2015) "Searches for exotic new physics in CMS", EDP Sciences.

[21] Muon POG, Muon identification and isolation (2015),
https://twiki.cern.ch/twiki/bin/viewauth/CMS/SWGuideMuonIdRun2.

[22] HEEP group, HEEP V6.0 selection for Run II analyses" (2015),
https://twiki.cern.ch/twiki/bin/viewauth/CMS/HEEPElectronIdentificationRun2.

[23] Electron POG, Cut based electron identification" (2015),
https://twiki.cern.ch/twiki/bin/view/CMS/CutBasedElectronIdentificationRun2.

[24] Jet POG, Jet identification for Run II (2015),
https : //twiki.cern.ch/twiki/bin/view/CMS/JetID.

[25] CMS Collaboration, "HEEP6.0 Selection efficiency Scale Factor Study for CMS in Run 2",
CMS AN 2015/320, 2015.

[26] Muon POG, "Muon identification and isolation data/MC scale factors (2015)",
https : //twiki.cern.ch/twiki/bin/viewauth/CMS/MuonReferenceEffsRun2#Results_f

[27] Jet POG, "Recommended Jet Energy Corrections and Uncertainties For Data and MC" (2015),
https : //twiki.cern.ch/twiki/bin/view/CMS/JECDataMC.

[28] BTV POG, Supported Algorithms and Operating Points (2015),
https : //twiki.cern.ch/twiki/bin/viewauth/CMS/BtagRecommendation76X.

[29] CMS Collaboration, Search for a Narrow Resonance Produced in 13 TeV pp Collisions Decaying to Electron Pair or Muon Pair Final States,CMS-PAS-EXO-15-005, 2015.

[30] Luminosity, Documentation of the RooStats-based statistics tools for Higgs PAG",
https : //twiki.cern.ch/twiki/bin/viewauth/CMS/SWGuideHiggsAnalysisCombinedLim

[31] CMS Collaboration, "Search for massive resonances decaying into pairs of boosted W and Z bosons at 13 TeV" (2015), CMS-PAS-EXO-15-002.

[32] Muon group, "Reference guidelines and results for muon momentum scale and resolution in Run-II" (2015),
https : //twiki.cern.ch/twiki/bin/view/CMS/MuonReferenceScaleResolRun2.

[33] Jet POG, "Recommended Jet Energy Corrections and Uncertainties For Data and MC" (2015),
https : //twiki.cern.ch/twiki/bin/view/CMS/JECDataMC.

[34] Jet POG, "Jet Energy Resolution" (2015),
https : //twiki.cern.ch/twiki/bin/view/CMS/JetResolution.

[35] J. Butterworth et al., "PDF4LHC recommendations for LHC Run II", $arXiv$: 1510.03865.

[36] CMS Collaboration, "Technical proposal for Phase-II Upgrade of the Compact Muon Solenoid " (2015), CERN-LHCC-2015-10.

[37] CMS Collaboration, "CMS Phase II Upgrade Scope Document" (2015), CERN-LHCC-2015-19.

[38] CMS collaboration, "CMS Technical Design Report for the Level-1 Trigger Upgrade"(2013), CERN-LHCC-2013-011.

[39] Technical Proposal geometry for Phase 2, $http$: $//mersi.web.cern.ch/mersi/layouts/.current/TechnicalProposal2014/index.html$.

[40] D. Magalotti, L. Alunni, N. Biesuz, G.M. Bilei, S. Citraro, F. Crescioli, L. Fanò, G. Fedi, G. Magazzù, L. Servoli, L. Storchi, F. Palla, P. Placidi, E. Rossi and A. Spiezia,"A Pattern Recognition Mezzanine based on Associative Memory and FPGA technology for Level 1 Track Triggers for the HL-LHC upgrade", (2016) ScienceDirect.